Multi-generation chemical aging of secondary organic aerosol components under initial high/low NO_x conditions

Submitted in partial fulfillment of the requirements for

the degree of

Doctor of Philosophy

in

Chemical Engineering

Ningxin Wang

B.S., Chemical Engineering, University of Arizona
B.S., Environmental Science and Engineering, Shanghai Jiao Tong University

Carnegie Mellon University

Pittsburgh, PA

January 2018

(Note: This is an unnumbered page)

To

Mei and Tianbao

Acknowledgements

This work would not have been possible without the tremendous amount of help and support from my advisors over the past five years. It is a privilege for me to have worked with two of the most exceptional scientists, Prof. Spyros Pandis and Prof. Neil Donahue. Under their guidance, I have learnt both the integrity and the creativity aspects of science and the approach to it, and gradually transitioned from a college graduate with minimum research experience to an independent researcher. I am sincerely grateful to Prof. Pandis for his guidance both in research and in life, for his invaluable inputs and feedback to this work, and for the opportunities to present at scientific conferences as well as participate in international field campaigns. Our discussion about career path during the Orlando conference, and the lunch discussion about life choices in Patras during the Greece campaign have left deep impression on me. I am sincerely grateful to Prof. Donahue for the countless research discussions, for his encouragement for ideas, and for his invaluable inputs and feedback to this work. Aside from research, his active involvement in public speech as an ambassador of our field to the general public constantly inspires me. I am so incredibly lucky to have these two role models as my mentors.

I would also like to thank the rest of my committee members, Prof. Allen Robinson, Prof. Peter Adams and Prof. Robert Tilton for taking the time to read my proposal and thesis, sharing their expertise, and providing invaluable advices and suggestions for the improvement of this work. Although not on the committee, Prof. Albert Presto has helped me no less by spending time discussing with me the experimental details and sharing the data from his own PhD work from ten years ago.

My peers at CAPS over the past five years have not only shared their research experience,

but offered me their sincere friendship. I would like to acknowledge Antonios Tasoglou for teaching me all the details in lab, for his friendship and for his family to have accommodated me during my stay in Athens. He is not only my lab mate in crime, but a dear friend. I would like to thank Yunliang Zhao, Penglin Ye and Adam Ahern for sharing their research expertise on various aspects. I would also like to thank my friends Xiang Li and Qing Ye for their company during working late hours, Elina Karnezi for delicious homemade cuisines, Nicholas Skarzynski for the afternoon jogs, Victoria Haufboue for the horseback riding lessons and Aja Ellis for the climbing adventures. The length of this acknowledgement does not allow a full list of the many, many more happy moments that I share with them. I would like to acknowledge all the CAPSians that I have encountered and known over the past five years. I am beyond grateful to have been colleagues and friends with such a vibrant group of individuals. Colleagues from the LAQS group at the University of Patras also provided excellent technical help. Evangelia Kostenidou shared her knowledge in AMS, Christos Kaltsonoudis his knowledge in PTRMS and experience during the field campaign.

I would not have achieved any of this had it not been my parents, who are always there for me. My mother, Mei, who has a college math degree and an advanced degree in Economics, is the most loving person I know. Her encouragement and positive attitude towards life influence me significantly, and from time to time remind me that life is larger than the current obstacle. My father, Tianbao, who has a college engineering degree and an advanced degree in engineering thermodynamics, has always inspired me with his unaging desire to learn. I dedicate this work to them for their endless support and unconditional love.

Finally, I would like to thank the US Environmental Protection Agency for the funding of this research.

Abstract

Secondary organic aerosol (SOA) formation from volatile organic compounds (VOCs) in the atmosphere can be thought of as a succession of oxidation steps. The production of later-generation SOA via continued oxidation of the first-generation products is defined as chemical aging. Zeroth order parameterizations have been developed to model the chemical aging of semi-volatile and intermediate volatility organic compounds in chemical transport models. Models using these schemes show improved performance in urban areas. However, they tend to over-predict OA in areas such as the southeastern United States where biogenic VOCs dominate if chemical aging is assumed to be a major source of additional SOA. As a result, the importance of aging of biogenic SOA as a source of SOA mass concentration remains an issue of debate.

In the first part of this work, we investigated aging in the α-pinene ozonolysis system with hydroxyl radicals (OH) through smog chamber experiments. The first-generation α-pinene ozonolysis products were allowed to react further with OH formed via HONO photolysis. After an equivalent of 2-4 days' of atmospheric oxidation, homogeneous OH oxidation of the α-pinene ozonolysis products resulted in a 20-40 % net increase of the SOA for the experimental conditions used in this work. A more oxygenated product distribution was observed after aging based on the increase in aerosol atomic oxygen to carbon ratio (O:C) by up to 0.04. Experiments performed at intermediate relative humidity (RH) of 50 % showed no significant difference in additional SOA formation during aging compared to those performed at low RH of less than 20 %.

The interaction of particles with the chamber walls has been a significant source of uncertainty when analyzing results of experiments performed in Teflon chambers. For complex experiments such as chemical aging of secondary organic aerosol, the results of the SOA quantification analysis can be quite sensitive to the adopted correction method due to the evolution

of the particle size distribution and the duration of these experiments. In the second part of this work, we evaluated the performance of several particle wall-loss correction methods for aging experiments of α-pinene ozonolysis products. Determining the loss rates from seed loss periods is necessary for this system because it is not clear when chemistry is over. Results from the organic to sulfate ratio and the size-independent correction methods can be influenced significantly by the size-dependence of the particle wall-loss process. Coagulation can also affect the particle size distribution, especially for particles with diameter less than 100 nm, thus introducing errors in the results of the wall-loss correction. The corresponding loss rate constants may vary from experiment to experiment, and even during a specific experiment. Friction between the Teflon chamber walls and non-conductive surfaces can significantly increase particle wall-loss rates and the chamber may require weeks to recover to its original condition. Experimental procedures are proposed for the characterization of particle losses during different stages of these experiments and the evaluation of corresponding particle wall-loss correction.

NO_x ($NO+NO_2$) can affect secondary organic aerosol formation by introducing a critical branching point in the fate of organo-peroxy radicals (RO_2) produced from the oxidation of organic compounds. The formation of organonitrates ($R\text{-}ONO_2$) from this pathway can potentially shift the product distribution and thus affect SOA yields and composition. In the third part of this work, we investigated the oxidation of the first-generation products of α-pinene ozonolysis from the RO_2+NO pathway with additional OH radicals by performing aging experiments of α-pinene ozonolysis products formed under high NO_x conditions in a smog chamber. The fate of RO_2 radicals during these experiments was determined using a kinetics box model. The α-pinene in our experiments reacted with O_3, NO_3 and OH. The reduction in the first-generation yields under the high NO_x levels used in this study was mainly attributed to α-pinene reacting with NO_3. Our zeroth

order estimate suggests that the ozonolysis RO_2+NO pathway yielded similar amount of SOA compared to the RO_2+RO_2 alternative. After an equivalent of 1-2 days' of typical atmospheric exposure to OH, the chemical aging processes of the α-pinene ozonolysis products formed under high NO_x resulted in a net increase of up to 25 % in the SOA for the experimental conditions used in this work. A more oxygenated product distribution was observed after aging based on the increase in aerosol atomic oxygen to carbon ratio (O:C) by up to 0.06. Organonitrates accounted for around one quarter of the first-generation SOA. Their fractional contribution to SOA increased to around 40 % after aging.

Table of Contents

List of tables

List of figures

Chapter 1

Introduction

1.1 Atmospheric aerosols

Atmospheric aerosols are airborne solid or liquid particles that range in size from approximately 1 nm to 100 µm. The air quality indicator $PM_{2.5}$ refers to the aerosol mass concentration of particles with diameter less than 2.5 µm, while PM_{10} to those smaller than 10 µm. Anthropogenic activities such as fuel combustion as well as biogenic sources such as emissions from vegetation can introduce particles and particle precursors into the atmosphere. The main chemical components of atmospheric aerosols include organic compounds, sulfate, nitrate, ammonium, sodium, chloride, water as well as metal oxides, dust and black carbon.

Atmospheric aerosols pose a significant risk to human health by causing respiratory problems and heart attacks (Davidson et al., 2005; Pope et al., 2009). A recent cohort epidemiological study involving more than 60 million people has shown a 7.3 % increase in all-cause mortality per 10 µg m^{-3} $PM_{2.5}$ (Di et al., 2017). In addition to their health impacts, atmospheric aerosols influence the climate of our planet via scattering or absorbing radiation directly, and via acting as cloud condensation nuclei indirectly (IPCC, 2011).

1.2 Secondary organic aerosols (SOA)

Roughly half of the submicron aerosol mass is composed of organic compounds in a lot of areas (Murphy et al., 2006; Zhang et al., 2007; Jimenez et al., 2009). Organic aerosols (OA) can be categorized into primary and secondary. Primary organic aerosols (POA) are traditionally defined as particles directly emitted into the atmosphere. Their sources can be both anthropogenic including vehicle exhaust, biomass burning and cooking etc. and biogenic including pollen etc. Secondary organic aerosols (SOA) are those formed through gas-phase oxidation of volatile, intermediate volatility and semi-volatile organic compounds and condensation of some of the

corresponding products (Robinson et al., 2007; Zhao et al., 2014). Traditional precursors for SOA include both anthropogenic and biogenic volatile organic compounds (VOCs). Anthropogenic SOA precursors include aromatic VOCs from fossil fuel combustion such as toluene, benzene and xylenes while biogenic VOCs include monoterpenes ($C_{10}H_{16}$), sesquiterpenes ($C_{15}H_{14}$) and isoprene (C_5H_8). Biogenic VOC emissions exceed anthropogenic ones on a global scale and play an important role in atmospheric chemistry (Kanakidou et al., 2005).

The three most abundant oxidants in the atmosphere that react with VOCs to form SOA are O_3, OH, and nitrate radicals (NO_3). OH-initiated reactions occur mainly during daytime since OH radicals are formed mostly during photolysis. NO_3-intiated reactions occur mainly at night since NO_3 radicals photo-dissociate rapidly during daytime. Reactions with O_3 (Fig. 1.1) can occur at all times.

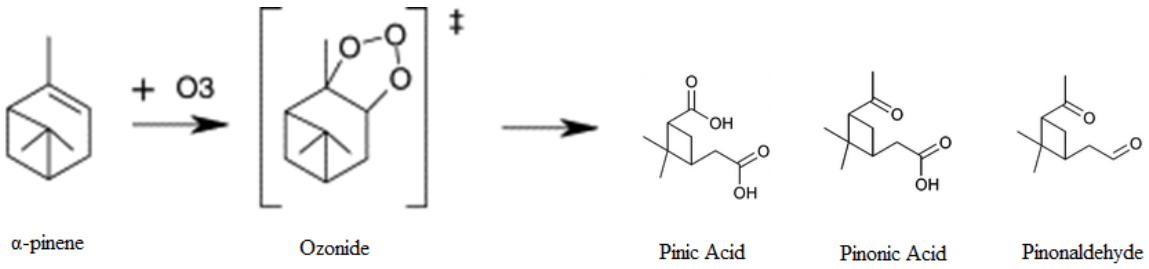

Figure 1.1: Ozone reacts with α-pinene (most abundant monoterpene) and forms an ozonide as an intermediate product. Major products of α-pinene ozonolysis include pinic acid, pinonic acid, and pinonaldehyde.

The SOA mass yield, *Y*, is a metric of the ability of a gaseous precursor to form SOA, and is defined as $Y=C_{SOA}/\Delta VOC$, where C_{SOA} is the produced SOA mass concentration and ΔVOC the amount of the VOC precursor reacted. Parameterizations of the SOA mass yields from specific precursors based on laboratory studies are incorporated into chemical transport models (CTMs) to predict ambient SOA levels.

1.3 Role of NO_x in SOA formation

The effect of NO_x on SOA formation is complex. Laboratory studies suggest that SOA mass yields from smaller (less than 10 carbon atoms) precursors are generally lower at high NO_x (Presto et al., 2005b, Kroll et al., 2006; Ng et al., 2007), but the high-NO_x yields rise compared to low-NO_x yields for larger precursors (Ng et al., 2007) and later generations (Zhang et al., 2006; Chacon-Madrid and Donahue, 2011). Furthermore, there are indications that products formed at low-NO_x may be vulnerable to photolysis (Kroll et al., 2006; Presto et al., 2005a; Henry and Donahue, 2012). Lane et al. (2008) suggested that in many urban areas as NO_x emissions are reduced, the NO_x-dependent SOA yields will either increase or remain relatively constant, but an increase in oxidant concentrations will produce an increase in SOA. In rural NO_x-limited areas, decreasing the NO_x emissions could reduce the SOA concentrations by reducing the concentration of oxidants present. In this case according at least to Lane et al. (2008), the NO_x-dependent SOA yields are not expected to significantly increase. In other areas, the SOA concentrations may remain relatively constant as the NO_x emissions are reduced because the increase in the NO_x-dependent SOA yields are offset by the decrease in oxidant concentrations. These authors estimated that the average biogenic SOA in the southeast US during the summer will decrease by roughly 0.5 $\mu g\ m^{-3}$ for a 50 % reduction in the 2001 NO_x emissions. The above conclusions of the Lane et al. (2008) study were based on a relatively simple parameterization of the SOA yield dependence on NO_x levels using a branching ratio and the few available at that time low- and high-NO_x yield measurements for monoterpenes and isoprene from laboratory studies. These simplifications together with the uncertainties about the NO_x-dependence of the aromatic VOCs and sesquiterpenes introduced significant uncertainties in their predictions. They recommended additional experiments and corresponding theoretical analyses are needed to reduce these uncertainties.

1.4 Chemical aging of SOA

Oxygenated OA with a high oxygen to carbon ratio (O:C) is often the most important component of ambient OA suggesting the importance of atmospheric chemistry in the formation and processing of OA (Zhang et al., 2007). Early studies of SOA formation focused exclusively on the first stage of reactions involving the target precursor reacting with the chosen oxidant. In the atmosphere, organic vapors and particles interact with oxidants for days and therefore successive oxidation processes are inevitable.

Chemical aging refers to the subsequent stages of SOA formation and evolution due to the production of later-generation products via oxidation of first-generation products by oxidants such as OH free radicals (Donahue et al., 2006; Henry et al., 2012). Previous studies have explored various forms of aging, including heterogeneous reactions of oxidants and aerosols (George et al., 2008), oligomerization (Kalberer et al., 2006), photolysis of either gas or condensed-phase products (Henry and Donahue, 2012), and homogeneous gas-phase oxidation by OH (Donahue et al., 2012). Homogeneous gas-phase oxidation reactions appear to be in general much faster than heterogeneous reactions, due to diffusion limitations of the latter (Lambe et al., 2009). The first-generation oxidation reactions of most SOA precursors convert much less than 50 % of the precursor to SOA, leaving more than half of the carbon still in the gas-phase. Additional oxidation of these vapors can potentially contribute additional and more oxygenated SOA components. These later-generation reactions have been proposed to be a major missing step connecting laboratory studies to field measurements.

Zeroth order parameterizations have been developed to model the chemical aging of semi-volatile and intermediate-volatility SOA components in chemical transport models (Robinson et al., 2007). CTMs using these aging schemes show improved performance in urban areas such as

Mexico City (Tsimpidi et al., 2011). On the other hand, aging schemes that assume significant later generation production of biogenic SOA tend to over-predict OA in areas such as the southeastern United States where biogenic VOCs dominate (Lane et al., 2008) (Fig. 1.2). As a result, the importance of aging of biogenic SOA as a source of SOA mass concentration remains an issue of debate.

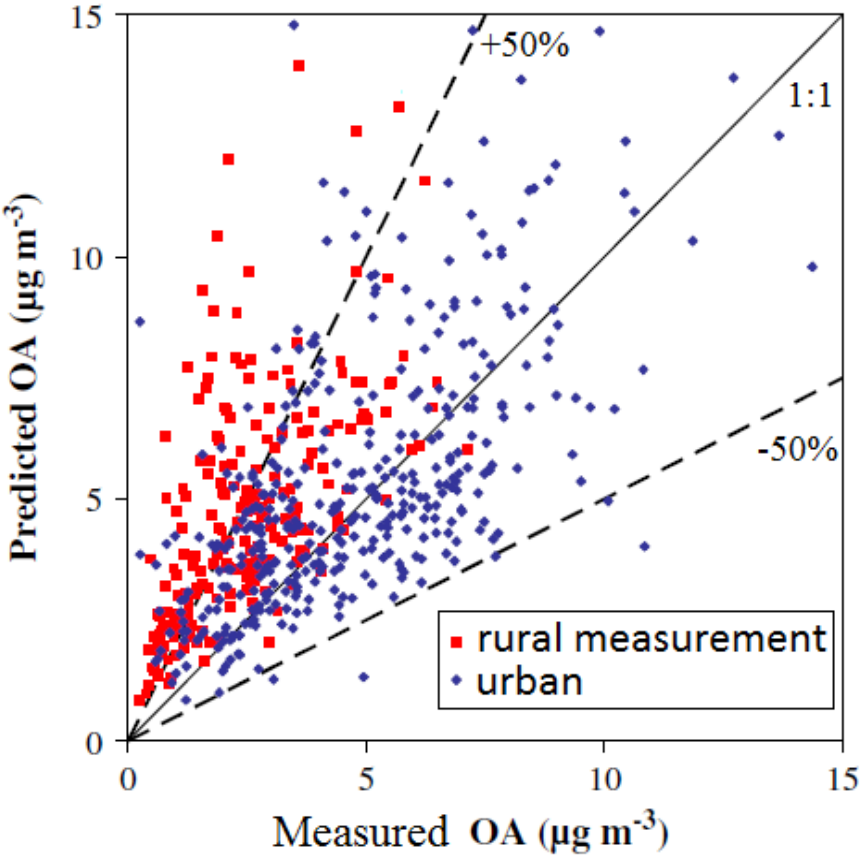

Figure 1.2: The PMCAMx model overpredicted ambient OA in rural areas mostly in the Southeast US (red symbols) assuming that aging of biogenic SOA results in significant additional SOA mass (Lane et al., 2008).

Despite the consensus from previous laboratory studies that gas-phase OH aging of the first-generation products from biogenic precursors can contribute additional SOA (Donahue et al., 2012; Qi et al., 2012), the magnitude of this effect as a function of the exposure to OH remains

uncertain. Few studies so far have explored aging of the first-generation products formed under high-NO_x initial conditions. While the first-generation monoterpene SOA mass yields are generally lower at high-NO_x due to formation of products of higher volatility, later-generation SOA formation could be enhanced with additional OH.

1.5 Environmental simulation chambers

Environmental simulation chamber (or smog chamber) experiments are an efficient approach to study atmospheric oxidation processes by isolating specific processes in a controlled environment. These reactors are typically made out of Teflon, and their volume varies from a few hundred liters up to hundreds of cubic meters. Thousands of smog chamber experiments have been conducted by different groups around the world to simulate the behavior of the pollutants in ambient air. These smog chambers have been used to study formation and yields of secondary organic aerosols and the effects of temperature, relative humidity, UV intensity, NO_x levels (Hallquist et al., 2009; Tritscher et al., 2011). Other chamber studies have focused on the characterization and evolution of primary emissions from selected sources (Weitkamp et al., 2007; Kostenidou et al., 2013; Platt et al., 2013).

One major challenge of smog chamber experiments is the interaction of vapors and particles with Teflon walls. The wall-loss rate of particles is a function of particle size, charge distribution, chamber geometry, turbulence and electric field within the chamber (Crump and Seinfeld, 1981). The particle wall-loss process is first-order and the particle wall-loss rate constant, *k*, is defined as,

$$\frac{\partial N(D_p,t)}{\partial t} = -k(D_p,t)N(D_p,t), \quad (1)$$

where $N(D_p, t)$ is the number concentration of particles with diameter D_p at time t. For an aerosol population, k is in general a function of particle size and time. Smaller-sized particles (less than 50 nm) have a higher loss rate due to diffusion-dominated wall-loss process, while particles larger than one micron are lost mainly due to sedimentation. Electrostatic effects can play a major role for intermediate sizes (McMurry and Rader, 1985).

The interaction of particles with the chamber walls has been a significant source of uncertainty when analyzing results of experiments performed in Teflon chambers. Early studies of of secondary organic aerosol (SOA) formation and growth assumed that the particle wall loss is negligible in fairly large chambers (~30 m^3) when determining SOA yields (Stern et al., 1987). A number of particle wall-loss correction methods have been proposed including the use of a size-independent loss rate constant, ratio of suspended organic to sulfate or other conserved tracer, size-dependent loss rate constant (Keywood et al., 2004; Pathak et al., 2007; Hildebrandt et al., 2009; Nah et al., 2017). For complex experiments such as chemical aging of secondary organic aerosol (SOA), the results of the SOA quantification analysis can be quite sensitive to the adopted correction method due to the evolution of the particle size distribution and the duration of these experiments. It is thus important to address both the time- and size-dependence of the particle loss rates for the purpose of SOA quantification in these experiments.

Recent findings that organic vapors in the chamber can be directly lost to the Teflon walls as well further complicate the wall-loss correction process (Matsunaga and Ziemann, 2010; Zhang et al., 2014).

1.6 Thesis overview

In this thesis, we present experimental investigations of the chemical aging of the first-

generation products of the most important monoterpene, α-pinene, with OH. We quantify the additional SOA yields, investigate the changes in the SOA chemical composition with the corresponding OH exposure and explore the effect of initial NO_x levels upon aging.

In Chapter 2, we quantify the yields of OH aging of the α-pinene ozonolysis products formed under intermediate and low relative humidity (RH), and explore the changes in the SOA oxidation level with the corresponding OH exposure. We adopt a size-dependent particle wall-loss correction method and develop a procedure to better constrain the associated errors. We also attempt to constrain the vapor loss using both theoretical calculations and measurements.

In Chapter 3, we evaluate the performance of several particle wall-loss correction methods for aging experiments. We explore the effect of coagulation on particle wall-loss rate constants through experiments with seed particles. Apart from the size-dependence of the particle wall-loss rates, we also address their time dependence. We propose an operating procedure for Teflon chambers to achieve minimal particle wall loss.

In Chapter 4, we quantify the yields of OH aging of the α-pinene ozonolysis products formed under initial high-NO_x conditions, examine the formation of organonitrate compounds, and explore the changes in the SOA oxidation level with the corresponding OH exposure. We adopt a kinetics box model to monitor the chemistry during the first-generation oxidation and to track the fate of the precursor and the formed organoperoxy radicals (RO_2). We also probe the SOA yield from the reaction of α-pinene and NO_3, and that of the RO_2+NO pathway.

Additional perturbation experiment of ambient air with a dual chamber system is described in the Appendix of the thesis.

1.7 References

Chacon-Madrid, H. J., and Donahue, N. M.: Fragmentation vs. functionalization: Chemical aging and organic aerosol formation, Atmos. Chem. Phys., 11, 13693-13721, 2011.

Crump, J. G., and Seinfeld, J. H.: Turbulent deposition and gravitational sedimentation of an aerosol in a vessel of arbitrary shape, J. Aerosol Sci., 2, 405–415, 1981.

Davidson, C. I., Phalen, R. F., and Solomon, P. A.: Airborne particulate matter and human health: a review, Aerosol Science and Technology, 39, 737–749, 2005.

Di, Q., Wang, Y., Zanobetti, A., Wang, Y., Koutrakis, P., Choirat, C., Dominici, F., and Schwartz, J. D.: Air pollution and mortality in the medicare population, N. Engl. J. Med., 376, 2513-2522, 2017.

Donahue, N. M., Robinson, A. L., Stanier, C. O., and Pandis, S. N.: Coupled partitioning, dilution, and chemical aging of semivolatile organics, Environ. Sci. Technol., 40, 2635-2643, 2006.

George, I. J., Slowik J., and Abbatt J. P. D.: Chemical aging of ambient organic aerosol from heterogeneous reaction with hydroxyl radicals, Geophys. Res. Lett., 35, L13811, 2008.

Griffin, R. J., Cocker, D. R., Seinfeld, J. H., and Dabdub, D.: Estimate of global atmospheric organic aerosol from oxidation of biogenic hydrocarbons, Geophys. Res. Lett., 26, 2721–2724, 1999.

Hallquist, M.; Wängberg, I.; Ljungstrom, E.; Barnes, I.; Becker, K: Aerosol and product yields from NO_3 radical-initiated oxidation of selected monoterpenes, Environ. Sci. Technol., 33, 553, 1999.

Henry, K. M., and Donahue, N. M.: Photochemical aging of α-pinene secondary organic aerosol: effects of OH radical sources and photolysis: J. Phys. Chem. A, 116, 5932−5940, 2012.

Henry, K. M., Lohaus T., and Donahue, N. M.: Organic aerosol yields from α-pinene oxidation: bridging the gap between first-generation yields and aging chemistry, Environ. Sci. Technol., 46, 12347−12354, 2012.

Hildebrandt, L.; Donahue, N. M.; Pandis, S. N.; High formation of secondary organic aerosol from the photo-oxidation of toluene; Atmos. Chem. Phys., 9, 2973–2986, 2009.

Intergovernmental Panel on Climate Change: Climate Change 2007: Synthesis Report. Contribution of Working Groups I, II and III to the Fourth Assessment Report of the Intergovernmental Panel on Climate Change, edited by R. K. Pachauri and A. Reisinger, eds., 104 pp., Cambridge Univ. Press, New York, 2007.

Jimenez, J. L., Canagaratna, M. R., Donahue, N. M., Prévôt, A. S. H., Zhang, Q., Kroll, J. H., DeCarlo, P. F., Allan, J. D., Coe, H., Ng, N. L., Aiken, A. C., Docherty, K. S., Ulbrich, I.

M., Grieshop, A. P., Robinson, A. L., Duplissy, J., Smith, J. D., Wilson, K. R., Lanz, V. A., Hueglin, C., Sun, Y. L., Tian, J., Laaksonen, A., Raatikainen, T., Rautiainen, J., Vaattovaara, P., Ehn, M., Kulmala, M., Tomlinson, J. M., Collins, D. R., Cubison, M. J., Dunlea, E., J., Huffman, J. A., Onasch, T. B., Alfarra, M. R., Williams, P. I., Bower, K., Kondo, Y., Schneider, J., Drewnick, F., Borrmann, S., Weimer, S., Demerjian, K., Salcedo, D., Cottrell, L., Griffin, R., Takami, A., Miyoshi, T., Hatakeyama, S., Shimono, A., Sun, J. Y, Zhang, Y. M., Dzepina, K., Kimmel, J. R., Sueper, D., Jayne, J. T., Herndon, S. C., Trimborn, A. M., Williams, L. R., Wood, E. C., Middlebrook, A. M., Kolb, C. E., Baltensperger, U., and Worsnop D. R.: Evolution of organic aerosols in the atmosphere, Science, 326, 1525-1529, 2009.

Kalberer, M., Sax, M., and Samburova, V.: Molecular size evolution of oligomers in organic aerosols collected in urban atmospheres and generated in a smog chamber, Environ. Sci. Technol., 40, 5917−5922, 2006.

Kanakidou, M., Seinfeld, J. H., Pandis, S. N., Barnes I., Dentener, F. J., Facchini, M. C., Van Dingenen, R., Ervens, B., Nenes, A., Nielsen, C. J., Swietlicki, E. J., Putaud, P., Balkanski, Y., Fuzzi, S., Horth, J., Moortgat, G. K., Winterhalter, R., Myhre, C. E. L., Tsigaridis, K., Vignati, E., Stephanou, E. G., and Wilson, J.: Organic aerosol and global climate modelling: a review, Atmos. Chem. Phys., 5, 1053–1123, 2005.

Keywood, M. D., Varutbangkul, V., Bahreini, R., Flagan, R. C., and Seinfeld, J. H.: Secondary organic aerosol formation from the ozonolysis of cycloalkenes and related compounds, Environ. Sci. Technol., 38, 4157–4164, 2004.

Kostenidou, E., Kaltsonoudis, C., Tsiflikiotou, M., Louvaris, E., Russell, L. M. and Pandis, S. N.: Burning of olive tree branches: a major organic aerosol source in the Mediterranean. Atmos. Chem. Phys., 13, 8797–8811, 2013.

Kroll, J. H., Ng, N. L., Murphy, S. M., Flagan, R. C., and Seinfeld, J. H.: Secondary organic aerosol formation from isoprene photooxidation, Environ. Sci. Technol., 40, 1869-1877, 2006.

Lambe, A. T., Miracolo, M. A., Hennigan, C. J., Robinson, A. L., and Donahue, N. M.: Effective rate constants and uptake coefficients for the reactions of organic molecular markers (n-alkanes, hopanes and steranes) in motor oil and diesel primary organic aerosols with hydroxyl radicals, Environ. Sci. Technol., 43, 8794−8800, 2009.

Lane, T., Donahue, N. M., and Pandis, S. N.: Simulating secondary organic aerosol formation using the volatility basis-set approach in a chemical transport model, Atmospheric Environment, 42, 7439-7451, 2008.

Matsunaga, A., and Ziemann, P. J.: Gas-wall partitioning of organic compounds in a Teflon film chamber and potential effects on reaction product and aerosol yield measurements, Aerosol Science and Technology, 44, 881–892, 2010.

McMurry, P. H., and Rader, D. J.: Aerosol wall losses in electrically charged chambers, Atmos. Chem. Phys., 4, 249–268, 1985.

Murphy, D. M., Cziczo, D. J., Froyd, K. D., Hudson, P. K., Matthew, B. M., Middlebrook, A. M., Peltier, R. E., Sullivan, A., Thomson, D. S., and Weber, R. J.: Single-particle mass spectrometry of tropospheric aerosol particles, J. Geophys. Res., 111, D23S32, 2006.

Nah, T.; McVay, R. C.; Pierce, J. R.; Seinfeld, J. H.; Ng, N. L.; Constraining uncertainties in particle-wall deposition correction during SOA formation in chamber experiments; Atmos. Chem. Phys., 17, 2297-2310, 2017.

Ng, N. L., Kroll, J. H., Chan, A. W. H., Chhabra, P. S., Flagan, R. C., and Seinfeld, J. H.: Secondary organic aerosol formation from m -xylene, toluene, and benzene, Atmos. Chem. Phys., 7, 3909–3922, 2007.

Pathak, R. K.; Stanier, C. O.; Donahue, N. M.; Pandis S. N.; Ozonolysis of α-pinene at atmospherically relevant concentrations: temperature dependence of aerosol mass fractions (yields); J. Geophys. Res., 112, D03201, 2007.

Platt, S. M., El-Haddad, I., Zardini, A. A., Clairotte, M., Astorga, C., Wolf, R., Slowik, J. G., Temime-Roussel, B., Marchand, N., Ježek, I., Drinovec, L., Močnik, G., Möhler, O., Richter, R., Barmet, P., Bianchi, F., Baltensperger, U., and Prévôt, A. S. H.: Secondary organic aerosol formation from gasoline vehicle emissions in a new mobile environmental reaction chamber. Atmos. Chem. Phys., 13, 9141-9158, 2013.

Pope, C. A., Ezzati, M., and Dockery, D. W.: Fine-particulate air pollution, and life expectancy in the United States, new Engl. J. Med, ,360, 376-386, 2009.

Presto, A. A., Huffhartz, K. E., and Donahue, N. M.: Secondary organic aerosol production from terpene ozonolysis. 1. Effect of UV radiation, Environ. Sci. Technol., 39, 7036–7045, 2005a.

Presto, A. A., Huffhartz, K. E., and Donahue, N. M.: Secondary organic aerosol production from terpene ozonolysis. 2. Effect of NO_x concentration, Environ. Sci. Technol., 39, 7046–7054, 2005b.

Qi, L.; Nakao, S.; Cocker, D. R.; Aging of secondary organic aerosol from α-pinene ozonolysis: Roles of hydroxyl and nitrate radicals; J. Air Waste Manag. Assoc., 62, 1359–1369, 2012.

Robinson, A. L., Donahue, N. M., Shrivastava, M. K., Weitkamp, E. A., Sage, A. M., Grieshop, A. P., Lane, T. E., Pierce, J. R., and Pandis, S. N.: Rethinking organic aerosol: semivolatile emissions and photochemical aging, Science, 315, 1259–1262, 2007.

Stern, J. E.; Flagan R.C.; Grosjean D.; Seinfeld J.H.; Aerosol formation and growth in atmospheric aromatic hydrocarbon photooxidation; Environ. Sci. Technol., 21, 1224-1231, 1987.

Tritscher, T., Dommen, J., DeCarlo, P. F., Gysel, M., Barmet, P. B., Praplan, A. P., Weingartner E., Prévôt, A. S. H., Riipinen, I., Donahue, N. M., and Baltensperger, U.: Volatility and hygroscopicity of aging secondary organic aerosol in a smog chamber, Atmos. Chem. Phys., 11, 11477–11496, 2011.

Tsimpidi, A. P., Karydis, V. A., Zavala, M., Lei, W., Bei, N., Molina, L., and Pandis, S. N.: Sources and production of organic aerosol in Mexico City: insights from the combination of a chemical transport model (PMCAMx-2008) and measurements during MILAGRO, Atmos. Chem. Phys., 11, 5153−5168, 2011.

Weitkamp, E. A., Sage, A. M., Pierce, J. R., Donahue, N. M., and Robinson, A.L.: Organic aerosol formation from photochemical oxidation of diesel exhaust in a smog chamber. Environ. Sci. Technol., 410, 6969–6975, 2007.

Zhang, J., Huff Hartz, K. E., Pandis, S. N., and Donahue, N. M.: Secondary organic aerosol formation from limonene ozonolysis: Homogeneous and heterogeneous influences as a function of NO_x, J. Phys. Chem. A, 110, 11053–11063, 2006.

Zhang, Q., Jimenez, J. L., Canagaratna, M. R., Allan, J. D., Coe, H., Ulbrich, I., Alfarra, M. R., Takami, A., Middlebrook, A. M., Sun, Y. L., Dzepina, K., Dunlea, E., Docherty, K., DeCarlo, P. F., Salcedo, D., Onasch, T., Jayne, J. T., Miyoshi, T., Shimono, A., Hatakeyama, S., Takegawa, N., Kondo, Y., Schneider, J., Drewnick, F., Borrmann, S., Weimer, S., Demerjian, K., Williams, P., Bower, K., Bahreini, R., Cottrell, L., Griffin, R. J., Rautiainen, J., Sun, J. Y., Zhang, Y. M., and Worsnop, D. R.: Ubiquity and dominance of oxygenated species in organic aerosols in anthropogenically-influenced Northern Hemisphere midlatitudes, Geophys. Res. Lett., 34, L13801, 2007.

Zhang, X., Cappa, D. C., Jathar, S. H., McVay, R. C., Ensberg, J. J., Kleeman, M. J., and Seinfeld, J. H.: Influence of vapor wall loss in laboratory chambers on yields of secondary organic aerosol, Proc. Natl. Acad. Sci. U.S.A, 111, 5802-5807, 2014.

Zhao, Y., Hennigan, C. J., May, A. A., Tkacik, D. S., Gouw, J. A. De, Gilman, J. B., Kuster, W. C., Borbon, A., and Robinson, A. L.: Intermediate-volatility organic compounds: a large source of secondary organic aerosol, Environ. Sci. Techno., 48, 13743–13750, 2014.

Chapter 2

Multi-generation chemical aging of α-pinene ozonolysis products by reactions with OH[1]

[1] Published as: Wang, N., Kostenidou, E., Donahue, N. M., and Pandis, S. N.: Multi-generation chemical aging of α-pinene ozonolysis products by reactions with OH, Atmos. Chem. Phys. Discuss., 10.5194/acp-2017-746, 2017.

2.1 Introduction

Anthropogenic activities such as fuel combustion as well as biogenic sources such as emissions from vegetation can introduce particles and particle precursors into the atmosphere. In most areas, about half of the submicron aerosol mass on average is composed of organic compounds (Zhang et al., 2007). Organic particles directly emitted to the atmosphere are traditionally defined as primary organic aerosol (POA), while those formed through atmospheric reactions and condensation of species with corresponding volatility are secondary (SOA). Atmospheric aerosols represent a significant risk to human health by causing respiratory problems and heart attacks (Davidson et al., 2005; Pope et al., 2009). At the same time these particles influence the climate of our planet (Intergovernmental Panel on Climate Change, 2007).

Oxygenated OA with a high oxygen to carbon ratio (O:C) is often the most important component of ambient OA suggesting the importance of atmospheric chemistry in the formation and processing of OA (Zhang et al., 2007). Early studies of SOA formation focused on the first stage of reactions involving the target precursor reacting with the chosen oxidant. In the atmosphere, organic vapors and particles interact with oxidants for days and therefore successive oxidation processes are inevitable.

Chemical aging refers to the subsequent stages of SOA formation and evolution due to the production of later-generation products via oxidation of first-generation products by oxidants such as OH free radicals (Donahue et al., 2006; Henry et al., 2012). Previous studies have explored various forms of aging, including heterogeneous reactions of oxidants and aerosols (George et al., 2008), oligomerization (Kalberer et al., 2006), photolysis of either gas or condensed-phase products (Henry and Donahue, 2012), and homogeneous gas-phase oxidation by OH (Donahue et al., 2012). Homogeneous gas-phase oxidation reactions appear to be in general much faster than

heterogeneous reactions, due to diffusion limitations of the latter (Lambe et al., 2009). The first-generation oxidation reactions of most SOA precursors convert much less than 50 % of the precursor to SOA, leaving more than half of the carbon still in the gas-phase. Additional oxidation of these vapors can potentially contribute additional and more oxygenated SOA components. These later-generation reactions have been proposed to be a major missing step connecting chamber studies to field measurements.

Zeroth order parameterizations have been developed to model the chemical aging of semi-volatile POA emissions in chemical transport models (Robinson et al., 2007). CTMs using these schemes show improved performance in urban areas such as Mexico City (Tsimpidi et al., 2011), but tend to over-predict OA in areas such as the southeastern United States where biogenic VOCs dominate if chemical aging is assumed to be a major source of additional SOA (Lane et al., 2008). As a result, the importance of aging of biogenic SOA as a source of SOA mass concentration remains an issue of debate.

The ozonolysis of α-pinene ($C_{10}H_{16}$) is considered one of the most important global SOA sources (Griffin et al., 1999). The system has been well characterized through smog chamber experiments where researchers quantified its SOA yields under different conditions, explored the reaction pathways and mechanisms, and identified its product distributions. Recent studies suggest that there is significant potential for additional SOA formation from homogeneous gas-phase aging by OH of the first-generation α-pinene oxidation products (Donahue et al., 2012; Müller et al., 2012; Chacon-Madrid et al., 2013). Major identified products existing in gas phase such as pinonaldehyde and pinonic acid can serve as SOA precursors and further react with OH. Pinonaldehyde reacts with OH, with SOA mass yields up to 5 % under low-NO_x conditions and 20 % under high-NO_x conditions (Chacon-Madrid et al., 2013). Müller et al. (2012) demonstrated

the formation of 1,2,3-butanetricarboxylic acid (MBTCA), an SOA product of low volatility identified in α-pinene ozonolysis, through the gas-phase OH oxidation of pinonic acid. They reported an experimental yield of 0.6 % for MBTCA from the gas-phase OH oxidation of pinonic acid, accounting for about 10 % of the total SOA formed. The proposed formation mechanisms of MBTCA is a classic example of semi-volatile precursors going through oxidation and forming products of lower volatility.

The Multiple Chamber Aerosol Chemical Aging Study (MUCHACHAS) explored the gas-phase OH aging effects of the α-pinene ozonolysis products via experiments performed in four different smog chambers (Donahue et al., 2012). They were able to isolate the aging effect by using different OH sources (HOOH photolysis, HONO photolysis, TME ozonolysis), light sources (sunlight, quasi-solar lamps, 350 nm UV lamps), and chambers of different design in size and material (Teflon and aluminum). Almost in all experiments, additional formation of SOA (up to 55 %) and a more oxidized product distribution (increasing O:C) were observed after aging. However, in one of the chambers, strong UV photolysis led to decreasing SOA mass concentrations in experiments with low to moderate OH levels, [OH] $\leq 2\times10^{6}$ molecules cm^{-3} (Henry and Donahue, 2012). These authors concluded that chemical aging involves a complex set of interacting processes with competing functionalization (conserved C number with products of lower volatility and higher oxidation states) and fragmentation (cleavage of C-bond with products over a wide volatility range and higher oxidation states) of the various organic compounds. A 2D-volatility basis set (2D-VBS) simulation based on these two pathways and a branching ratio between them showed that homogeneous OH aging can potentially more than double the α-pinene SOA mass concentration, after about a day's equivalent of typical atmospheric oxidation conditions. Uncertainties such as "ripening" during which SOA volatility evolves but its mass

remains constant, UV photolysis and heterogeneous OH uptake can further complicate the aging process.

Qi et al. (2012) also explored aging of the α-pinene ozonolysis system through smog chamber experiments using HOOH as an OH source and studied the UV photolysis effect. They observed a 7.5 % increase in the SOA volume concentration and an increase of 0.03 in the O:C after aging. Minimum photolysis effect was reported for these experiments.

One complication of chamber experiments is the interaction of particles with chamber walls. The wall-loss rate of particles is a function of particle size, charge distribution, chamber geometry, turbulence, and electric field within the chamber (Crump and Seinfeld, 1981). In order to quantify SOA yields from chamber experiments, it is important to correct for particle wall loss. Recent findings that organic vapors in the chamber can be directly lost to the Teflon walls as well further complicate the wall-loss correction process (Matsunaga and Ziemann, 2010; Zhang et al., 2014). Krechmer et al. (2016) measured the loss rate of vapors formed in the chamber and found the corresponding timescale to be 7-13 min. Ye et al. (2016) determined the vapor wall-loss timescale in the Carnegie Mellon chamber used in this work to be around 15 min for semi-volatile organic compounds.

Despite the consensus from the aforementioned chamber studies that gas-phase OH aging of α-pinene ozonolysis products can contribute to additional SOA formation, there lacks consistency in the extent to which the additional mass can form for different OH exposures. Part of the problem is that the estimated amount of additional SOA formed from these long-lasting aging experiments can be extra sensitive to the particle and the vapor wall-loss correction methods deployed. The uncertainties at the end of a 10-hour long aging experiment during which most particles are lost to chamber walls and the measured suspended mass is low can be relatively high.

In this work, we aim to quantify the additional SOA formed during the aging step comparing measurements from a suite of instrumentation. We adopt a size-dependent particle wall-loss correction method and develop a procedure to better constrain the associated errors. We also attempt to constrain the vapor loss using both theoretical calculations and measurements.

2.2 Experimental approach

We conducted experiments in a 12 m^3 Teflon (Welch Fluorocarbons) smog chamber at Carnegie Mellon University (CMU). The reactor was suspended in a temperature-controlled room with walls covered with UV lights (GE 10526 and 10244). Prior to each experiment, we flushed the chamber overnight with purified air under UV illumination to remove any residual particles and gas-phase organics. We generated purified air by passing ambient air through a high-efficiency particulate air (HEPA) filter to remove particles, an activated carbon filter to remove any organics, a Purafil filter to remove NO_x, and finally a silica gel filter, keeping relative humidity (RH) below 5 % in the chamber before each experiment.

We pumped an ammonium sulfate solution (1 g L^{-1}) into the chamber at the beginning of each experiment through an atomizer (TSI, model 3076) at a constant rate of 90 mL h^{-1} to produce droplets. The droplets passed through a diffusion dryer and a neutralizer to produce dry ammonium sulfate seed particles. We injected seeds with a number mode size of 110 nm until they reached a number concentration of 2×10^4 cm^{-3}, resulting in an initial seed mass concentration of around 40 µg m^{-3} and a surface area concentration of up to 1000 μm^2 cm^{-3}. Typical organic vapors with a molar weight of 250 g mol^{-1} thus had an initial collision frequency with these seeds of 0.01 s^{-1}. We injected α-pinene (Sigma-Aldrich, ≥ 99 %) into the chamber using a septum injector with purified air as carrier flow. We generated ozone using a corona-discharge ozone generator (AZCO,

HTU500AC) to initiate the ozonolysis reaction. We prepared a fresh HONO solution in a bubbler by adding a 4.9 g L^{-1} sulfuric acid solution to a 6.9 g L^{-1} sodium nitrite solution. We then turned on the UV lights to start the photo-dissociation of HONO, producing OH.

At the end of each experiment, we injected additional ammonium-sulfate seeds into the chamber using the same method with a more concentrated solution (5 g L^{-1}) in order to characterize the particle wall-loss rates a second time.

We added butanol-d9 (Cambridge Isotope Laboratories, 98 %) into the chamber through the septum injector as an OH tracer before the reaction started and used the method described in Barmet et al. (2012) to calculate the OH produced by HONO photolysis. The OH concentration in these experiments was around 2.4×10^7 molecules cm^{-3} for the first hour, then dropped to around 5×10^6 molecules cm^{-3} afterwards. The introduction and photolysis of HONO produces hundreds of ppb of NO_x, and thus the aging reactions in this work occurred under high NO_x conditions; the majority of the peroxy radicals reacted with NO during the aging phase of the experiments.

We performed experiments at both low RH of less than 20 % and intermediate RH of 50 %. To add water vapor to the chamber, we used a stream of purified air to carry ultrapure water (Millipore water purification system) in a bubbler into the chamber before the introduction of seeds.

We measured the particle size distribution using a TSI Scanning Mobility Particle Sizer, SMPS (classifier model 3080; CPC model 3010 or 3772), with flows adjusted to measure particle diameters in the 15-700 nm range. We measured the particle composition and mass spectrum of the OA with an Aerodyne High Resolution Time-of-flight Aerosol Mass Spectrometer (HR-Tof-AMS). We monitored the concentrations of α-pinene and butanol-d9 using a Proton Transfer Reaction-Mass Spectrometer (PTR-MS, Ionicon), the ozone concentration using a Dasibi 1008 ozone monitor (ICE: Teledyne 400E), and NO_x (NO + NO_2) levels using a Teledyne API NO_x

Analyzer 200A (ICE: Teledyne T201). We held the chamber temperature constant at 22 ^{o}C throughout all experiments. We list the initial conditions of the experiments performed for this work in Table 2.1.

Table 2.1: Initial conditions of the α-pinene ozonolysis aging experiments.

Experiment	**α-pinene** (ppb)	**O_3** (ppb)	**Initial seed surface area** (μm^2 cm^{-3})	**RH** (%)	**OH[a]** ($\times 10^7$ molecules cm^{-3})	**OH introduction time** (h after α-pinene consumption)
1	33	450	850	<20	2.4	0.3
2	14	600	760	<20	2.7	0.8
3	35	450	720	<20	2.0	1.1
4	16	500	950	<20	2.4[b]	1.1
5	20	400	710	~50	2.7	0.8

[a]The OH concentration was calculated using the decay of butanol-d9 (monitored by PTRMS) (Barmet et al., 2012).

[b]Estimated OH concentration for Exp. 4 based on the other experiments. The PTRMS data was not available during that time for Exp. 4.

2.3 Data analysis

2.3.1 SOA yields

The SOA mass yield, *Y*, is a metric of the ability of a gaseous precursor to form SOA, and is defined as $Y = C_{SOA}/\Delta VOC$, where C_{SOA} is the produced SOA mass concentration (in $\mu g\ m^{-3}$) and ΔVOC the amount of the VOC precursor (α-pinene in this case) reacted (in $\mu g\ m^{-3}$). To separate the effect of aging on SOA mass concentration, we define a first-generation SOA mass yield, $Y_1 = C_{SOA,1}/\Delta VOC$, and a second-generation SOA mass yield, $Y_2 = C_{SOA,2}/\Delta VOC$. $C_{SOA,1}$ and $C_{SOA,2}$ are the concentrations of SOA formed before, and after aging with hydroxyl radicals. All α-pinene reacts away during the first stage and thus ΔVOC for the second stage is the same as the initial α-pinene concentration in the chamber.

2.3.2 Particle wall-loss correction

In this work, we try to reduce the uncertainties in the estimated SOA mass concentration associated with the particle wall-loss correction. This uncertainty can be significant due to two aspects of these aging experiments: the evolution of the particle size distribution and the duration of the experiments. In these aging experiments, where particles grow by condensation and coagulation for several hours, the particle size distribution can potentially shift, covering a wide size range over the course of an experiment. Particle wall losses are size dependent, and this shift can introduce significant errors if a constant loss rate constant is assumed. To minimize these problems, we adopted a size-dependent particle wall-loss correction method where we determined the particle wall-loss rate constant, *k*, at each particle size, D_p.

The size-dependent particle wall-loss correction method (Keywood et al., 2004; Ng et al., 2007; Loza et al., 2012; Nah et al., 2016) adopted in this work is based on the SMPS-measured particle size distribution. At each particle size bin *i*, the first-order particle wall-loss rate constant *k*, can be determined as the slope of the following equation:

$$\ln[N_i(t)] = -k_i t + Q \quad (1)$$

where $N_i(t)$ is the SMPS-measured aerosol number concentration at size bin *i* and *Q* is an arbitrary constant. Applying Eqn. 1 across the entire SMPS-measured particle size range, we obtain the particle wall-loss rate constant function, $k(D_p)$.

To determine the $k(D_p)$ profile, we utilized the initial four-hour ammonium sulfate seed wall-loss period for each experiment. Since *k* may also vary with time (McMurry and Rader, 1985), we determined a second $k(D_p)$ profile for each experiment using the ammonium sulfate seed wall-loss period at the end. It is important to ensure that the *k*'s, especially at sizes where the majority of SOA mass is distributed, remain the same over the course of each experiment.

The $k(D_p)$ values calculated (with an R^2>0.5) based on SMPS measurements of the seed distribution from this work usually only cover particle size range of 30-300 nm due to the lack of particles at either end of the particle size distribution. To determine the $k(D_p)$ for D_p<30 nm, we use a simple log-linear fit of *k*'s from 30-50 nm and back extrapolate it to 10 nm. To determine $k(D_p)$ for D_p > 300 nm, we assume that the constant is practically the same in the 300-700 nm range. We confirmed this with additional seed-only experiments where there were enough particles at that size range (Wang et al., 2017). Significant increases of the rate loss constant are observed for particles larger than 1 μm, while in our experiments the particles remained small than 600 nm or so. A measure of the uncertainty of these corrections is the variability of the corrected mass concentration during the seed wall-loss periods as discussed in the next section. Details regarding the wall-loss profiles in the CMU chamber and the execution of the size-dependent particle wall-loss correction for this work can be found in Wang et al. (2017).

The corrected particle number concentration at each size bin *i*, $N_i(t)$, can be calculated numerically,

$$N_i(t) = \mathrm{N}_i^m(t) + k_i \int_0^t \mathrm{N}_i^m(t)dt, \quad (2)$$

from the measured values $\mathrm{N}_i^m(t)$ and the $k(D_p)$ corresponding to the size bin *i*, k_i.

For closed systems in which coagulation is slow, the particle wall-loss corrected number concentration should be constant. In order to evaluate how well the correction works, we define the parameter: $\varepsilon_N = 2\sigma_{N_s}/\overline{N_s}$, where σ_{N_s} is the standard deviation of the particle wall-loss corrected number concentration for the seed wall-loss periods and $\overline{N_s}$ the average. Similarly, we define $\varepsilon_V = 2\sigma_{N_s}/\overline{V_s}$ based on the particle wall-loss corrected volume concentration for the two seed wall-loss periods. Only when all four values, ε_N and ε_V for both the initial and the final seed periods, are less than 5 % do we deem the particle wall-loss correction valid for that individual

experiment. Experiments in which these criteria were not met were not included in the analysis.

To calculate the mass concentration of the formed SOA, C_{SOA}, during the course of an experiment, we treated the particle wall-loss corrected aerosol volume concentration V(t) differently before and after its maximum, V_{max} . For

$$\mathrm{t} < t_{V_{max}},\ C_{SOA}(t) = (V(t) - V_s)\rho_{SOA},$$

$$\mathrm{t} \geq t_{V_{max}},\ C_{SOA}(t) = [V(t) - V_s \frac{V(t)}{V_{max}}]\rho_{SOA}, \quad (3)$$

where $t_{V_{max}}$ is the corresponding time at the maximum particle wall-loss corrected total aerosol volume concentration. V_s is the average particle wall-loss corrected seed volume concentration before the beginning of each experiment. ρ_{SOA} is the SOA density, assumed to be equal to 1.4 μg m^{-3} (Kostenidou et al., 2007). Ideally, V(t) should equal to V_{max} after the reactions are completed and particle wall loss is the only process after $t_{V_{max}}$. However, deviations of V(t) from V_{max} are caused by the uncertainty associated in applying the size-dependent wall-loss corrections. By scaling V_s with V(t)/V_{max}, we are distributing the impact of any potential fluctuations in V(t) evenly to both the seeds and the organics, and thus obtain a more stable C_{SOA} after aging.

2.3.3 Analysis of AMS measurements

The HR-AMS was operated in V mode during the experiments in this work. Squirrel v1.56D was used to analyze the data. The atomic oxygen to carbon ratio, O:C, was determined based on the unit-resolution correlation described in Caragaratna et al. (2015). Nitrate signals were attributed to organics since the only sources of them in these experiments are organonitrates.

In an attempt to explore the functionalities/products that may have changed during aging, we used the AMS high-resolution (HR) family analysis. We used Pika 1.15D to analyze the HR data. Each fitted ion is grouped into a "family" based on their chemical formula, and the families used are:

CH, CHO, CHO_2, C_x, HO, and NO. These are the main components of the organics formed, with family HO calculated by subtracting the concentrations of the other families from the total organic signal. This is necessary because the fragmentation of sulfates can interfere with the family HO. Family NO can be used to represent the organonitrates formed during the aging phase of the experiments.

2.4 Results and discussion

The particle wall-loss corrected aerosol number concentration evolution during a typical experiment (Exp. 1) together with the SMPS raw measurements are shown in Fig. 2.1. Prior to the ozonolysis, 18,000 cm^{-3} ammonium sulfate particles were added to the chamber as seeds. After a 4.5 h wall-loss period, 8,000 cm^{-3} particles remained suspended, serving as pre-existing surface for condensation. At t=0, ozone was added into the chamber, reacting with α-pinene to form condensable first-generation products. The ozonolysis of α-pinene has been found to produce OH with a molar yield of approximately 0.7 (Paulson et al., 1998), which in our experiments resulted in approximately one third of the precursor reacting with OH. An additional 100 cm^{-3} particles were formed due to nucleation at this time. Two doses of HONO were added into the chamber in this experiment at t=0.4 h and t=1.3 h, respectively. HONO was allowed to mix in the chamber and then the UV lights were turned on at t=0.8 h and t=1.8 h to produce OH. At t=3.5 h, another 10,000 cm^{-3} ammonium sulfate particles were added into the chamber for a second 4 h long determination of the $k(D_p)$ profile for this experiment.

The two $k(D_p)$ profiles determined from the initial seed wall-loss period and the one at the end of the experiment are shown in Fig. 2.2. They agree relatively well with small discrepancies at $D_p < 50$ nm. The complete $k(D_p)$ profile used for the size-dependent particle wall-loss correction

is also shown.

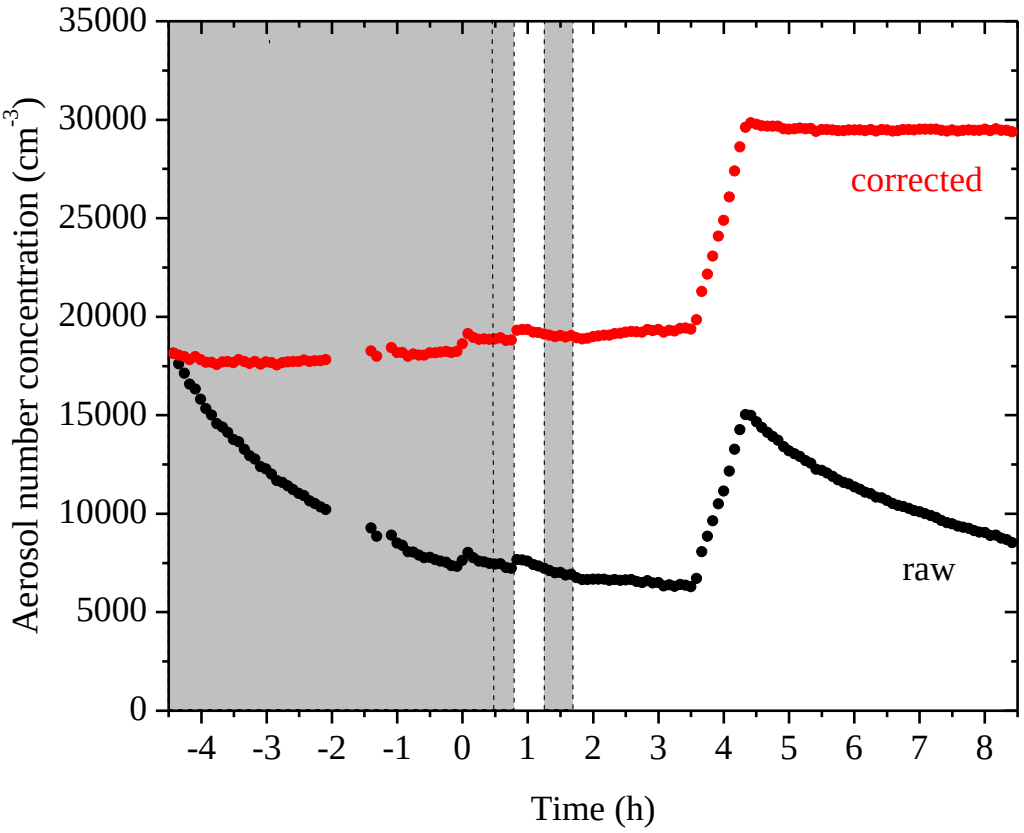

Figure 2.1: SMPS-measured (black symbols) and the size-dependent particle wall-loss corrected (red symbols) aerosol number concentration evolution during a typical experiment (Exp. 1). Ozone was added into the chamber at time zero to initiate α-pinene ozonolysis. The shaded areas indicate that the chamber was dark. The dashed lines mark the beginning and the end of the two times HONO were added, respectively. The increase in number concentration at t=3.5 h is due to the injection of 5 g L^{-1} ammonium sulfate particles. An additional 100 cm^{-3} particles were formed due to nucleation both at the ozonolysis step and the aging step. Data were not recorded from t=-2 h to -1.4 h.

As indicated in Fig. 2.1, the particle wall-loss corrected aerosol number concentration remains relative level at t<0 h and t>3.5 h, with $\varepsilon_{N,1} = 3.3$ % and $\varepsilon_{N,2} = 0.5$ %, respectively. The particle wall-loss corrected aerosol volume concentration (Fig. 2.3) at the initial seed wall-loss

period and that at the end had variabilities equal to $\varepsilon_{V,initial} = 4.2\,\%$ and $\varepsilon_{V,end} = 3.8\,\%$, respectively. All parameters were less than 5 % and therefore the accuracy of the wall-loss correction was acceptable.

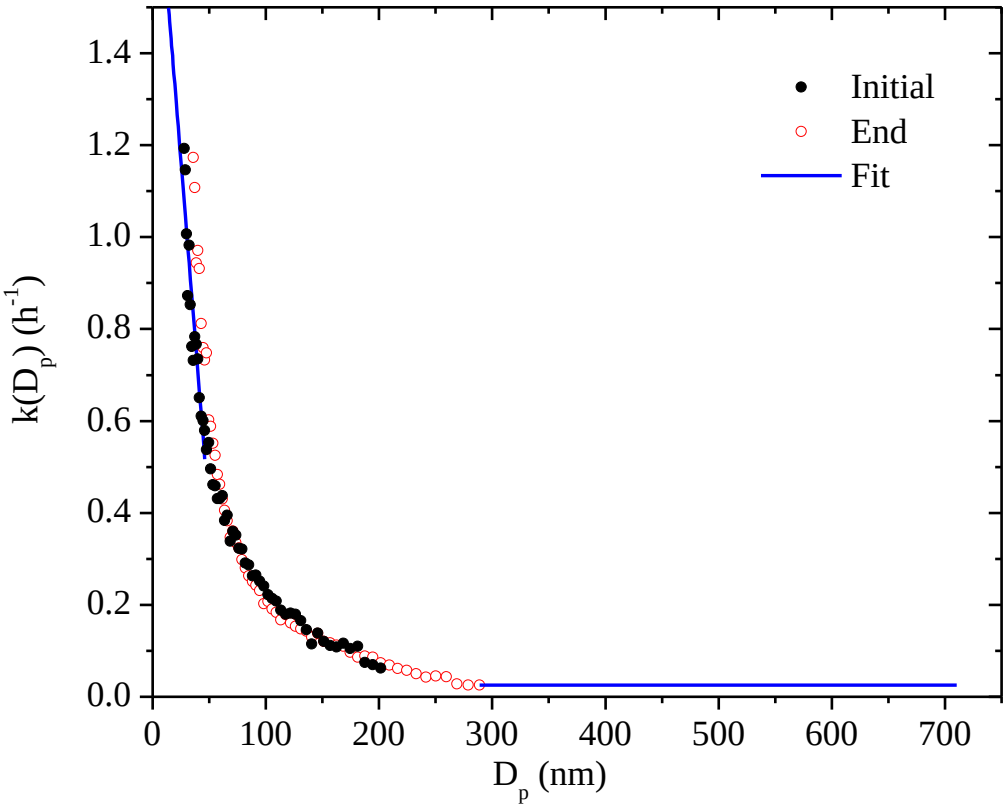

Figure 2.2: The size-dependent particle wall-loss rate constant profile, $k(D_p)$, for Exp. 1. The black symbols are the rate constants calculated based on the wall-loss process of the initial ammonium sulfate seed particles from t=-4.5 h to t=0 h, while the red open symbols those of the additional ammonium sulfate particles at the end from t=4.5 h to t=8.5 h. The blue line is the fit determined.

The particle wall-loss corrected aerosol volume concentration evolution for Exp. 1 together with the corresponding SMPS raw measurements are shown in Fig. 2.3. Particles grew from t=0 to 0.7 h and t=0.8 to 1 h due to vapor condensation. The total aerosol volume peaked at t=0.7 h

during the first-generation oxidation, and reached its maximum at *t*=1.1 h due to aging during the second-generation oxidation. The change in volume during the second addition of OH at 1.7 h was negligible.

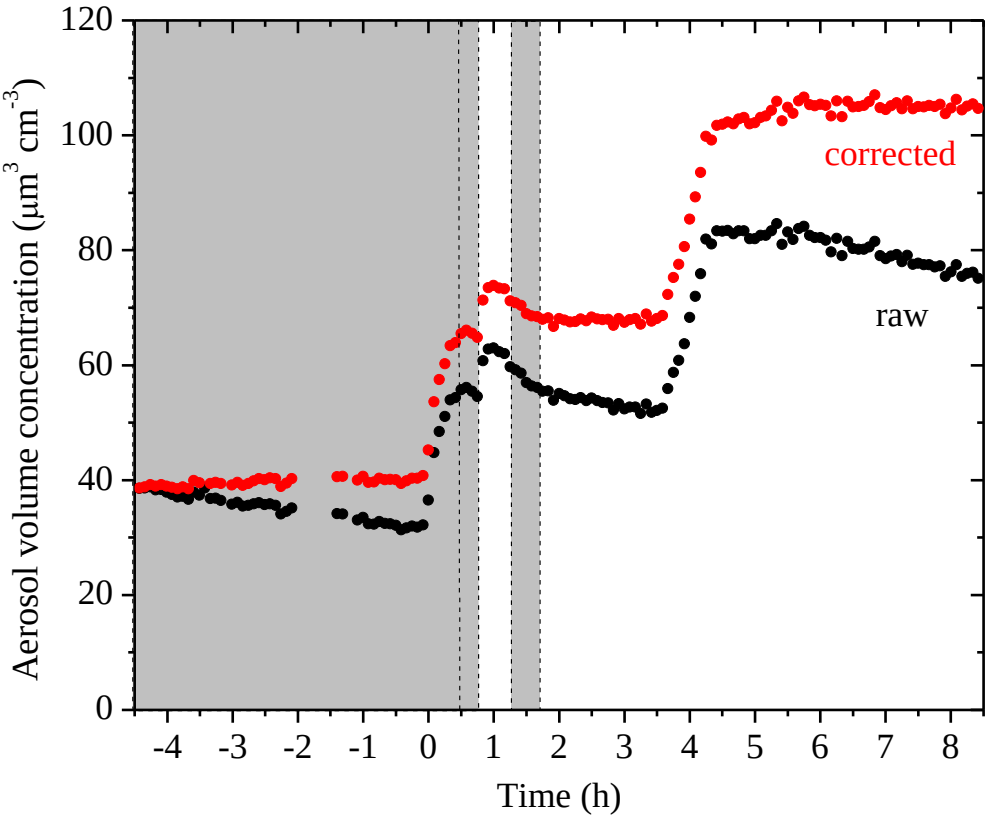

Figure 2.3: SMPS-measured (black symbols) and the size-dependent particle wall-loss corrected (red symbols) aerosol (seed and organic) volume concentration evolution during a typical experiment (Exp. 1). Ozone was added into the chamber at time zero to initiate α-pinene ozonolysis. The shaded areas indicate that the chamber was dark. The dashed lines mark the beginning and the end of the two times HONO were added, respectively. 5 g L^{-1} ammonium sulfate particles were injected into the chamber at *t*=3.5 h. Data were not recorded from *t*=-2 h to -1.4 h.

The SOA mass concentration evolution for Exp. 1 calculated using Eqn. 3 is shown in Fig. 2.4. The error bars are calculated using the highest ε (in this case $\varepsilon_{V,1} = 4.2\,\%$). For this experiment, 37.7±1.6 μg m^{-3} of SOA was formed during ozonolysis. An additional 11.1±2.6 μg

m^{-3} SOA was formed during the first aging period. The SOA reached 48.8±2 μg m^{-3} after aging and remained approximately constant until the end of the experiment. The total SOA produced and the calculated SOA yields for all experiments are listed in Table 2.2.

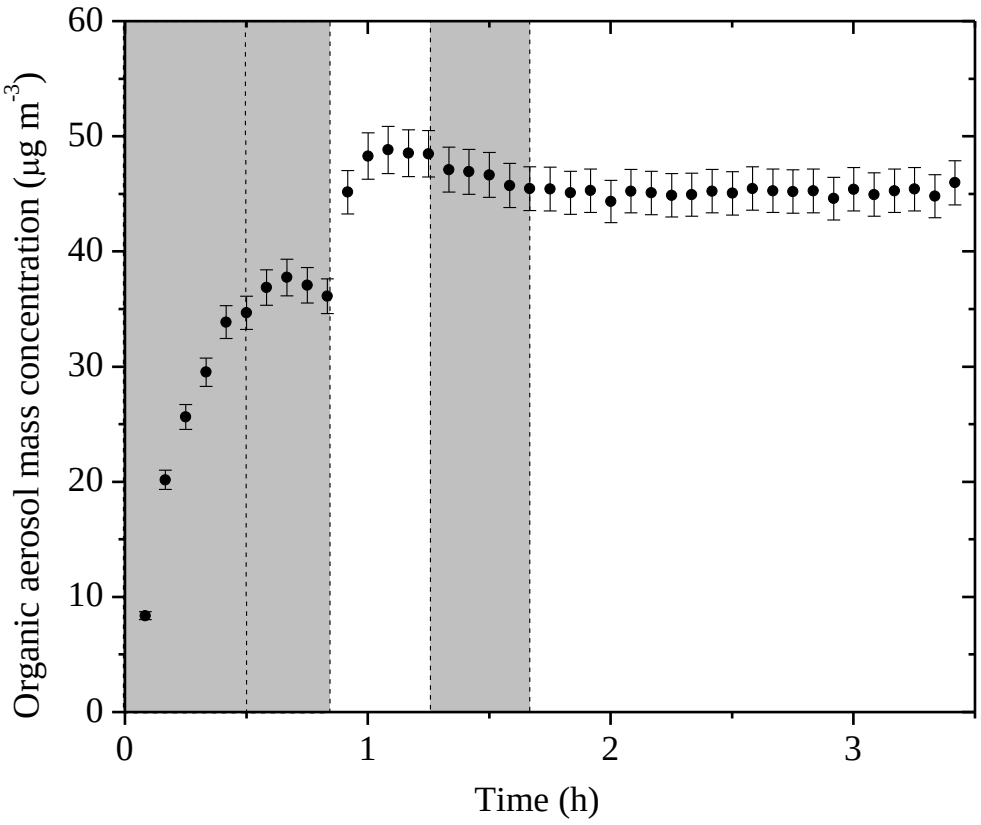

Figure 2.4: The particle wall-loss corrected SOA mass concentration (ρ=1.4 g cm^{-3}) evolution for Exp. 1 derived from SMPS measurements. The corresponding error shown is due to the particle wall-loss correction. Ozone was added into the chamber at time zero to initiate α-pinene ozonolysis. The shaded areas indicate that the chamber was dark. The dashed lines mark the beginning and the end of the two times HONO were added, respectively.

The AMS-derived atomic oxygen to carbon ratio (O:C) evolution for Exp. 1 is shown together with the AMS-measured aerosol composition (assuming CE=1) in Fig. 2.5. The increase in the sulfate signals at *t*=0 is caused by a change in the instrument collection efficiency. Due to

the uncertainty caused by CE changes over the course of an experiment, we did not use the absolute AMS-measured organic mass concentration for any quantitative analysis. Using the algorithm derived by Kostenidou et al. (2007), we calculated the CE to be ~0.25 for the initial seed period and ~0.4 after the seeds were coated with organics. A quick check comparing the two stepwise increase in the CE-corrected organic mass concentration to those derived from SMPS revealed that the results from both instrument agreed reasonably well. The algorithm also estimated that the SOA density was 1.3±0.15 g cm^{-3} in good agreement with the Kuwata et al. (2012) parameterization based on the measured O:C and H:C which also predicted 1.3 g cm^{-3}.

Table 2.2: SOA mass concentration and yields of the α-pinene ozonolysis aging experiments.

Experiment	$C_{SOA,1}$ (μg m^{-3})	Y_1 (%)	$C_{SOA,2}$ (μg m^{-3})	Y_2 (%)	**ΔOA** (%)	**Δ[Org/Sulf]** (%)
1	37.7±1.6	20.6±0.9	48.8±2.0	26.7±1.1	29.4±6.9	27.0±5.8
2	16.7±0.9	21.5±1.2	18.3±1.0	23.5±1.3	19.8±8.1	18.1±2.9
3	57.1±1.3	29.4±0.7	71.0±1.6	36.2±0.8	23.5±3.6	19.1±3.6
4	16.8±0.6	19.1±0.6	20.8±0.7	23.7±0.8	24.0±5.3	21.9±2.1
5	22.2±0.7	19.5±0.6	25.4±0.8	22.3±0.7	20.5±4.7	21.2±4.4

The O:C is a collective measure for the ongoing chemistry during these aging experiments. In Exp. 1, the O:C kept decreasing due to the freshly-formed semi-volatile SOA condensing onto particles from *t*=0 to 0.5 h. Later during the dark period (*t*=0.5 h to 0.8 h), the O:C ratio kept decreasing to 0.42 while the organic mass concentration stayed almost constant. This is consistent with the "ripening" phenomenon, first observed during the MUCHACHAS campaign, where the

composition of the formed SOA keeps evolving after α-pinene has reacted while the change in SOA mass is minimal (Tritscher et al., 2011). The nature of this process is not well-understood, but it probably involves heterogeneous reactions.

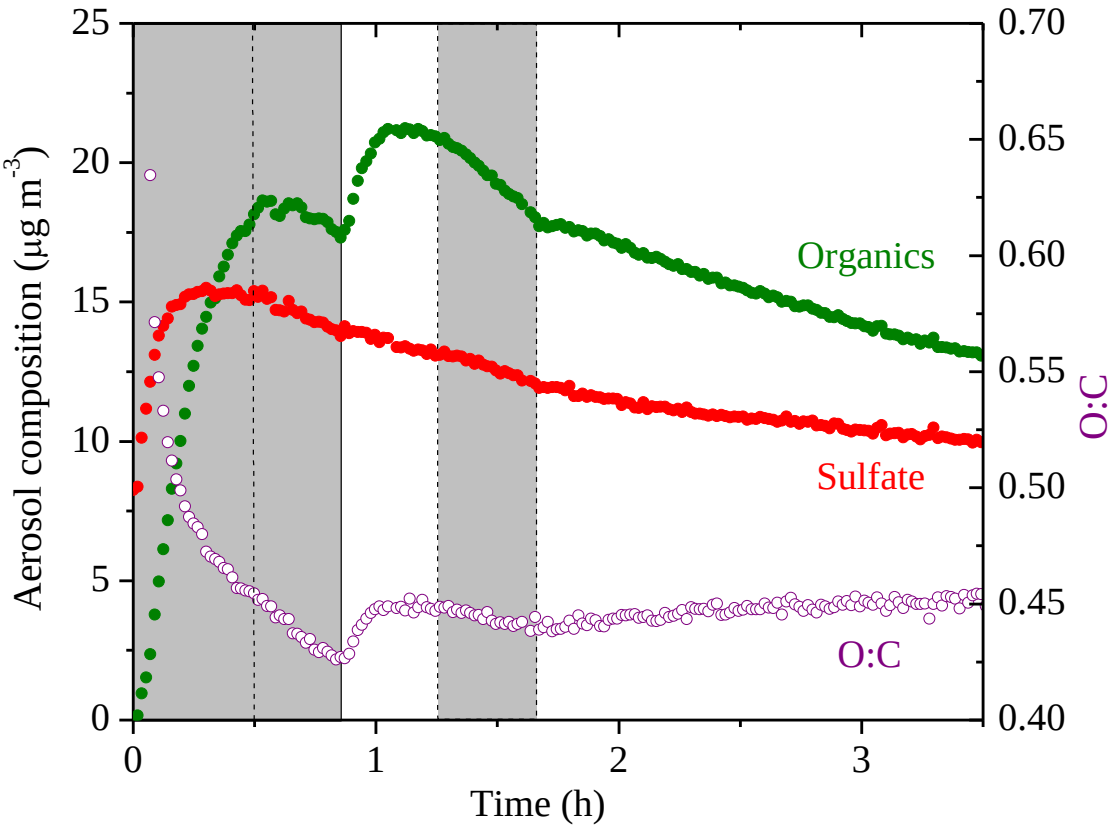

Figure 2.5: The AMS-measured aerosol composition (CE=1) (left axis) and the atomic oxygen to carbon ratio (right axis) evolving with time for Exp. 4. The increase in the sulfate signal at *t*=0 is the result of a change in the collection efficiency (CE). Ozone was added into the chamber at time zero to initiate α-pinene ozonolysis. The shaded areas indicate that the chamber was dark. The dashed lines mark the beginning and the end of the two times HONO were added, respectively.

After OH radicals were generated in the chamber at *t*=0.8 h, the semi-volatile vapors got oxidized to form second-generation products of lower volatility, resulting in an increase of 0.02 in O:C in about 10 min. After *t*=1 h, the O:C remained relatively constant but it started to decrease at *t*=1.25

h when the UV lights were turned off. Since aging is a complex process that involves functionalization, fragmentation and heterogeneous reactions, the trends in O:C are indicative of the competition among these processes. The decrease we observed here was associated with turning the UV lights off, and thus it is likely that some chemistry was perturbed and thus the processes resulting in decreasing O:C took over. The decrease in O:C associated with turning off the UV lights was not consistent across the five experiments. This further proves that this phenomenon is the result of several competing process and needs further investigation on a molecular level. An inflection point at t=1.7 h was observed after a second dose of OH being introduced in the chamber. Instead of the stepwise increase like the one observed after the first dose of OH, the O:C increased slowly but steadily this time until the end of the experiment to 0.45 with no significant increase in organic mass. This is also quite consistent with what was observed in MUCHACHAS.

We used the organic to sulfate ratio (Org/Sulf) derived from AMS measurements to look at the SOA formation in these experiments due to its insensitivity to changes in collection efficiency. The Org/Sulf time series for Exp. 1 is shown in Fig. 2.6. The ratio increased to 1.25 at t=0.7 h as the result of the first-generation vapors condensing onto pre-existing particles. After we first turned on the UV lights, a stepwise increase in the ratio was observed and reached the maximum value of 1.60 at t=1.1 h as a result of the second-generation oxidation chemistry. After that, the ratio kept decreasing. A small bump was observed after the second introduction of OH and then the ratio kept decreasing. One possible explanation for this continuous decrease is the effect of the size-dependent particle wall-loss process. The faster removal of smaller particles (which contain more SOA than sulfate) than that of the bigger ones (which have a lower SOA to sulfate ratio) can lead to a decrease of the overall organic to sulfate ratio.

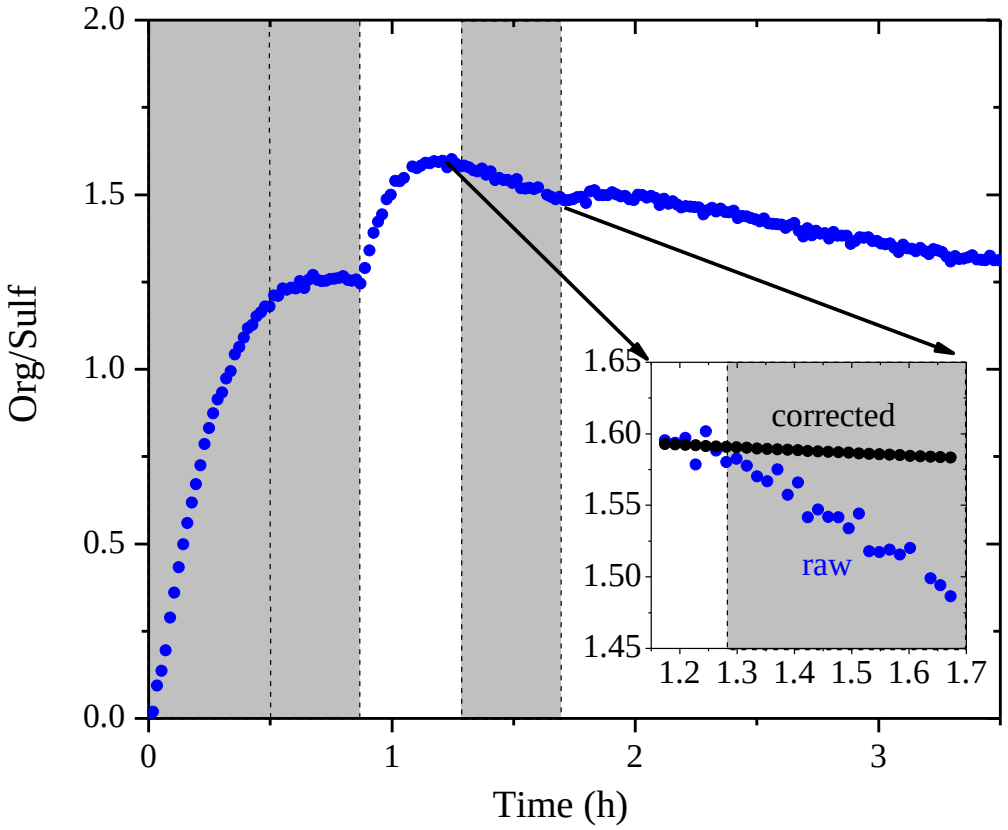

Figure 2.6: The AMS-derived organic to sulfate ratio time series for Exp. 1. The inset is a blow-up of the Org/Sulf ratio from its maximum until the second time when the UV lights were turned on. The black symbols are the particle wall-loss corrected Org/Sulf during that half hour. Ozone was added into the chamber at time zero to initiate α-pinene ozonolysis. The shaded areas indicate that the chamber was dark. The dashed lines mark the beginning and the end of the two times HONO were added, respectively.

Fig. 2.7 shows the size dependence of the Org/Sulf, together with the mass distribution of both organic and sulfate for Exp. 1. The Org/Sulf decreased dramatically from 10 to 1 over the particle vacuum aerodynamic diameter (D_{va}) range of 200 – 500 nm, indicating strong composition dependence on particle size. Since the majority of the mass is distributed in this range, the size-dependent particle wall-loss rate can contribute significantly to the decrease observed in Fig. 2.6 after the Org/Sulf reached its maximum.

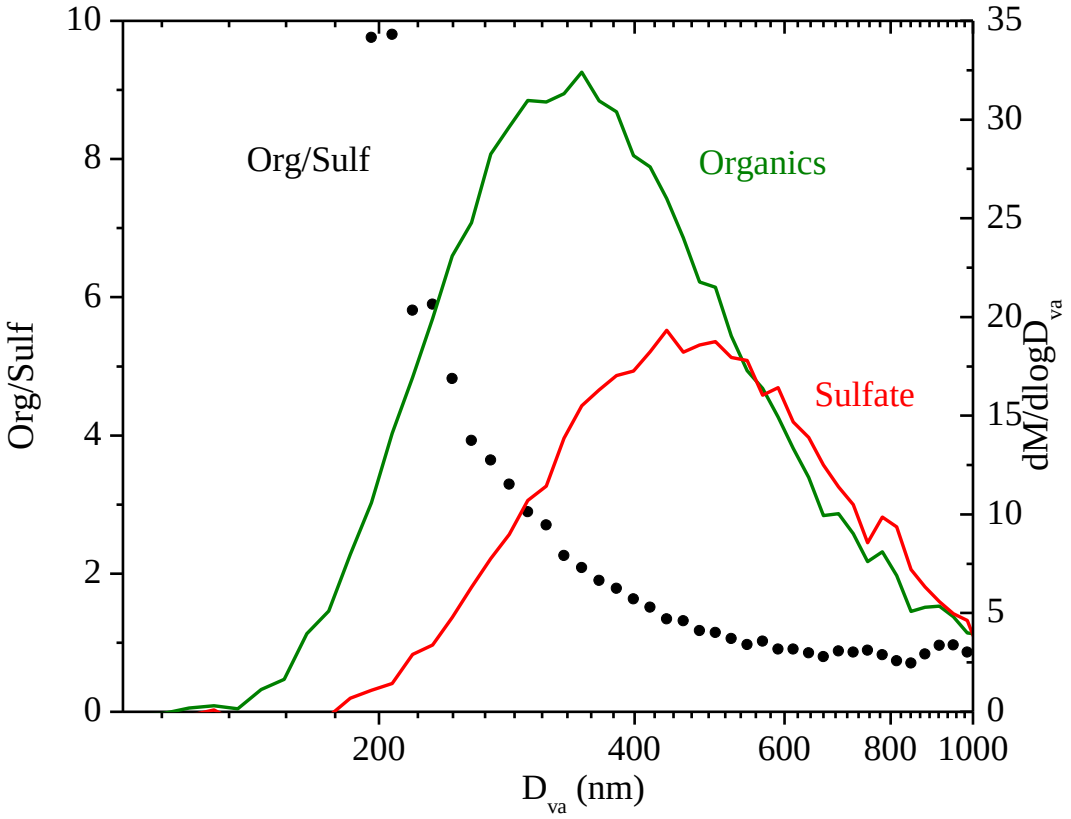

Figure 2.7: The dependence of the AMS-derived organic to sulfate ratio on particle vacuum aerodynamic diameter for Exp. 1 (left axis). Also shown are the AMS-measured organic (green) and sulfate (red) mass distribution (right axis). The results are based on PToF data averaged over ~2.5 hours (t=1.1 h to 3.5 h).

2.4.1 Effect of size-dependent losses on the organic to sulfate ratio

To quantify the effect of the size-dependence of the particle wall-loss process on the organic to sulfate ratio, we discretized the AMS-measured mass distribution $M(D_p)$ into 10 bins in the particle diameter space and defined a mass-weighted particle wall-loss rate constant for each species j, $\bar{k}_j$, as

$$\bar{k}_j = \sum_{i=1}^{10} M_{ij} k_i \,/\, \sum_{i=1}^{10} M_{ij} \quad (4)$$

where M_{ij} is the aerosol mass concentration of species j for size bin i and k_i is the averaged $k(D_p)$

across size bin *i*. Note that the particle diameter used in this section refers to the SMPS-measured mobility equivalent diameter D_p. The particle vacuum aerodynamic diameters derived from the AMS measurements have been converted to D_p using an SOA density of 1.4 μg m^{-3}.

From Eqn. 4 we are able to determine a mass-weighted particle wall-loss rate constant for sulfate, $\bar{k}_{SO_4}$, and for organics, $\bar{k}_{Org}$. For the period after completion of the reactions and if there are only particle losses to the walls the Org/Sulf ratio should satisfy:

$$(\mathrm{Org/Sulf})(t) = (\mathrm{Org/Sulf})_m(t)\exp\left(\bar{k}_{SO_4} - \bar{k}_{Org}\right)t \quad (5)$$

where $(\mathrm{Org/Sulf})_m(t)$ is the AMS-measured and $(\mathrm{Org/Sulf})(t)$ the loss-corrected organic to sulfate ratio.

We can test if indeed the particle wall losses are responsible for the decreasing ratio in Exp. 1 focusing on the period from $t_1 = 1.2$ h to $t_2 = 1.7$ h (Fig. 2.6). In this example t_1 corresponds to the maximum Org/Sulf and t_2 is the second time in which the UV lights were turned on. Applying Eqn. 4, we found the mass-weighted particle wall-loss rate constant for organics, $\bar{k}_{Org} = 0.06\ h^{-1}$, and for sulfate, $\bar{k}_{SO_4} = 0.05\ h^{-1}$. The black line in the inset graph of Fig. 2.6 indicates the particle wall-loss corrected Org/Sulf for the chosen time period using Eqn. 5. The loss-corrected ratio remained relatively constant indicating that the size-dependent particle wall-loss process coupled with the different size distributions of the sulfate and organics were causing the decrease in the ratio. This exercise was repeated for the other experiments arriving in the same conclusion.

2.4.2 Effect of chemical aging on additional SOA formation

To quantify aging effects based on the SMPS measurements, we define the fractional change in the particle wall-loss corrected SOA mass concentration after aging, Δ[OA] , as:

$$\Delta[\mathrm{OA}] = (C_{\mathrm{SOA},2} - C_{\mathrm{SOA,UV}})/C_{\mathrm{SOA},1}, \quad (6)$$

where $C_{\mathrm{SOA,UV}}$ is the particle wall-loss corrected aerosol mass concentration at the time when we first turned on the UV lights. $C_{\mathrm{SOA,\ UV}}$ can be equal to $C_{\mathrm{SOA},1}$ depending on how level the first-generation SOA mass concentration remains after wall-loss correction. Fig. 2.8 summarizes the Δ[OA] for all five experiments with the values and corresponding errors listed in Table 2.2. The OH exposure resulted in an average increase of 24±6 % in SOA mass concentration after aging, ranging from 20 to 29 %. Our HONO injection method creates OH levels of about 2.4×10^7 molecules cm^{-3} for the first hour and then the concentration dropped to around 5×10^6 molecules cm^{-3}. The OH exposure is equivalent to 2-4 days of typical atmospheric oxidation conditions, assuming an OH concentration of 2×10^6 molecules cm^{-3}. The uncertainties displayed in Fig. 2.8 were propagated from uncertainties in the SOA mass concentration.

To quantify aging effects based on the AMS data, we define the fractional change in the organic to sulfate ratio:

$$\Delta[\mathrm{Org/Sulf}] = ([\mathrm{Org/Sulf}]_2\text{-}[\mathrm{Org/Sulf}]_{\mathrm{UV}})/[\mathrm{Org/Sulf}]_{1,} \quad (7)$$

where $[\mathrm{Org/Sulf}]_{\mathrm{UV}}$ refers to the organic to sulfate ratio at the time when we first turned on the UV lights, $[\mathrm{Org/Sulf}]_1$ the maximum before we first turned on the UV lights and $[\mathrm{Org/Sulf}]_2$ the maximum after the OH exposure. Fig. 2.8 summarizes the Δ[Org/Sulf] calculated for all five experiments with the values and corresponding errors listed in Table 2.2. The uncertainties are based on the deviation between the measured and the corrected Org/Sulf (Fig. 2.6 inset) over the chosen time period. An associated error is calculated respectively for $[\mathrm{Org/Sulf}]_{\mathrm{UV},}$ $[\mathrm{Org/Sulf}]_1$ and $[\mathrm{Org/Sulf}]_2$. The reported error for Δ[Org/Sulf] in Table 2.2 is the propagated results of the three. For experiments in this work, the percent increase in organic to sulfate ratios ranged from 18 to 27 % with an average increase of 21±4 %. The values are fairly consistent with the SMPS-derived

Δ[OA].

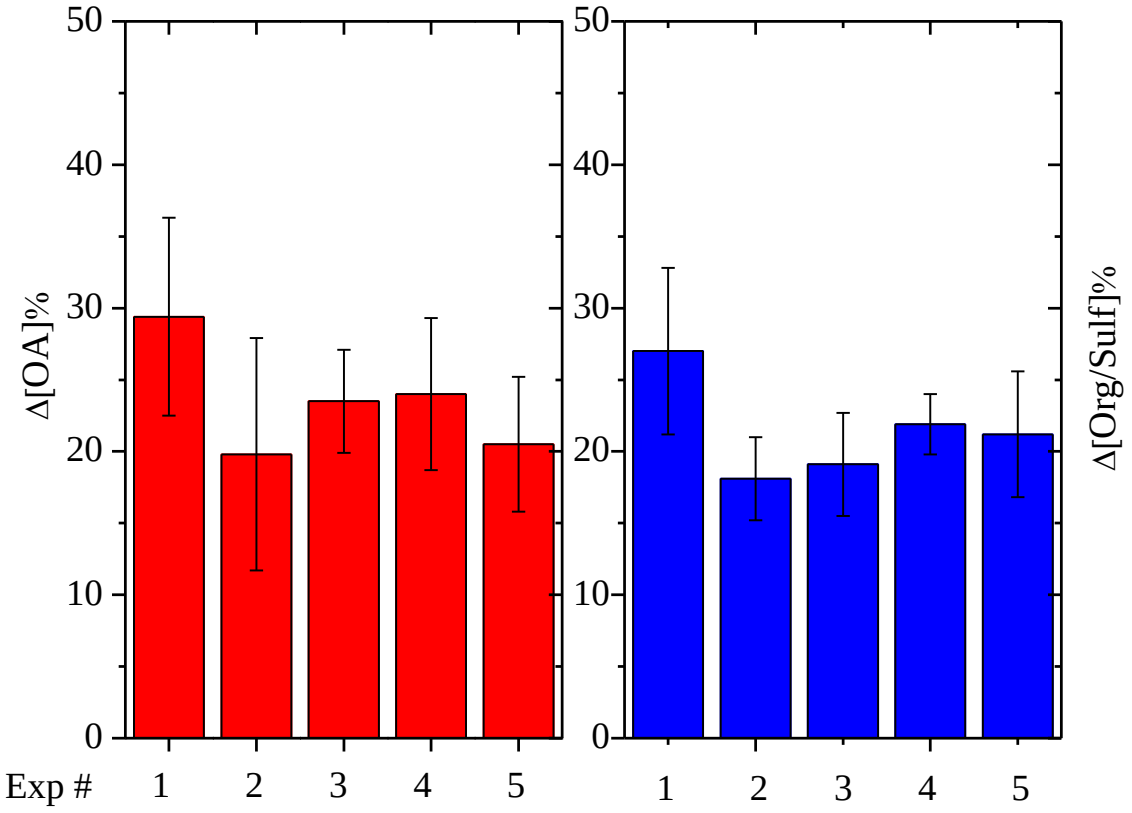

Figure 2.8: SMPS-derived percent change in the particle wall-loss corrected SOA (red columns) mass concentration after aging and AMS-derived percent change in organic to sulfate ratio (blue columns) after aging for all five experiments.

Exp. 5, performed at the intermediate RH of 50 %, resulted in a comparable change in SOA formation after aging as experiments at lower RH (Fig. 2.8). In this experiment, the increase in Org/Sulf after aging was 21.2 %, 1.5 % higher than the average Δ[Org/Sulf] of experiments 2-4. Δ[OA] for Exp. 5 was 20.5 %, about 2 % lower than the average Δ[OA] of experiments 2-4. The effect of RH on the SOA formation during chemical aging, at least for these conditions, appears to be small.

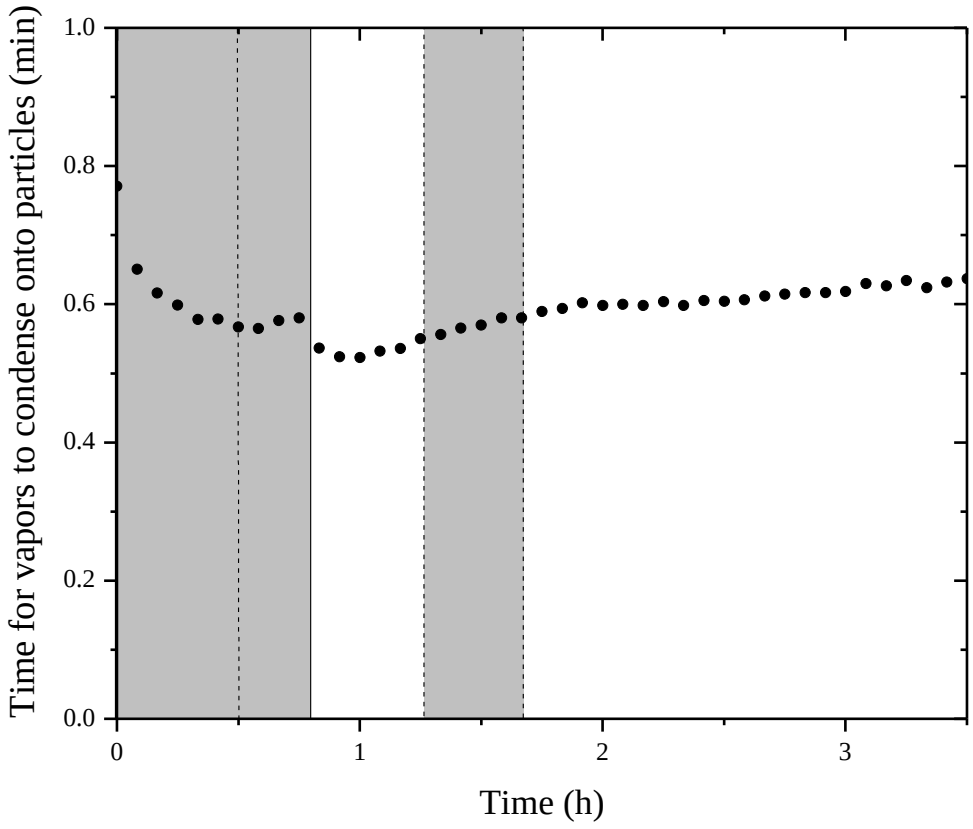

Figure 2.9: The calculated condensation sink (CS) in the form of time scale for vapors condensing onto particles (1/CS). Ozone was added into the chamber at time zero to initiate α-pinene ozonolysis. The shaded areas indicate that the chamber was dark. The dashed lines mark the beginning and the end of the two times HONO were added, respectively.

For chamber SOA experiments with preexisting particles, the particles act as competing surface against the chamber walls. We calculated the condensation sink (CS) of particles using the method described in Trump et al. (2014) with a unit accommodation coefficient, consistent with recent findings (Julin et al., 2014; Palm et al., 2016). The calculated condensation sink in the form of time scale for vapors condensing onto particles (1/CS) for Exp. 1 is shown in Fig. 2.9. During the entire experiment, the timescale for vapors to condense onto particles remained less than a minute. Compared to the organic vapor wall-loss timescale of 15 min in the CMU chamber (Ye et

al., 2016), the vapors condense onto the particles 15 times faster than that onto the walls. This corresponds to a 6.3 % loss of the semi-volatile vapors to the walls. Assuming the yields for the experiments conducted in this work also increase by 6.3 %, the absolute yields should be increased by 1-3 % after accounting for the vapor wall-loss effect. This approach is a conservative estimation of vapor wall loss, and yet the results are consistent with what we observed from the measurements. As indicated in Fig. 2.6, the organic to sulfate ratio stayed practically constant after its first peak at t=0.7 h until the introduction of OH. This is consistent with the fact that the semi-volatiles formed in our system only accounted for a small fraction of the products. Ye et al. (2016) studied the SVOCs formed in the α-pinene ozonolysis system and found 20 % SVOCs in the products formed from experiments with moderate precursor concentration (α-pinene=75 ppb). They also observed that the SVOC fraction increased with increased amounts of reacted α-pinene. Since the reacted α-pinene in our experiments was less than 35 ppb, our observation of small amount of SVOCs forming is also consistent with their results.

The situation is a little more complex for the second-generation oxidation because material with higher volatilities that could have become SOA were lost during the time after the end of the first phase and before the beginning of the second. To address this issue, OH radicals were introduced about an hour earlier in Exp. 1 as compared to the rest of the experiments. A shorter timescale ensures the first-generation vapor products react efficiently with OH instead of interacting with the chamber walls as in the case of longer timescales. There was an increase of 27 % in Org/Sulf in this experiment after aging, 7 % more than the average of the other four experiments. Δ[OA] for Exp. 1 was 29.4 %, about 7.5 % higher than the average of the rest four experiments. If we attribute this 7 % difference purely to the vapor wall-loss effect, then we estimate that vapor losses can increase the additional SOA formation by roughly another 10 % for

the experiments conducted in this work.

2.4.3 Effect of chemical aging on aerosol composition

Fig. 2.10 summarizes the absolute increase in O:C after the two doses of OH, respectively, with the corresponding exposure required to achieve the increase. As we discussed above using Exp. 1 as an example, the O:C in all experiments showed a stepwise increase after the first OH introduction while it grew continuously after the second OH introduction until the end of the experiment. For these five experiments, it took 10 - 30 min for the O:C to increase by 0.02-0.04. The stepwise increase in O:C is caused by the rapid reactions between the first generation vapor products and the OH. One of the major products identified in the gas phase from the α-pinene ozonolysis system, pinonaldehyde, reacts with OH at a rate of 4.4×10^{-11} cm^3 $molecule^{-1}$ s^{-1} (Atkinson and Arey, 2003). During the first hour of OH introduction, the OH concentration remains on average at a steady state of 2.4×10^7 molecule cm^{-3}. A quick estimation of $1/k_{OH}[OH]$ gives a timescale of 16 min, which is consistent with what we observed in these experiments.

The second exposure corresponds to the period until the end of each experiment. The increase in O:C of 0.01 to 0.04 during this stage clearly indicates change in SOA composition, however paired with minimum change in SOA mass. Although gas-phase reactions can contribute to these observed changes in O:C, the corresponding condensation of the products should also result in a detectable increase in SOA concentration during the same period. Given that changes in SOA concentration could not be detected the contribution of gas-phase oxidation was probably small. In addition, we observed small amounts of SVOCs forming in our system as discussed above. The significant change in O:C without corresponding increase in SOA mass concentration was

likely caused by heterogeneous reactions.

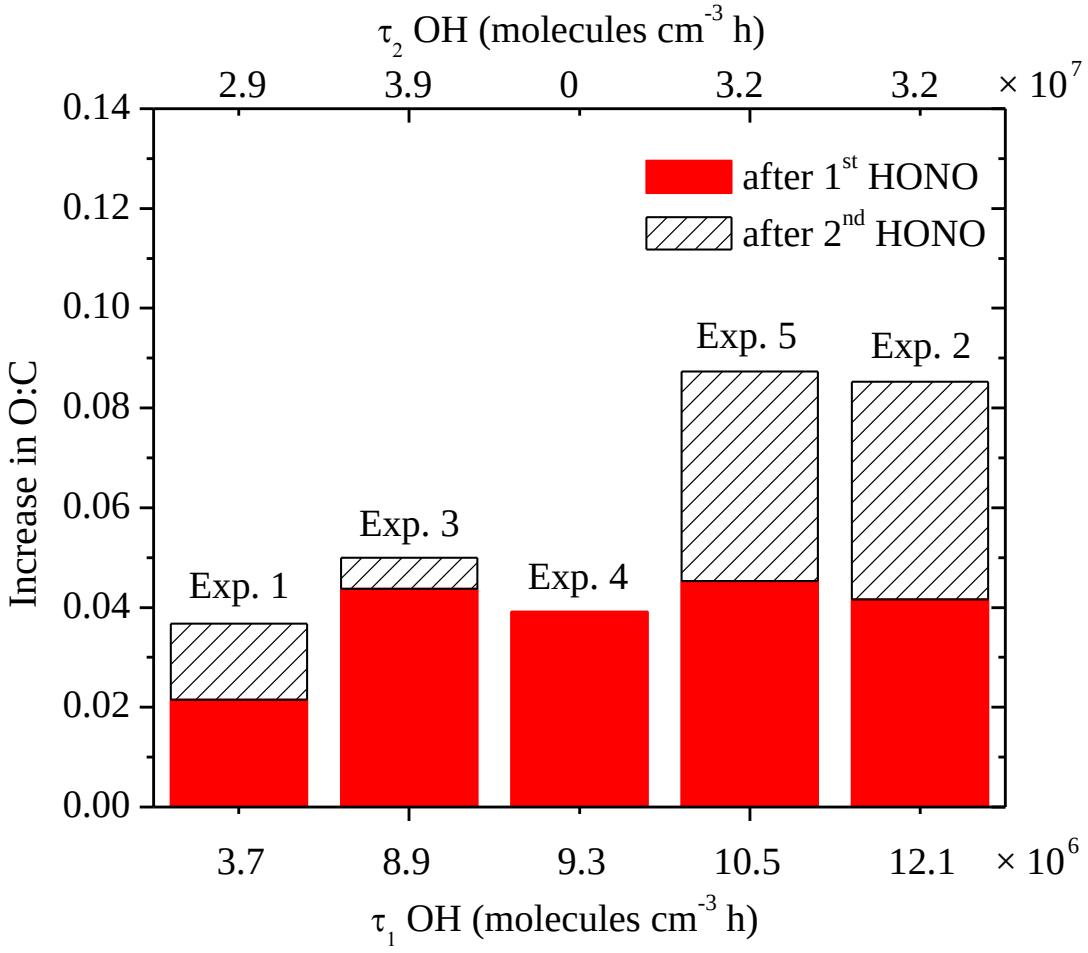

Figure 2.10: The absolute increase in O:C after the two doses of OH, respectively, with the corresponding exposure. The solid red columns are the increase in O:C after the first introduction of OH, with the corresponding exposure on the bottom axis. The hatched columns are the increase in O:C after the second introduction of OH, with the corresponding exposure on the top axis.

Based on the HR family analysis results, the less oxidized ion family CH decreased around 10 percent during the aging process (i.e., from 41.9 to 38.1 percent of the OA in Exp. 1 and from 40.5 to 35.3 percent in Exp. 2) while the more oxidized CHO_2 increased 4 percent in Exp. 1 (from 12.8 to 13.3 percent) and 16 percent in Exp. 2 (from 14.9 to 17.3 percent). The changes in the family CHO were +4 percent in Exp. 1 and -6 percent in Exp. 2, suggesting that there was both

production and destruction of the corresponding family members. The concentration of organonitrates was, as expected, close to zero initially in these experiments. At the end of the aging process, the NO family represented 3-3.5 % of the OA.

CO_2^+ (m/z 44) from family CHO_2 and $C_2H_3O^+$ (m/z 43) from family CHO are usually identified in aged and relatively fresh aerosols, respectively. Their fractions of the total organics, f_{44} and f_{43}, have been used as chemical indicators in chamber experiments (Donahue et al., 2012). During the dark ozonolysis period of Exp. 1 (Fig. B.2), the f_{43} increased initially and stayed practically constant after *t*=0.2 h, while f_{44} decreased. After the first introduction of OH, both f_{43} and f_{44} showed a stepwise increase. After the second introduction of OH, f_{43} decreased while f_{44} increased over time until the end of the experiment, indicating that the SOA was getting progressively more oxidized during aging. During Exp. 2 (Fig. B.4), f_{43} increased sharply initially and then slowly decreased during the dark ozonolysis period. This is consistent with the "ripening" effect observed during the MUCHACHAS campaign (Donahue et al., 2012). Overall, f_{43} decreased while f_{44} increased over the course of Exp. 2, indicating that the initially formed SOA was getting more oxidized during aging.

2.4.4 Comparison with other studies

Overall, the results from our chamber experiments in this work are consistent to those from the MUCHACHAS chambers. After adopting a size-dependent particle wall-loss correction method, we observed 20-30 % additional SOA formation after aging. Vapor wall-loss effect can account for an additional 10 %, increasing the range to 20-40 %. The O:C presented a stepwise increase of 0.02-0.04 after the first introduction of OH, and then increased gradually overtime after the second introduction of OH.

During the MUCHACHAS campaign, mixtures of SOA and gas-phase products formed in the Paul Scherrer Institute (PSI) 27 m^3 Teflon chamber from low (10 ppb) and high (40 ppb) initial α-pinene concentration were exposed to OH by TME ozonolysis and HONO photolysis at an RH of approximately 50 % (Tritscher et al. 2011). An OH concentration of 2×10^6 to 10×10^6 molecules cm^{-3} was maintained up to four hours. The authors reported an additional 50 % SOA mass forming after aging using the first-order, size-independent particle wall-loss correction for the suspended organic mass concentration measured by AMS. An increase of 0.04 in the oxygen to carbon ratio was also observed during aging.

In the 84.5 m^3 Aerosol Interaction and Dynamics in the Atmosphere (AIDA) aluminum chamber at Karlsruhe Institute of Technology, an OH concentration of 2×10^6 to 10×10^6 molecules cm^{-3} was used by a constant flow of TME (dark aging). The authors observed an increase of 17-55 % in the SMPS-derived SOA mass concentration (density corrected) after aging during four experiments with initial α-pinene concentration ranging from 14 to 56 ppb (Salo et al., 2011). In the 270 m^3 Simulation of Atmospheric Photochemistry in a large Reaction (SAPHIR) Teflon chamber at Forchungzentrum Jülich, SOA and vapors generated from the ozonolysis of 40 ppb α-pinene was aged for three consecutive days with OH produced by ambient light chemistry. An OH concentration of 2-5×10^6 molecules cm^{-3} was maintained and 9 %, 4 % and 1 % additional SOA was formed respectively after aging each day. These values were corrected for particle wall loss using different wall-loss rate constants determined during different periods of the experiment.

Our result of 20-40 % additional SOA formation due to aging is well within the range of that from the above chambers. The difference in the results from each chamber could potentially be attributed to different OH exposure (e.g. a constant flow of HONO or TME was provided in the PSI chamber). Other plausible explanations include whether the reported values were particle wall-

loss corrected and whether the same method was adopted for the correction.

For the HONO aging experiment performed in the CMU chamber during the MUCHACHAS campaign, Henry and Donahue (2012) suggested a potentially strong photolysis effect based on decreasing organic to sulfate ratio derived from the AMS measurements. In our experiments, the organic to sulfate ratio was affected by the size-dependent wall-loss process. Both the AMS-measured organic to sulfate ratio and the SMPS-measured OA remained relatively constant after correcting for the size dependence of the particle-wall process in these experiments. We thus conclude that minimum photolysis was observed for our experiments.

2.5 Conclusions

With an OH exposure equivalent to 2-4 days of typical atmospheric oxidation conditions, the OH aging of the α-pinene ozonolysis products formed 20-40 % additional SOA mass for the experimental conditions used in this work. Elevated RH up to 50 % has minimum effect on SOA production due to aging. We have constrained the aging effects on additional SOA formation quantitatively using both SMPS and AMS measurements.

A more oxygenated product distribution was observed after aging. A stepwise increase of 0.02-0.04 in O:C was observed within half an hour after the first introduction of OH. After the second-generation products were exposed to additional OH, the O:C grew continuously until the end of the experiments with an absolute increase of up to 0.04. During this period, minimum SOA production was observed. We attribute this phenomenon to condensed-phase reactions. Further investigation on a molecular scale is needed.

This work explored the additional SOA formation potential of the α-pinene ozonolysis products under high NO_x conditions. The aging time scale of this study of a few days corresponds

to the atmospheric lifetime of the corresponding aerosol. The additional formation of SOA observed here is clearly non-negligible, but is also much less than the doubling or tripling of the SOA that has been assumed in few modeling studies (Lane et al., 2008) which resulted in overprediction of the biogenic SOA. The present results can be used for the improvements of the currently used parameterizations for the aging of a-pinene SOA products in CTMs.

2.6 References

Atkinson, R., and Arey J.: Atmospheric degradation of volatile organic compounds, Chemical Reviews, 103, 4605-4638, 2003.

Barmet, P., Dommen, J., DeCarlo, P. F., Tritscher, T., Praplan, A. P., Platt, S. M., Prévôt A. S. H., Donahue, N. M., and Baltensperger, U.: OH clock determination by proton transfer reaction mass spectrometry at an environmental chamber, Atmos. Meas. Tech., 5, 647–656, 2012.

Canagaratna, M. R., Jimenez, J. L., Kroll, J. H., Chen, Q., Kessler, S. H., Massoli, P., Hildebrandt Ruiz, L., Fortner, E., Williams, L. R., Wilson, K. R., Surratt, J. D., Donahue, N. M., Jayne, J. T., and Worsnop, D. R.: Elemental ratio measurements of organic compounds using aerosol mass spectrometry: characterization, improved calibration, and implications, Atmos. Chem. Phys., 15, 253-272, 2015.

Chacon-Madrid, H. J., Henry, K. M., and Donahue, N. M.: Photo-oxidation of pinonaldehyde at low NO_x: from chemistry to organic aerosol formation, Atmos. Chem. Phys., 13, 3227-3236, 2013.

Cocker III, D. R., Flagan, R. C., and Seinfeld, J. H.: State-of-the-art chamber facility for studying atmospheric aerosol chemistry, Environ. Sci. Technol., 35, 2594–2601, 2001.

Crump, J. G., and Seinfeld, J. H.: Turbulent deposition and gravitational sedimentation of an aerosol in a vessel of arbitrary shape, J. Aerosol Sci., 2, 405–415, 1981.

Davidson, C. I., Phalen, R. F., and Solomon, P. A.: Airborne particulate matter and human health: a review, Aerosol Science and Technology, 39, 737–749, 2005.

Donahue, N. M., Henry, K. M., Mentel, T. F., Kiendler-Scharr, A., Spindler, C., Bohn, B., Brauers, T., Dorn, H. P., Fuchs, H., Tillmann, R., Wahner, A., Saathoff, H., Naumann, K.-H., Mohler, O., Leisner, T., Muller, L., Reinnig, M.-C., Hoffmann, T., Salo, K., Hallquist, M., Frosch, M., Bilde, M., Tritscher, T., Barmet, P., Praplan, A. P., DeCarlo, P. F., Dommen, J., Prevot, A. S. H., and Baltensperger, U.: Aging of biogenic secondary organic aerosol

via gas-phase OH radical reactions, Proc. Natl. Acad. Sci., U.S.A., 109, 13503 −13508, 2012.

Donahue, N. M., Robinson, A. L., Stanier, C. O., and Pandis, S. N.: Coupled partitioning, dilution and chemical aging of semivolatile organics, Environ. Sci. Technol., 40, 2635-2643, 2006.

George, I. J., Slowik J., and Abbatt J. P. D.: Chemical aging of ambient organic aerosol from heterogeneous reaction with hydroxyl radicals, Geophys. Res. Lett., 35, L13811, 2008.

Griffin, R. J., Cocker, D. R., Seinfeld, J. H., and Dabdub, D.: Estimate of global atmospheric organic aerosol from oxidation of biogenic hydrocarbons, Geophys. Res. Lett., 26, 2721–2724, 1999.

Henry, K. M., and Donahue, N. M.: Photochemical aging of α-pinene secondary organic aerosol: effects of OH radical sources and photolysis: J. Phys. Chem. A, 116, 5932−5940, 2012.

Henry, K. M., Lohaus T., and Donahue, N. M.: Organic aerosol yields from α-pinene oxidation: bridging the gap between first-generation yields and aging chemistry, Environ. Sci. Technol., 46, 12347−12354, 2012.

Intergovernmental Panel on Climate Change: Climate Change 2007: Synthesis Report. Contribution of Working Groups I, II and III to the Fourth Assessment Report of the Intergovernmental Panel on Climate Change, edited by R. K. Pachauri and A. Reisinger, eds., 104 pp., Cambridge Univ. Press, New York, 2007.

Julin, J., Winkler, P. M., Donahue, N. M., Wagner, P. E., and Riipinen, I.: Near-unity mass accommodation coefficient of organic molecules of varying structure, Environ. Sci. Technol., 48, 12083–12089, 2014.

Kalberer, M., Sax, M., and Samburova, V.: Molecular size evolution of oligomers in organic aerosols collected in urban atmospheres and generated in a smog chamber, Environ. Sci. Technol., 40, 5917−5922, 2006.

Keywood, M. D., Varutbangkul, V., Bahreini, R., Flagan, R. C., and Seinfeld, J. H.: Secondary organic aerosol formation from the ozonolysis of cycloalkenes and related compounds, Environ. Sci. Technol., 38, 4157–4164, 2004.

Krechmer, J. E., Pagonis, D., Ziemann, P. J., and Jimenez, J. L.: Quantification of gas-wall partitioning in Teflon environmental chambers using rapid bursts of low-volatility oxidized species generated in situ, Environ. Sci. Technol., 50, 5757–5765, 2016.

Kostenidou E., Pathak R. K., and Pandis S. N.: An algorithm for the calculation of secondary organic aerosol density combining AMS and SMPS data; Aerosol Science and Technology, 41, 1002–1010, 2007.

Kuwata, M., Zorn S. R., and Martin S. T.: Using elemental ratios to predict the density of organic material composed of carbon, hydrogen, and oxygen, Environ. Sci. Technol., 46, 787-794, 2012.

Lambe, A. T., Miracolo, M. A., Hennigan, C. J., Robinson, A. L., and Donahue, N. M.: Effective rate constants and uptake coefficients for the reactions of organic molecular markers (n-alkanes, hopanes and steranes) in motor oil and diesel primary organic aerosols with hydroxyl radicals, Environ. Sci. Technol., 43, 8794−8800, 2009.

Lane, T., Donahue, N. M., and Pandis, S. N.: Simulating secondary organic aerosol formation using the volatility basis-set approach in a chemical transport model, Atmospheric Environment, 42, 7439-7451, 2008.

Loza, C. L., Chhabra, P. S., Yee, L. D., Craven, J. S., Flagan, R. C., and Seinfeld, J. H.: Chemical aging of m-xylene secondary organic aerosol: laboratory chamber study, Atmos. Chem. Phys., 12, 151–167, 2012.

Matsunaga, A., and Ziemann, P. J.: Gas-wall partitioning of organic compounds in a Teflon film chamber and potential effects on reaction product and aerosol yield measurements, Aerosol Science and Technology, 44, 881–892, 2010.

McMurry, P. H., and Rader, D. J.: Aerosol wall losses in electrically charged chambers, Atmos. Chem. Phys., 4, 249–268, 1985.

Müller, L., Reinnig, M. C., Naumann, K. H., Saathoff, H., Mentel, T. F., Donahue, N. M., and Hoffmann, T.: Formation of 3-methyl-1,2,3-butanetricarboxylic acid via gas phase oxidation of pinonic acid - a mass spectrometric study of SOA aging, Atmos. Chem. Phys., 12, 1483–1496, 2012.

Nah, T., McVay, R. C., Zhang, X., Boyd, C. M., Seinfeld, J. H., and Ng, N. L.: Influence of seed aerosol surface area and oxidation rate on vapor wall deposition and SOA mass yields: a case study with α-pinene ozonolysis, Atmos. Chem. Phys., 16, 9361–9379, 2016.

Ng, N. L., Kroll, J. H., Chan, A. W. H., Chhabra, P. S., Flagan, R. C., and Seinfeld, J. H.: Secondary organic aerosol formation from m -xylene, toluene, and benzene, Atmos. Chem. Phys., 7, 3909–3922, 2007.

Palm, B. B., Campuzano-Jost, P., Ortega, A. M., Day, D. A., Kaser, L., Jud, W., Karl, T., Hansel, A., Hunter, J. F., Cross, E. S., Kroll, J. H., Peng, Z., Brune, W. H., and Jimenez, J. L.: In situ secondary organic aerosol formation from ambient pine forest air using an oxidation flow reactor, Atmos. Chem. Phys., 16, 2943–2970, 2016.

Paulson, S. E., Chung, M., Sen, A. D., and Orzechowska, G.: Measurement of OH radical formation from the reaction of ozone with several biogenic alkenes, J. Geophys. Res., 103, 25533-25539, 1998.Pope, C. A., Ezzati, M., and Dockery, D. W.: Fine-particulate air pollution and life expectancy in the United States, New Engl. J. Med., 360, 376-386, 2009.

Qi, L., Nakao, S., and Cocker, D. R.: Aging of secondary organic aerosol from α-pinene ozonolysis: Roles of hydroxyl and nitrate radicals, Journal of the Air & Waste Management Association, 62, 1359–1369, 2012.

Robinson, A. L., Donahue, N. M., Shrivastava, M. K., Weitkamp, E. A., Sage, A. M., Grieshop, A. P., Lane, T. E., Pierce, J. R., and Pandis, S. N.: Rethinking organic aerosol: semivolatile emissions and photochemical aging, Science, 315, 1259–1262, 2007.

Salo, K., Hallquist, M., Jonsson, Å. M., Saathoff, H., Naumann, K.-H., Spindler, C., Tillmann R., Fuchs, H., Bohn, B.; Rubach, F., Mentel, T. F., Müller, L., Reinnig, M., Hoffmann, T., and Donahue, N. M.: Volatility of secondary organic aerosol during OH radical induced ageing; Atmos. Chem. Phys., 11, 11055–11067, 2011.

Tritscher, T., Dommen, J., DeCarlo, P. F., Gysel, M., Barmet, P. B., Praplan, A. P., Weingartner E., Prévôt, A. S. H., Riipinen, I., Donahue, N. M., and Baltensperger, U.: Volatility and hygroscopicity of aging secondary organic aerosol in a smog chamber, Atmos. Chem. Phys., 11, 11477–11496, 2011.

Trump, E. R., Riipinen, I., and Donahue, N. M.; Interactions between atmospheric ultrafine particles and secondary organic aerosol mass: a model study, Boreal Environ. Res., 19, 352–362, 2014.

Tsimpidi, A. P., Karydis, V. A., Zavala, M., Lei, W., Bei, N., Molina, L., and Pandis, S. N.: Sources and production of organic aerosol in Mexico City: insights from the combination of a chemical transport model (PMCAMx-2008) and measurements during MILAGRO, Atmos. Chem. Phys., 11, 5153−5168, 2011.

Wang, N., Donahue, N. M., and Pandis, S.N.: Performance of different particle wall-loss correction methods for aging experiments of alpha-pinene SOA in a smog chamber, Aerosol Science and Technology; in preparation.

Ye, P., Ding, X., Hakala, J., Hofbauer, V., Robinson, E. S., and Donahue, N. M.: Vapor wall loss of semi-volatile organic compounds in a Teflon chamber, Aerosol Science and Technology, 50, 822-834, 2016.

Ye, P., Ding, X., Ye, Q., and Robinson, E. S.: Uptake of semivolatile secondary organic aerosol formed from α-pinene into nonvolatile polyethylene glycol probe particles, J. Phys. Chem. A, 120, 1459-1467, 2016.

Zhang, Q., Jimenez, J. L., Canagaratna, M. R., Allan, J. D., Coe, H., Ulbrich, I., Alfarra, M. R., Takami, A., Middlebrook, A. M., Sun, Y. L., Dzepina, K., Dunlea, E., Docherty, K., DeCarlo, P. F., Salcedo, D., Onasch, T., Jayne, J. T., Miyoshi, T., Shimono, A., Hatakeyama, S., Takegawa, N., Kondo, Y., Schneider, J., Drewnick, F., Borrmann, S., Weimer, S., Demerjian, K., Williams, P., Bower, K., Bahreini, R., Cottrell, L., Griffin, R. J., Rautiainen, J., Sun, J. Y., Zhang, Y. M., and Worsnop, D. R.: Ubiquity and dominance of oxygenated

species in organic aerosols in anthropogenically-influenced Northern Hemisphere midlatitudes, Geophys. Res. Lett., 34, L13801, 2007.

Zhang, X., Cappa, D. C., Jathar, S. H., McVay, R. C., Ensberg, J. J., Kleeman, M. J., and Seinfeld, J. H.: Influence of vapor wall loss in laboratory chambers on yields of secondary organic aerosol, Proc. Natl. Acad. Sci. U.S.A, 111, 5802-5807, 2014.

Chapter 3

Particle wall-loss correction methods in smog chamber experiments

3.1 Introduction

Smog chamber experiments have been an important tool for the study of atmospheric aerosol processes. One major challenge of smog chamber experiments is the particle wall-loss processes. The aerosols inside the chamber are lost to its walls due to Brownian diffusion, convection, electrostatic effects (especially for Teflon chambers) and gravitational sedimentation (Crump and Seinfeld, 1981). The particle wall-loss process is first-order and the particle wall-loss rate constant, *k*, is defined as,

$$\frac{\partial N(D_p,t)}{\partial t} = -k(D_p,t)N(D_p,t), \quad (1)$$

where $N(D_p,t)$ is the number concentration of particles with diameter D_p at time *t*. For an aerosol population, *k* is in general a function of particle size and time. Smaller-sized particles (less than 50 nm) have a higher loss rate due to diffusion-dominated wall-loss process while particles larger than one micron are lost mainly due to sedimentation. Electrostatic effect can play a major role for intermediate sizes (McMurry and Rader, 1985).

Early studies of chamber simulations of secondary organic aerosol (SOA) formation and growth assumed that the particle wall loss is negligible in fairly large chambers (~30 m^3) when determining SOA yields (Stern et al., 1987). Several particle wall-loss correction methods have since been developed and adopted in chamber studies. Pathak et al. (2007) proposed a semi-empirical wall-loss correction method that involves determining the first-order particle wall-loss rate constant, *k*, from the SMPS-measured SOA mass concentration after chemical reactions have been completed. This total mass concentration-based method is based on the assumption that *k* is independent of particle size for the size range of particles present in the experiment and remains constant during the course of an experiment. The constant *k* is found as the slope of the linear regression:

$$\ln[C_{SOA}^{sus}(t)] = -kt + Q, \quad (2)$$

where $C_{SOA}^{sus}(t)$ is the measured SOA mass concentration at time *t* and *Q* is an arbitrary constant. The values of $C_{SOA}^{sus}(t)$ used for the fit are taken after the SOA production has finished (condensation/evaporation is minimal). The corrected SOA concentration can be found by:

$$C_{SOA}^{tot} = C_{SOA}^{sus}(t) + k\int_0^t C_{SOA}^{sus}(t)dt - C_{seed}(0), \quad (3)$$

where $C_{seed}(0)$ is the seed mass concentration when SOA formation begins. This approach is relatively accurate when *k* remains more or less constant over the size range of the aerosol population inside the chamber, and accounts for the experiment-to-experiment variability of the particle wall-loss rates. However, it requires a period during which no reactions are taking place in the chamber and assumes that the rate constant does not vary during the experiment.

The size-dependent correction method involves determining a first-order *k* through the aforementioned linear fitting of the number concentration of the suspended particles, for each size, usually with the help of a scanning mobility particle sizer (SMPS). Several studies that adopted this method determined the $k(D_p)$ profile for the corresponding chamber through seed experiments where inert (e.g. ammonium sulfate) particles were used (McMurry and Grojean, 1985; Keywood et al., 2004; Ng et al., 2007; Nah et al., 2016; Fry et al., 2014). In these studies, an average $k(D_p)$ profile was applied to all experiments. This method takes care of the size dependence of *k* but not its potential variation from experiment to experiment. Ng et al. (2007) and Wang et al. (2017) determined a $k(D_p)$ profile using the initial seed wall-loss period for each of their experiments, thus accounting for the experiment-to-experiment variation.

The OA/Sulfate correction method was proposed by Hildebrandt et al. (2009) using the organic and the sulfate mass concentration measured by the aerosol mass spectrometer (AMS). This approach assumes that the loss rate constant of organic and sulfate are the same during an

experiment as there are no processes affecting sulfate other than losses to the walls. The corrected OA mass concentration is then calculated as,

$$C_{OA}(t) = \frac{C_{OA}^{sus}(t)}{C_{seed}(t)} C_{seed}(0) \quad (4)$$

where $C_{OA}^{sus}(t)/C_{seed}(t)$ is the AMS-derived organic to sulfate ratio and $C_{seed}(0)$ is the seed concentration in the chamber when SOA formation starts. Several chamber studies have adopted this method (Henry and Donahue, 2012; Loza et al., 2012). Other variations of this method including use the ratio of OA to other inert tracers like black carbon (BC) which are present in experiments investigating the evolution of primary OA from combustion sources (Hennigan et al., 2011). This method involving the use of OA to tracer ratio is accurate when the OA and the tracer have the same size distribution during the experiment or when the loss rate constant is close to size independent. However, in experiments in which SOA condenses more onto smaller-sized particles, the size dependence of the loss rate can introduce significant uncertainty in the corrected results (Wang et al., 2017).

An alternative method for particle wall-loss correction is the use of models of aerosol dynamics. Pierce et al. (2008) developed the Aerosol Parameter Estimation (APE) model that simulates the processes of condensation/evaporation, coagulation and particle wall loss during a chamber experiment. By constraining the unknown parameters with the SMPS-measured particle size distribution, the model can predict SOA formation for each experiment accounting for wall losses. The predicted particle wall-loss rates are both size- and time- dependent. The APE model predicts the particle wall-loss rates by assuming specific functional forms of its dependence on particle size (Crump and Seinfeld, 1981). The model has performed well in experiments in which the reaction time scale was short, but produced more uncertain results in experiments with slower reacting systems. Nah et al. (2017) adopted a modified version of the APE model that simulates

only coagulation and particle wall loss for the interpretation of inert seed wall loss experiments. The size-dependent, instantaneous particle loss rates were calculated directly from the SMPS-measured seed number size distribution at each time step. These instantaneous $k(D_p)$ values were then averaged over the initial seed loss period of the experiment and applied to the entire experiment including the SOA formation period. This approach focusing on specific wall-loss characterization experiments has the advantage that the functional dependence of the wall-loss rate constant is directly calculated from the measurements. Its disadvantage compared to APE is that it requires additional time for seed measurements and can no longer address the potential time dependence of k over the course of a complex experiment.

The aforementioned methods each has its own advantages and disadvantages, and may perform well for specific experiments and chambers. However, for long-lasting experiments such as SOA aging where particle size distribution may shift across a wide size range due to several generations of condensation, it is important to address both the time- and size-dependence of the particle loss rates for the purpose of SOA quantification. In this work, we adopt the modified APE model following Nah et al. (2017) and derived the size-dependent particle loss rate constants, $k(D_p)$, based on seed periods during the experiments. As an attempt to evaluate the time-dependence of the loss rates, we derive a second $k(D_p)$ at the end of each experiment with a second seed injection and loss characterization period. To probe the effect of electrostatic forces on particle wall loss, we regularly measured the $k(D_p)$ during the time period when the chamber was experiencing changes. We explore the coagulation effect on the estimated particle wall-loss rates and particle number/volume concentration in both a 12 m^3 Teflon chamber and a smaller 1.5 m^3 Teflon reactor. We evaluate the performance of the aforementioned particle wall-loss correction methods for relatively complex aging experiment of the α-pinene ozonolysis products.

3.2 Experimental approach

3.2.1 Particle wall-loss rate constant measurements in the 12 m^3 CMU Teflon chamber

The CMU smog chamber is a 12 m^3 Teflon reactor (Welch Fluorocarbons) suspended in a temperature-controlled room. The walls of the room are covered with UV lights (GE10526 and 10244). Prior to each experiment, the chamber is flushed overnight with purified air under UV illumination to remove any residual particles and vapors. Purified air is generated by passing house air through a high-efficiency particulate air (HEPA) filter to remove particles, a Purafil filter to remove NO_x and an activated carbon filter to remove any organics followed by a silica gel filter, keeping relative humidity (RH) below 20% throughout the experiments performed in this work.

To characterize the particle wall-loss rates, we performed experiments with ammonium sulfate (AS) particles during a full year. We used both 1 g L^{-1} and 5 g L^{-1} ammonium sulfate solutions to generate particles, with the latter producing more particles at larger sizes. The ammonium sulfate solution was fed to an atomizer (TSI, model 3076) at a constant rate of 90 mL h^{-1} to produce droplets. The droplets passed through a diffusion dryer and a neutralizer to produce dry ammonium sulfate particles. This process produced seeds with a number mode size of around 100 nm. The initial seed number concentration in the chamber was around 3×10^4 cm^{-3}, corresponding to a mass concentration of around 70 μg m^{-3} and a surface area concentration of around 1500 μm^2 cm^{-3}. After injecting the particles, the particle wall loss was quantified for 3-4 hours. We measured the particle size distribution with a TSI Scanning Mobility Particle Sizer, SMPS (classifier model 3080; DMA model 3081; CPC model 3010 or 3772).

For a number of α-pinene ozonolysis experiments, we characterized the particle wall-loss rates twice, once before and once after the main experiment. At the beginning of each aging experiment, we used the 1 g L^{-1} ammonium sulfate solution to generate seed particles to provide

enough surface area for the vapors to condense on. From the 3-4 h wall-loss time period, we were able to characterize the initial $k(D_p)$ profile for this experiment. At the end of each experiment, we injected additional ammonium sulfate seeds into the chamber using the same method with a more concentrated solution (5 g L^{-1}) in order to characterize the particle wall-loss rate constants a second time. Details about the experimental procedure for these aging experiments can be found in Wang et al. (2017).

Table 3.1: List of experiments and experimental conditions

Exp.	**Chamber volume** (m^3)	**Type**	**Number of seed wall-loss periods**	**Initial seed volume/number/surface concentration[a]**			**Notes**
				(μm^3 cm^{-3})	(cm^{-3})	(μm^2 cm^{-3})	
1	1.5	Seed	1	1892	13.0×10^4	19500	Regular seed wall-loss exp.
2	12	Seed	1	53	3.1×10^4	1630	Regular seed wall-loss exp.
3	12	Seed+SOA	2	39	1.8×10^4	1076	Aging exp. of α-pinene ozonolysis
4	12	Seed+SOA	2	42	2.8×10^4	1388	Aging exp. of α-pinene ozonolysis
5	12	Seed	2	75	2.3×10^4	1874	UV lights on for 3 h before final seed
6	12	Seed	2	200	5.2×10^4	4599	HONO addition (5 L min^{-1} for 20 min) before final seed
7	12	Seed	1	40	2.6×10^4	1271	Regular seed wall-loss exp. with overnight flushing after
8	12	Seed	1	40	3.4×10^4	1329	Regular seed wall-loss experiment ran on the day after Exp. 7

[a]Maximum concentration after initial seed injection (before wall loss of these seed particles).

3.2.2 Particle wall-loss rate constant measurements in a 1.5 m^3 Teflon reactor

We performed additional particle wall-loss measurements in a dual smog chamber system consisting of a set of two identical Teflon chambers (1.5 m^3 each). The two pillow-shaped chambers are mounted on metal frames with wheels on the bottom for portability. Details about the portable dual-chamber system can be found in Kaltsonoudis et al. (2017). The system was tested inside the laboratory in the present study. We used both ammonium sulfate and PSL particles (700 nm, Duke Scientific Corporation) for measurements in these chambers.

A list of experiments performed in this work is presented in Table 3.1, together with the experimental conditions. For the regular seed experiments to test particle loss rate constants, only one for either chamber is listed.

3.3 Data analysis

3.3.1 Particle loss rate constants

The particle loss rate constants derived from methods accounting for the coagulation of particles are denoted as k_c in the rest of the paper, while the apparent particle loss rate constants neglecting the role of coagulation as k_a.

The coagulation-corrected particle wall-loss rate constants were derived based on the model used by Nah et al. (2016). The model assumes that only two processes take place: particle wall loss and coagulation. With a given particle number size distribution at a specific time step, the model predicts how the distribution evolves at the next step assuming coagulation is the only process based on the coagulation rates in Seinfeld and Pandis (2006). The model attributes the difference between the predicted size distribution and the measured one to particle wall loss. Then the model calculates the instantaneous wall-loss rate constants at each time step for each size. To

obtain the coagulation-corrected particle wall-loss rate constant, $k_c(D_p)$, the instantaneous rate constants are averaged over time. The reported uncertainty is calculated $as\ \sigma_{k_c}/\sqrt{N-1}$ where σ_{k_c} is the standard deviation of k_c for a certain size bin and N is the total number of time steps used. To minimize the uncertainty of k_c, we used a time step of 15 min for the averaging of the measurements. Only SMPS measurements from the seed wall-loss periods were used as the inputs for the model.

The apparent particle loss rate constants, denoted as k_a in this work, were derived from the size-dependent loss rate constant. Details can be found in Wang et al. (2017). This approach uses the SMPS-measured seed particle number size distribution as input, and calculates a first-order loss rate constant for particles of a certain size across all measured sizes. These k_a's intrinsically represent the combined loss effect of both particle wall loss and coagulation.

For particles in size bin i, $k_{a,i}$ is found by:

$$\ln[\mathrm{N}_i^{sus}(t)] = -k_{a,i}t + Q \tag{5}$$

where $\mathrm{N}_i^{sus}(t)$ is the suspended aerosol number concentration at size bin i measured by SMPS and Q is an arbitrary constant.

3.3.2 Size-dependent particle loss correction

Both k_c and k_a are size-dependent. The corrected particle number concentration at size bin i, $\mathrm{N}_i^{tot}(t)$, is calculated by,

$$\mathrm{N}_i^{tot}(t) = \mathrm{N}_i^{sus}(t) + k_{a/c,i}\int_0^t \mathrm{N}_i^{sus}(t)dt. \tag{6}$$

We can then derive the corrected particle volume concentration of size bin i, $\mathrm{V}_i^{tot}(t)$.

The organic aerosol mass concentration corrected for wall losses can be then calculated during a seeded experiment using:

$$C_{SOA}^{tot}(t) = (V^{tot}(t) - V_s)\rho_{SOA}, \quad (7)$$

where $V^{tot}(t)$ is the corrected total particle volume concentration summed across all sizes and V_s is the corrected seed volume concentration.

3.4 Results and discussion

3.4.1 Role of coagulation in particle wall-loss processes

Fig. 3.1 shows the apparent (k_a) and coagulation-corrected (k_c) particle wall-loss rate constants as a function of particle size for the 1.5 m^3 Teflon reactor (Exp. 1) and the 12 m^3 chamber (Exp. 2) after both systems have remained undisturbed in the lab for weeks. According to the aerosol dynamics model, coagulation was a significant loss process in Exp. 1 for particles with diameters smaller than 250 nm and for particles smaller than 150 nm in Exp. 2. In Exp. 1, the apparent loss rate constant for 100 nm particles was 0.5 h^{-1}, while the actual rate constant after correcting for coagulation was only 0.2 h^{-1}. For 200 nm particles, the corresponding values were 0.3 h^{-1} and 0.2 h^{-1} respectively. The coagulation effects were minor for particles larger than 250 nm in both cases. Once corrected for coagulation, the particle wall-loss rate constants indicated little size dependence for particles larger than 100 nm in both experiments. The corresponding values were 0.25 h^{-1} for the small reactor, and 0.1 h^{-1} for the 12 m^3 chamber. The uncertainty of the aerosol dynamics model for the larger particles is significantly higher than that of the direct calculation based on Eqn. 5. This is due to the reliance of the model on observed small changes of small number concentrations versus the linear regression that uses measured values. We suggest using twice the uncertainty of the linear regression as representative of the uncertainty of the rate loss constants of particles larger than 300 nm given the small impact of coagulation on particle concentrations and sizes in this range.

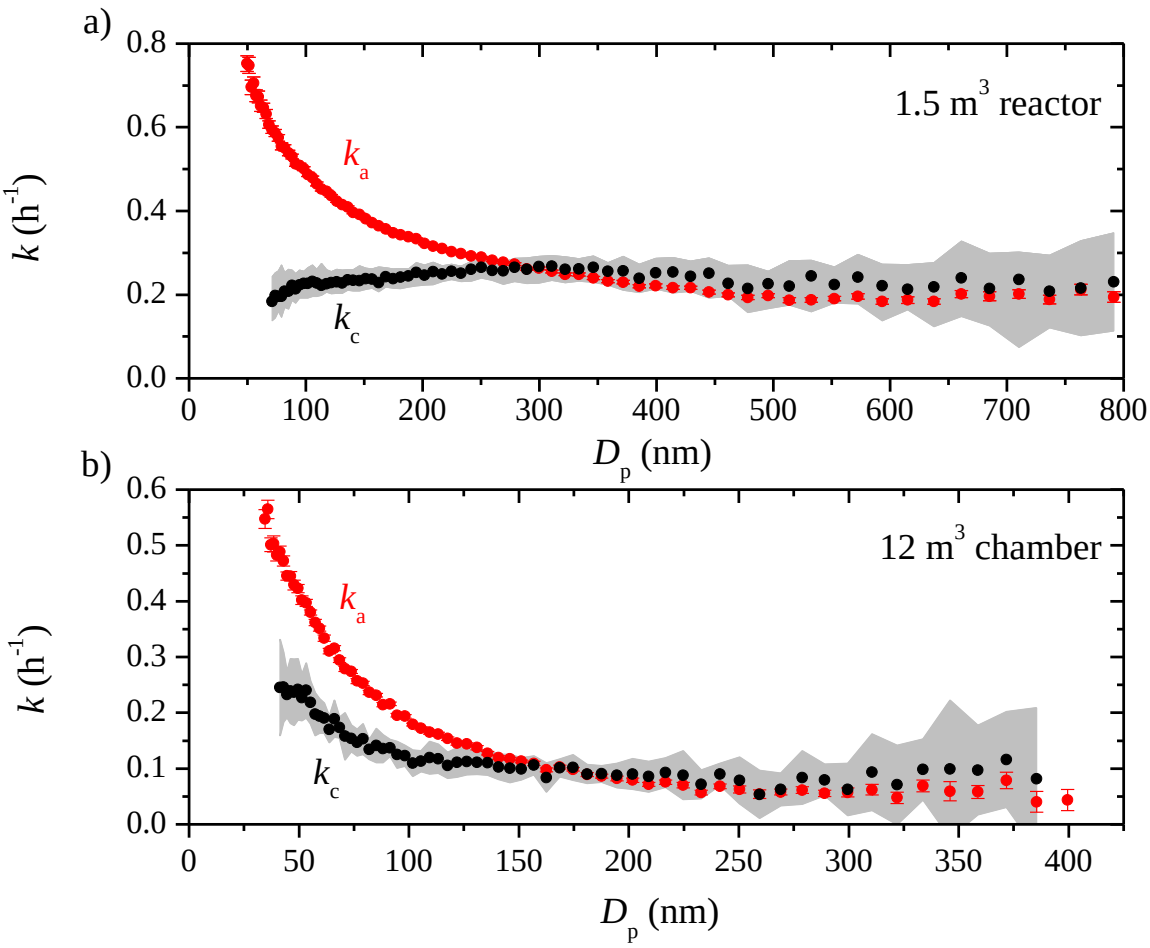

Figure 3.1: The apparent (red symbols) and coagulation-corrected (black symbols) particle wall-loss rate constants as a function of particle size for **a)** the 1.5 m^3 Teflon reactor and **b)** the 12 m^3 CMU smog chamber after the two systems have been left undisturbed in the lab for weeks. The particle loss rate constants were derived based on SMPS measurements from Exp. 1 and Exp. 2. Only k_a's with an $R^2 > 0.5$ are shown. The error bars correspond to one standard deviation. The grey area is the uncertainty associated with k_c.

To evaluate the coagulation effect on particle number and volume concentrations, we corrected them for wall loss with both $k_a(D_p)$ and $k_c(D_p)$. The results for the 1.5 m^3 reactor (Exp. 1) are shown in Fig. 3.2 as an example. Coagulation caused the particle number concentration to decrease by 27 % over a 5 h period in this case, but had, as expected, negligible effect on particle volume concentration. Please note that even if the overall effect of coagulation on total particle number is moderate, it is mostly concentrated in the lower end of the size distribution. As a result,

the coagulation effect is almost an order of magnitude higher than average for the rate constants of particles smaller than 100 nm. In this case there is little difference in the calculated total volume concentration, which is the most important quantity for SOA studies. However, this difference depends in general on the particle size distribution. If a significant part of the volume (or mass) is in particles with diameters less than 200 nm or so, the effect of coagulation will be significant for the corrected particle volume too.

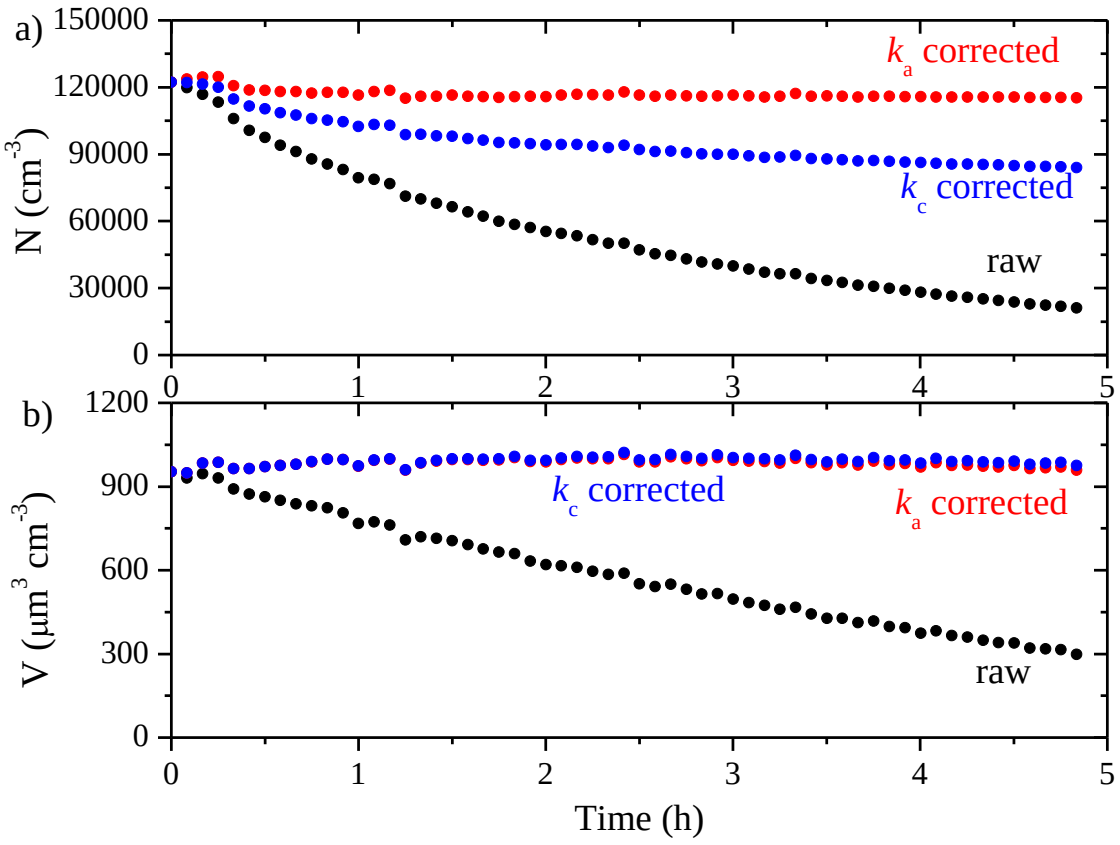

Figure 3.2: The SMPS-measured (black symbols) and the particle loss corrected **a)** number and **b)** volume concentration using the $k_a(D_p)$ profile (red symbols) and the $k_c(D_p)$ profile (blue symbols) for Exp. 1.

3.4.2 Particle wall-loss rate constants in the CMU chamber over three years

Fig. 3.3 shows the coagulation corrected $k_c(D_p)$ profiles together with their corresponding uncertainties in the 12 m^3 CMU smog chamber over a span of three years. All these measurements

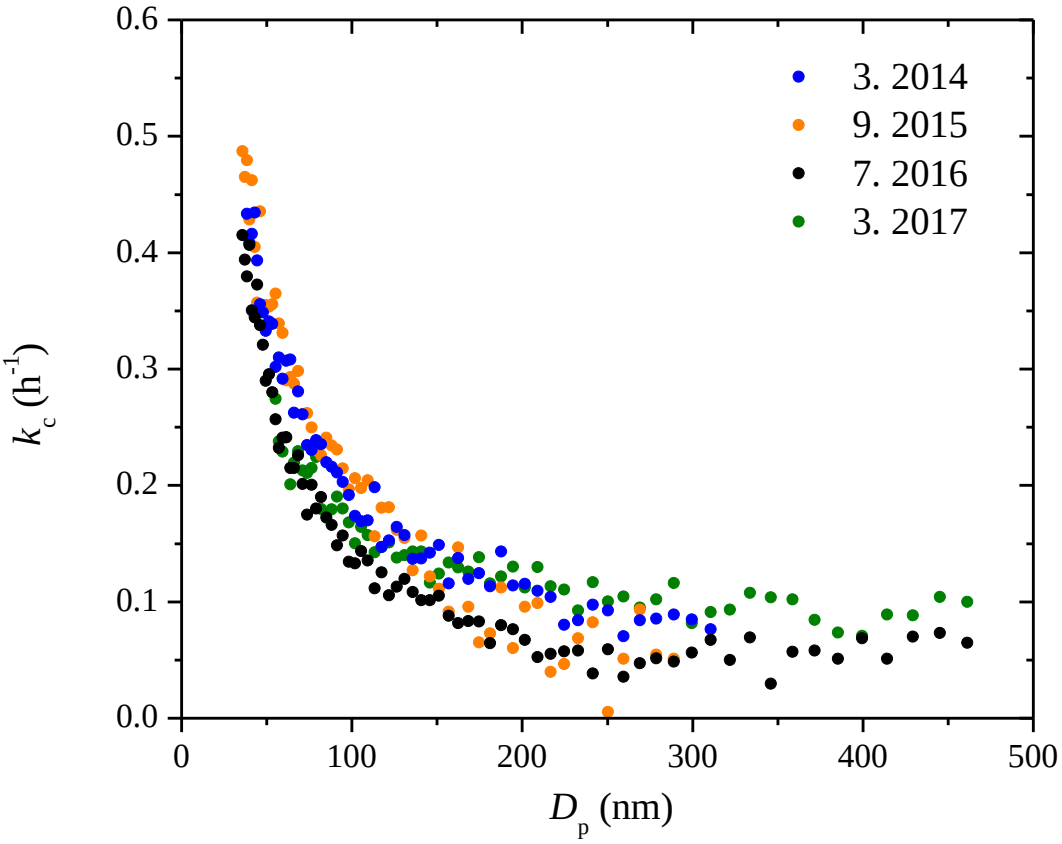

Figure 3.3: The $k_c(D_p)$ profiles for the 12 m^3 CMU Teflon chamber over a span of three years. The particle wall-loss rate constants were derived based on SMPS measurements from experiments with only ammonium sulfate particles.

were performed during periods in which the chamber was undisturbed. The rate constants show a monotonic decreasing trend with sharp decrease initially until 100 nm due to diffusion dominating the wall-loss processes. Then the loss rate constants gradually decrease until 300 nm, after which they stay almost constant until the end of the measured size range. Using the $k_c(D_p)$ determined in

2017 as an example, k_c decreased from 0.3 h^{-1} at 50 nm, to 0.14 h^{-1} at 100 nm, then gradually to 0.05 h^{-1} at 300 nm and stayed constant until approximately 500 nm. The $k_c(D_p)$ profiles over the past three years stayed fairly consistent with values equal 0.32±0.03 h^{-1} at 50 nm, 0.16±0.03 h^{-1} at 100 nm, 0.10±0.02 h^{-1} at 200 nm and 0.07±0.01 h^{-1} at 300 nm. The behavior of the chamber after disturbances (e.g., repairs, upgrades, etc.) will be discussed in a subsequent section.

3.4.3 Applying different particle wall-loss correction methods to SOA aging experiments

The measured particle volume concentration time series of a typical aging experiment (Exp. 3) of α-pinene ozonolysis products in the 12 m^3 CMU Teflon chamber is shown in Fig. 3.4. In this experiment there were three separate stages. We injected ammonium sulfate seeds both at the beginning of the experiment and at the end (t=3.5 h). At t=0, ozone was introduced into the chamber to react with α-pinene producing SOA in the dark. HONO was bubbled into the chamber twice at t=0.5 h and 1.2 h to produce OH radicals under UV illumination, leading to a second round of reactions in the system. The size-dependent $k_a(D_p)$ and $k_c(D_p)$ derived from the initial 4.5 h seed loss period differed by up to 0.2 h^{-1} for particles smaller than 100 nm and were practically the same for particles larger than 100 nm (Fig. 3.4c). The size-independent loss rate constants k_1-k_3 were derived during the three periods when condensation/evaporation was minimal. $k_1 = 0.05\ h^{-1}$ ($R^2 = 1$) was derived from volume concentration measurements from t=-4.5 to 0 h according to Eq. 2, $k_2 = 0.04\ h^{-1}$ ($R^2 = 0.8$) from t=2 to 3.4 h and $k_3 = 0.03\ h^{-1}$ ($R^2 = 0.9$) from t=4.7 to 8.4 h. One major contributor to the difference in these three k's is the size dependence of the particle wall-loss rate constants. k_2 was calculated from the period after several generations of condensation. The particle size distribution shifted to bigger size range (Fig. 3.4b) and thus

resulted in a smaller value compared to k_1. k_3 was derived from the final seed loss period where the majority of the seed particles were distributed at larger sizes.

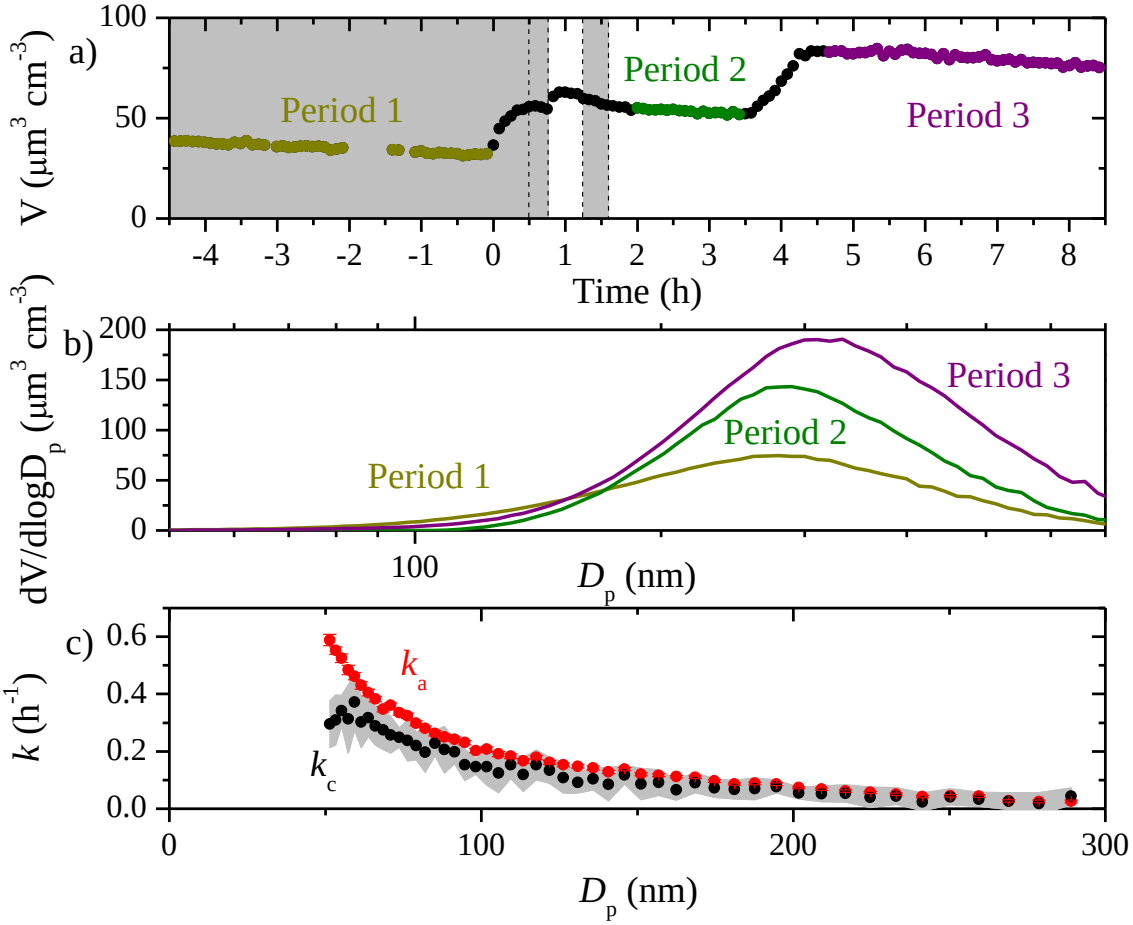

Figure 3.4: a) The SMPS-measured particle volume concentration time series for an aging experiment (Exp. 3) with 3 colored periods used to derive the corresponding size-independent particle wall-loss rate constants, k_1-k_3 (Eq. 2). The grey area indicates that the chamber was dark. The dashed lines mark the beginning and the end of bubbling HONO into the chamber twice; **b)** the averaged particle volume size distribution over the 3 periods used to develop k_1-k_3 based on the SMPS measurement for Exp. 3; **c)** the size-dependent particle wall-loss rate constants determined from SMPS-measured particle number concentration for Exp. 3. Only k_a's (red symbols) with an $R^2 > 0.5$ are shown. The error bars are one standard deviation. The grey area is the uncertainty associated with k_c (black symbols).

The particle wall-loss corrected SOA mass concentration ($\rho = 1.4$ μg m^{-3}) time series using both the size-independent k_1-k_3 and the size-dependent $k_a(D_p)$ and $k_c(D_p)$ for Exp. 3 are shown in

Fig. 3.5.

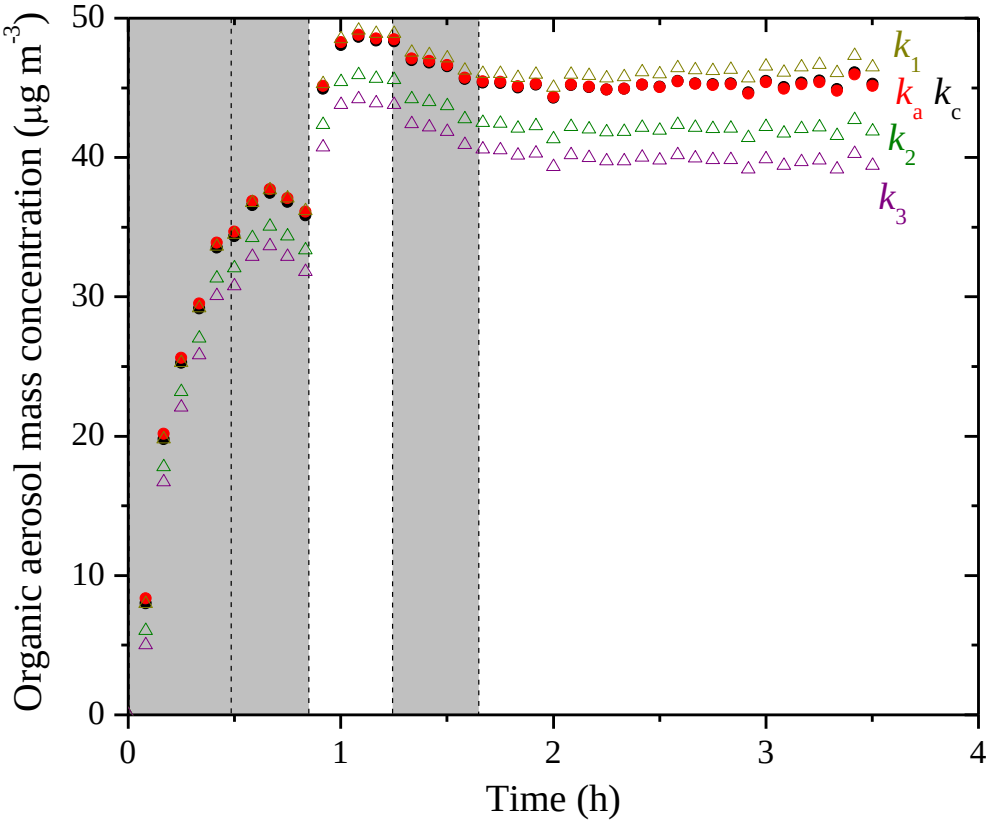

Figure 3.5: Particle loss corrected SOA mass concentration (ρ_{SOA} = 1.4 µg m^{-3}) time series using the size-independent k's (open symbols) and the size-dependent $k(D_p)$'s (solid symbols) for Exp. 3. $k_1 - k_3$ were derived from the total mass concentration-based method (Eq. 2) when wall loss was the only process (t_1= -4.5-0 h; t_2= 2-3.4 h; t_3= 4.7-8.4 h). The $k_a(D_p)$ and the $k_c(D_p)$ profiles were derived from the two models based on the SMPS-measured number concentration of the seed wall-loss periods. The shaded area indicates that the chamber was dark. The dashed lines mark the beginning and the end of bubbling HONO into the chamber.

Applying k_1-k_3 to Eq. 3 resulted in corrected SOA mass concentration differing up to 7 µg m^{-3}. To estimate the $k(D_p)$'s at D_p<50 nm and D_p> 300 nm, we used a linear fit of the $k(D_p)$'s from 50 to 70 nm to back extrapolate the k's at smaller sizes and assumed a constant k value equal to that at 300 nm for particles larger than 300 nm (Fig. C2). We corrected for total particle number

concentration applying the size-dependent loss rates to Eq. 6, and then calculated the corrected SOA mass concentration using Eq. 7. The $k_a(D_p)$- and the $k_c(D_p)$- corrected SOA mass concentration time series were practically the same for this experiment, because the majority of the formed SOA mass condensed on particles with diameters exceeding 100 nm.

3.4.4 Effect of size-dependent wall loss on organic to sulfate ratio

Fig. 3.6 shows the AMS-measured organic to sulfate ratio (OA/Sulfate) for Exp. 3. In the beginning, the ratio increased to 1.2 at t=0.6 h due to the first generation of SOA formation. It then stayed practically constant until OH was introduced into the chamber at t=0.9 h. The second-generation of SOA formation led to an increase of the ratio to 1.6 at t=1.1 h. The ratio decreased gradually to 1.5 until the second introduction of HONO. This decrease could be explained as a loss of SOA due to photodegradation or another chemical process. Another explanation for the decreasing trend of OA/Sulfate ratio during this period is the size dependence of the particle wall-loss rates. Particles of smaller sizes with higher organic to sulfate ratios can be lost to the walls at a faster rate, thus causing the OA/Sulfate to decrease during periods when wall loss is the dominant process in the chamber. The strong size dependence of the OA/Sulfate ratio in this experiment is indicated in Fig. 3.7. The organic mass distribution peaked at an aerodynamic vacuum diameter (D_{va}) equal to around 300 nm, while the sulfate one at 450 nm. This indicates the majority of the organic vapors condensed onto smaller particles with a higher surface to volume ratio. Fig. 3.7b shows the OA/Sulfate derived from the AMS-measured mass distribution (averaged from t=1.1 to 3.5 h) as a function of the particle vacuum aerodynamic diameter. For particles with D_{va} from 200 to 300 nm, the ratio dropped dramatically from 10 to 3. It then decreased gradually and stabilized at 1 from D_{va}=300 to 1000 nm.

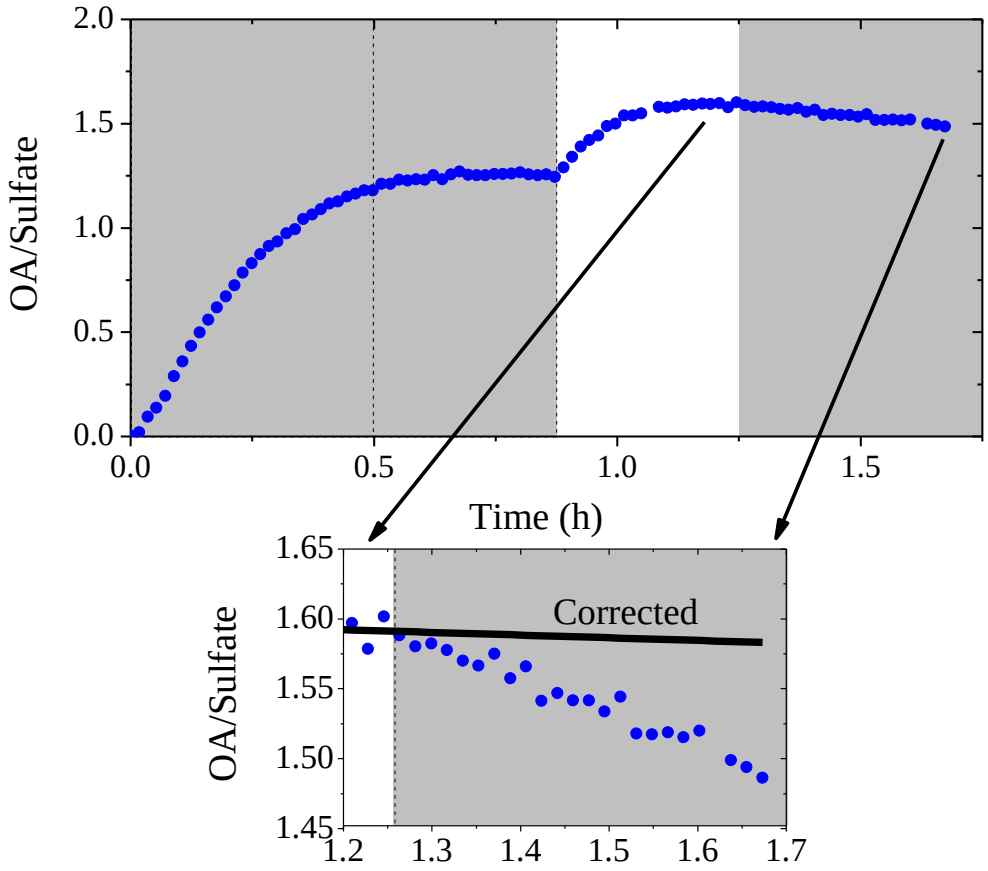

Figure 3.6: The organic to sulfate ratio time series derived from AMS measurements for Exp. 3 (data after the second HONO introduction is not shown). The inset is a blow-up of the OA/Sulfate from its maximum until the second HONO introduction. The black symbols are the size dependence corrected OA/Sulfate during that half hour. The shaded area indicates that the chamber was dark. The dashed lines mark the beginning and the end of the first HONO injection into the chamber.

To further analyze the effect of size-dependent wall loss on the OA/Sulfate ratio, we adopted the method suggested in Wang et al. (2017). This approach allows the estimation of mass-weighted wall-loss rate constants for both species, $\bar{k}_{SO_4}$ and $\bar{k}_{OA}$, by discretizing the AMS-measured mass distribution in the diameter space and assigning the corresponding $k_c(D_p)$. For periods during the experiment when particle wall-loss is the only process, the loss-corrected

OA/Sulfate can be estimated using $(\mathrm{OA/Sulfate})_m(t)\exp\left(\bar{k}_{SO_4} - \bar{k}_{OA}\right)t$, where $(\mathrm{OA/Sulfate})_m(t)$ is the measured OA/Sulfate. For Exp. 3 in this work, we discretized the AMS-

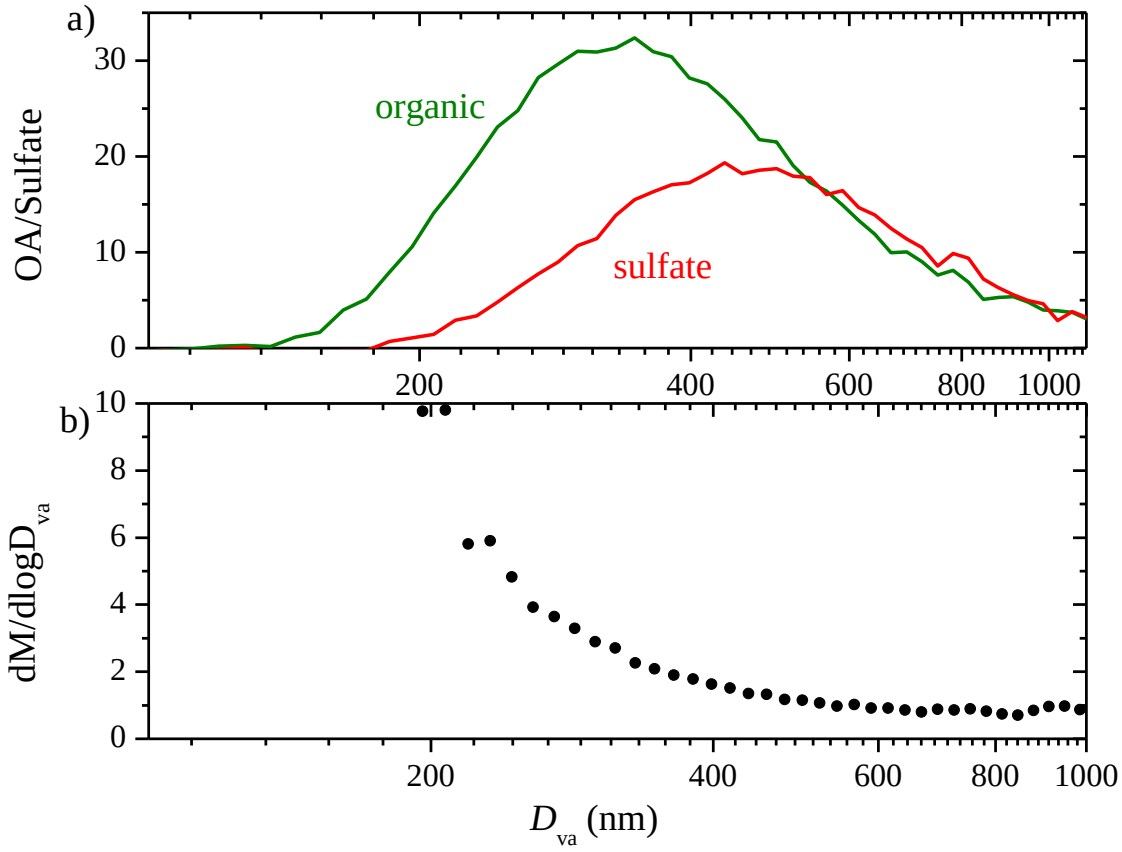

Figure 3.7: a) The AMS-measured organic (green) and sulfate (red) mass distribution for Exp. 3; **b)** the dependence of the AMS-derived organic to sulfate ratio on particle vacuum aerodynamic diameter. The results are based on particle time-of-flight (PToF) data averaged over ~2.5 h (t=1.1-3.5 h).

measured mass distribution (averaged from *t*=1.2 to 1.7 h) into 10 diameter bins and found $\bar{k}_{Org} = 0.06\ h^{-1}$ and $\bar{k}_{SO_4} = 0.05\ h^{-1}$. The particle wall-loss corrected OA/Sulfate for the chosen time period is shown in the inset of Fig. 3.6. The loss-corrected ratio remained relatively constant, indicating that the decrease observed in the measured OA/Sulfate was caused by the size-

dependent particle wall-loss process coupled with the different size distributions of the organics and sulfate.

3.4.5 Time dependence of particle wall-loss rates during an experiment

When the CMU chamber is undisturbed the wall loss rate constant is around 0.1 h^{-1} for particles larger than 100 nm. However, after small repairs (addition of a sampling line, replacement of lights, etc.) the loss rates can increase dramatically and the effects can last for weeks. During these periods the size-dependent, coagulation-corrected particle wall-loss rate constants, $k_c(D_p)$, can change significantly during the course of an experiment. The results of such an experiment in a "disturbed" smog chamber are described below.

The comparison of the two $k_c(D_p)$ profiles derived from the initial and the final seed periods for Exp. 4 are shown in Fig. 3.8, together with the raw and the corrected aerosol volume concentration time series. This is a similar aging experiment of α-pinene ozonolysis products as Exp. 3, but with only one HONO injection. Before t=0, ammonium sulfate seed particles were losing to chamber walls. At t=0, ozone was added into the chamber to react with α-pinene. The aerosol volume increased due to condensation of the first-generation products. At t=2.5h, HONO was introduced into the chamber and OH were produced at t=3 h under UV illumination. The aerosol volume increased again due to additional SOA formation from the second-generation oxidation. At t=4 h, we injected ammonium sulfate particles into the chamber to characterize the particle wall loss rates for a second time. The final k_c's were statistically higher than their initial counterparts at every size, and both sets of k_c's were higher than their usual values in the chamber (Fig. 3.3). Comparing the initial k_c's with the averaged usual values under undisturbed chamber conditions, the initial k_c was 0.33 h^{-1} as compared to the usual 0.16 h^{-1} at 100 nm, 0.21 h^{-1} compared

to 0.10 h^{-1} at 200 nm, and 0.15 h^{-1} compared to 0.07 h^{-1} at 300 nm. The final $k_c(D_p)$-corrected volume concentration was higher than the one corrected using the initial $k_c(D_p)$ by 37 % at t=4 h. The time dependence of $k_c(D_p)$ during the course of this experiment introduced a 40% or so uncertainty in the corrected aerosol mass or volume concentration.

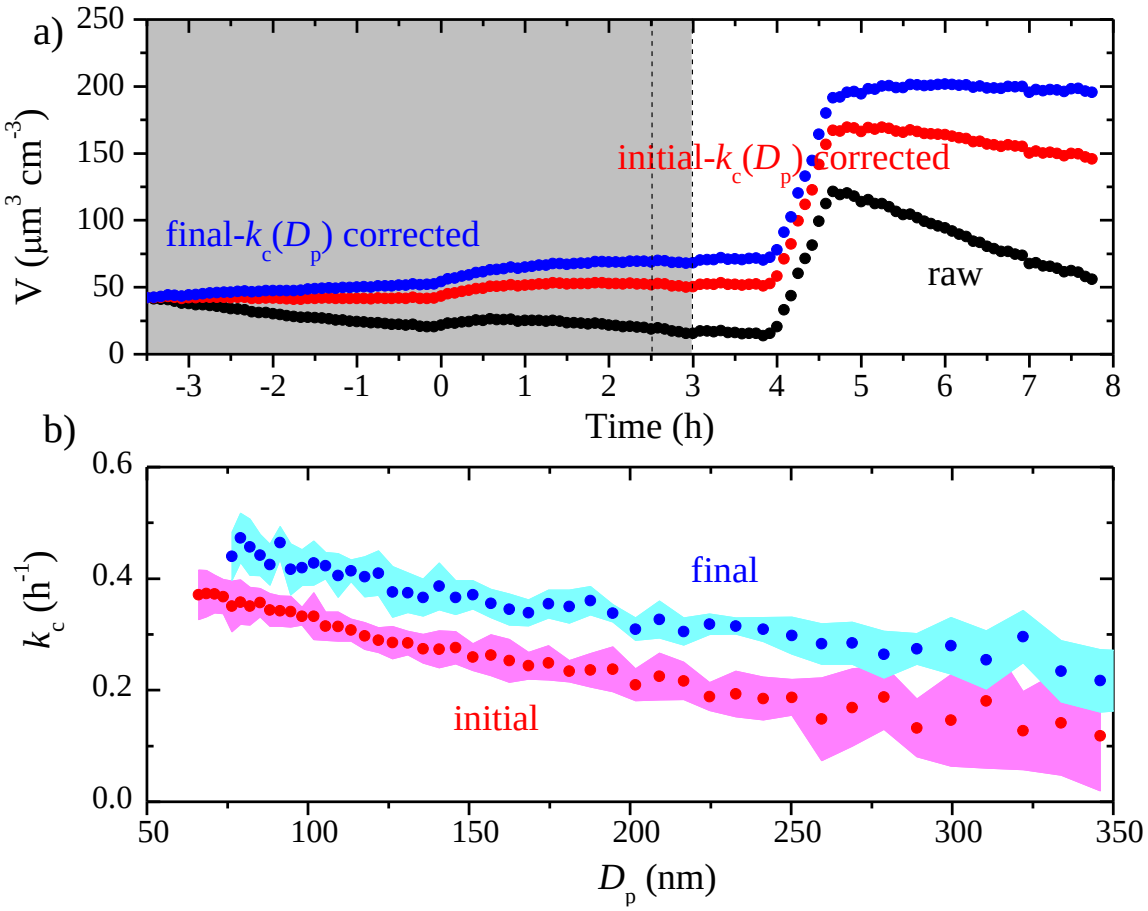

Figure 3.8: a) The SMPS-measured (black symbols), the initial $k_c(D_p)$-corrected (red symbols) and the final $k_c(D_p)$-corrected (blue symbols) particle volume concentration time series for an aging experiment (Exp. 4), together with **b)** the initial (red symbols) and the final (blue symbols) $k_c(D_p)$ profiles. The colored area are the uncertainties associated with the corresponding $k_c(D_p)$. The grey area indicates that the chamber was dark. The two dashed lines mark the beginning and the end of HONO addition into the chamber. Ammonium sulfate seed particles were injected into the chamber at t=4 h.

We define the chamber conditions under which these abnormally high loss rates and

exacerbated time dependence of $k_c(D_p)$ were observed as "disturbed". The $k_c(D_p)$ profiles shown in Fig. 3.3 were under "undisturbed" chamber conditions. Since the affected particles are usually larger than 100 nm where electrostatic forces start to dominate the wall-loss process (McMurry and Rader, 1985), we postulate that excess electrostatic forces within the chamber are most likely the cause of the "disturbed" conditions. Friction created with the Teflon walls was found to be a major contributor to the exacerbated electrostatic forces and thus the "disturbed" chamber conditions.

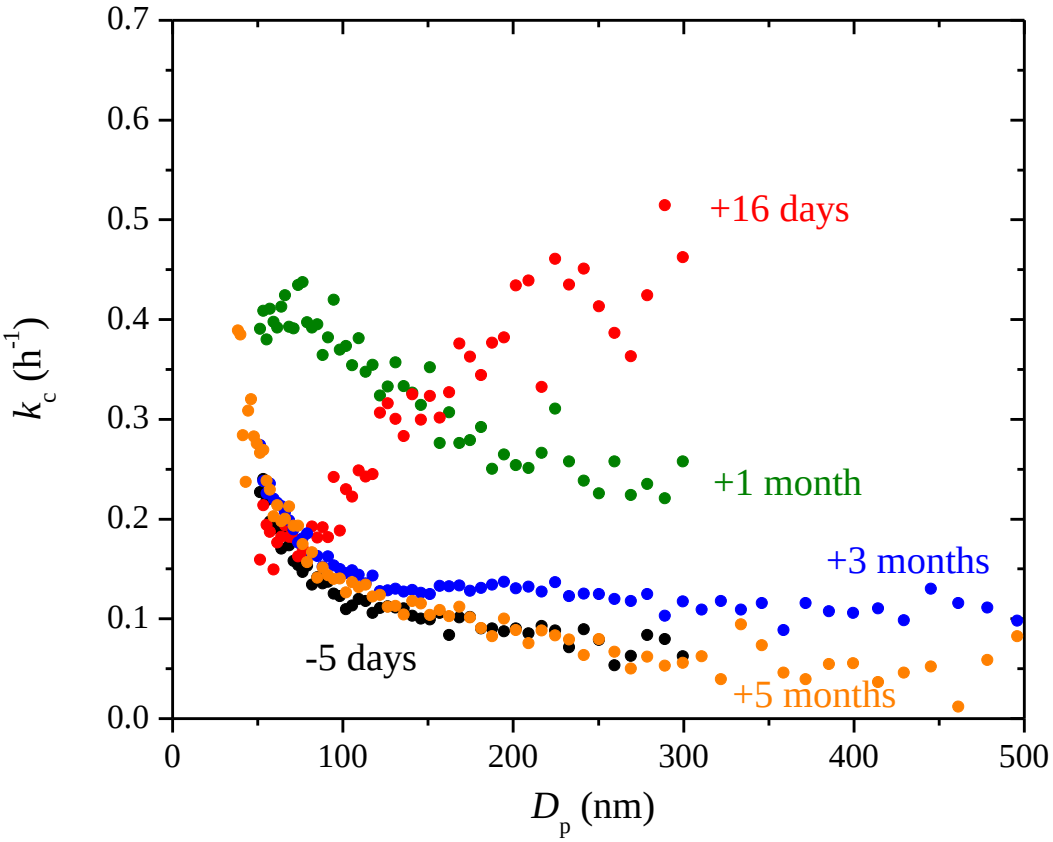

Figure 3.9: The coagulation-corrected particle wall-loss rate constant, k_c, at each diameter derived from experiments with only ammonium sulfate particles in the 12 m^3 CMU Teflon chamber before and after some major maintenance in the room where the chamber is suspended. The chamber was partially deflated and its walls subjected to friction repeatedly during the maintenance.

Fig. 3.9 shows the $k_c(D_p)$ profiles measured over a span of five months after some major maintenance work (Jan. 2016) in the room where the chamber is suspended. During the one-week maintenance, friction with Teflon walls was created by partially deflating the chamber, moving and touching it repeatedly. The measured $k_c(D_p)$ profile changed drastically in shape for days after. The 16-day post-maintenance $k_c(D_p)$ profile presented an increasing trend from 75 nm to 300 nm, with particles bigger than 200 nm getting lost at a rate 3-4 times faster than before. Once we noticed the abnormally high particle loss rates in the chamber, we refrained from being in any form of contact with the chamber walls. The chamber was left suspended and full during those five months. Records of experiments performed in the chamber during that time indicate only regular experimental procedures were carried out. About a month later, the k_c's recovered to the decreasing trend, but were in general high as compared to their pre-maintenance counterparts with values > 0.2 h^{-1} at 300 nm. Three months after the maintenance, particles smaller than 100 nm recovered to its pre-maintenance values while particles bigger than 150 nm still had loss rate constants up to 0.1 h^{-1} higher than before. Five months after, the $k_c(D_p)$'s made a full recovery, with values decreased further to 0.13 h^{-1} at 100 nm, 0.09 h^{-1} at 200 nm and 0.06 h^{-1} at 300 nm. During the 5 months, the chamber was left fully inflated, stationary and suspended in the room. Only steps necessary for an experiment (overnight flushing, injection flow etc.) were taken.

Exp. 4 was performed a month after the major maintenance when $k_c(D_p)$ was still in recovery, and thus the exacerbated electrostatic forces within the chamber likely played a major role in the extra time sensitivity of the $k_c(D_p)$'s in Exp. 4. As discussed above (Fig. 3.8), the final $k_c(D_p)$ profile shifted to higher values after about 4 hours of measurements. To test whether certain steps during this experiment may have been the major cause of the shift, we explored potential impact on $k_c(D_p)$ of turning on the UV lights, injecting HONO and overnight flushing individually

in separate seed experiments. Experiments 5-8 were designed to test each of these factors individually. These experiments were performed about 3 months after the maintenance when

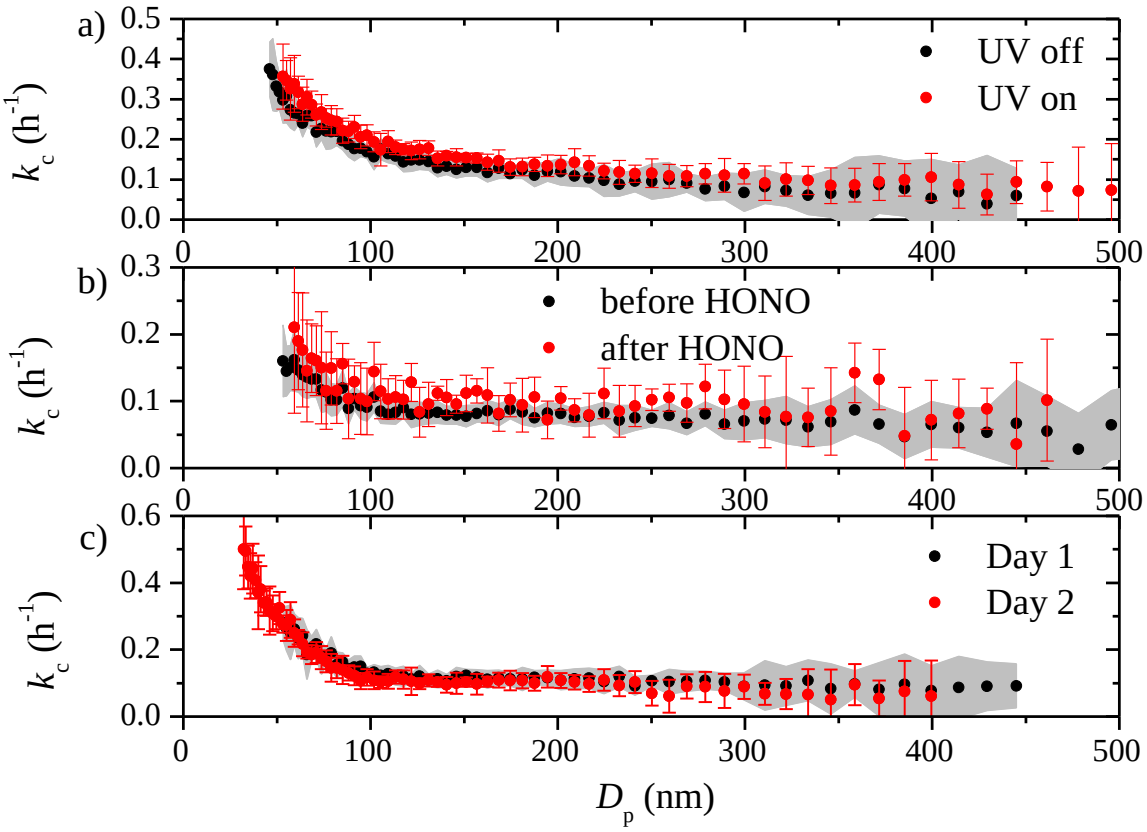

Figure 3.10: The coagulation-corrected particle wall-loss rate constant, k_c, at each diameter for a) Exp. 5, b) Exp. 6, c) Exp. 7 and Exp. 8. The uncertainties associated with the corresponding $k_c(D_p)$ are either expressed as the grey area or the red error bars.

particle wall loss rates have almost recovered to its pre-maintenance values, indicating the chamber has mostly recovered to "undisturbed" conditions. Turning on the UV lights inside the room where the chamber is suspended can cause changes in the air circulation around the chamber walls, thus affecting the turbulence. Carrying HONO into the chamber with a clean air flow at a rate of ~ 5 L min^{-1} for 20 min may potentially impact the turbulence within the chamber. Though cleaning the

chamber with overnight flushing may not have a direct impact of k_c during the day of an experiment, flow rates higher than 100 L min^{-1} into the chamber may well change the its geometry. The results of Experiments 5-8 are shown in Fig. 3.10 and none of the aforementioned processes had evident impact on $k_c(D_p)$. *t*-test results indicated that of the $k_c(D_p)$ profiles derived before and after each factor were statistically the same, respectively. We thus conclude that the usual steps taken during a typical SOA aging experiment do not have a significant impact on k_c if the chamber is in its undisturbed state. However, when the chamber has been disturbed and the losses are already high they also become sensitive to routine changes in the experimental conditions.

3.4.6 Teflon chamber maintenance and operating procedure of chamber experiments

Routine seed experiments appear to be necessary for testing the particle loss rates in Teflon chambers. Any deviation in the particle wall-loss rate constants from the usual values can be a sign of "disturbed" chamber conditions, which may result in higher particle loss rates and time sensitivity of $k_c(D_p)$ during an experiment. As discussed above, friction with the chamber walls can introduce excess electrostatic forces within the chamber and thus introduce significant uncertainty in the particle loss rates. In order to maintain minimum particle loss in Teflon chambers, we should refrain from creating any type of friction with the chamber walls such as touching the walls or having the walls rubbing against each other. When transporting the chambers such as the dual-chamber system, it is ideal to leave them half-filled with air and fixed onto a rigid structure that can be packed during the transportation. This can minimize potential friction and shorten the recovery time for the particle loss rates. Use of metal gloves is recommended when it is absolutely necessary to touch the chamber.

When the chamber is in a "disturbed" state, the $k_c(D_p)$'s can vary with time during the

course of an experiment. It is thus vital in these cases to include two seed loss periods, one at the beginning and the other at the end, for each SOA experiment to characterize the $k_c(D_p)$, especially if the chambers are recently subjected to friction. When performing SOA experiments in a Teflon chamber, we recommend the following operating procedure:

1. injection of seeds and initial $k_c(D_p)$ characterization for 3-4 hours;
2. perform necessary steps for the SOA experiment and wait until the mass loadings in the chamber become low;
3. if the losses in step 1 are high, a second injection and another 3-4 hours of measurements for final $k_c(D_p)$ characterization are necessary.

3.5 Conclusions

Particle number losses in chamber experiments due to coagulation can be significant for small particles (< 150 nm). It is thus important to correct for this coagulation effect when calculating the particle wall-loss rate constants especially for experiments in which the behavior of the nanoparticles is important (e.g., when they carry a significant fraction of the total particle mass).

The CMU chamber used in this study appeared to operate in two different states: an undisturbed and a disturbed one. The chamber entered the second state after either major repairs or even after smaller changes (e.g. addition of a sampling line or replacement of a few lights) probably because it was touched by the researchers or because friction was created during the repairs. The disturbed state could last for several weeks. In this state the particle loss rates increased by more than a factor of 3-4 and their size dependence became more pronounced. There was significant variation of the losses from experiment to experiment and even within the same

experiment. In the undisturbed state, the loss rate constant was less than 0.1 h^{-1} for particles larger than approximately 200 nm and was constant from experiment to experiment. Under these conditions the cleaning of the chamber, turning on the chamber lights, injection of reactants, etc., did not have a statistically significant impact on the loss rate constants.

The accuracy of the use of size-independent loss rate constants for the correction of the experimental results depends on the state of the chamber and the size distribution of the aerosol during the experiment. If the aerosol volume is dominated by particles larger than 200 nm and the chamber is undisturbed its results can be quite accurate. However, if the chamber has been disturbed or if the size distribution during some phase of the experiment includes a lot of ultrafine particles, significant errors can be introduced.

The correction based on the OA/Sulfate ratio can also introduce uncertainties. The SOA mass distribution is usually shifted towards the smaller particles compared to that of the sulfate seeds. As a result, the losses of sulfate can be different than those of the organics. The sign and the magnitude of the error depends on both the differences between the two size distributions and also the size dependence of the losses in this specific experiment. A method to correct the OA/Sulfate ratio for these effects has been developed. In one of the experiment, this explains the apparent decreases of the ratio from 1.0 to 0.9 in less than one hour.

Due to the above complexities, seed experiments for testing the particle loss rates in Teflon chambers should be performed regularly, probable before each experiment. If the rates are high a second measurement of the losses should be performed after the end of the experiment to constrain any potential changes. The use of size-dependent corrections accounting for coagulation effects is the preferred approach even if in a number of experiments when the chamber is undisturbed the errors introduced by neglecting the size dependence or the role of coagulation could be small.

However, this depends a lot on the evolution of the aerosol volume distribution during the experiment and especially on the importance of the particles smaller than 200 nm or so for the objectives of the experiment.

3.6 References

Crump, J. G.; Seinfeld, J. H.; Turbulent deposition and gravitational sedimentation of an aerosol in a vessel of arbitrary shape; J. Aerosol Sci., 2, 405–415, 1981.

Draper, D. C.; Farmer, D. K.; Desyaterik, Y.; Fry, J. L; A qualitative comparison of secondary organic aerosol yields and composition from ozonolysis of monoterpenes at varying concentrations of NO_2; Atmos. Chem. Phys., 15, 12267-12281, 2015.

Fry, J. L.; Draper, D. C.; Barsanti, K. C.; Smith, J. N.; Ortega, J.; Winkler, P. M.; Lawler, M. J.; Brown, S. S.; Edwards, P. M.; Cohen, R. C.; Lee, L.; Secondary organic aerosol formation and organic nitrate yield from NO_3 oxidation of biogenic hydrocarbons; Environ. Sci. Technol., 48, 11944-11953, 2014.

Hennigan, C. J.; Miracolo, M. A.; Engelhart, G. J.; May, A. A.; Presto, A. A.; Lee, T.; Sullivan A. P.; McMeeking, G. R.; Coe, H.; Wold, C. E.; Hao, W.-M.; Gilman, J. B.; Kuster, W. C.; de Gouw, J.; Schichtel, B. A.; Collett Jr. J. L.; Kreidenweis S. M.; Robinson, A. L.; Chemical and physical transformations of organic aerosol from the photo-oxidation of open biomass burning emissions in an environmental chamber; Atmos. Chem. Phys., 11, 7669-7686, 2011.

Henry, K. M. and Donahue, N. M.; Photochemical aging of α-pinene secondary organic aerosol: effects of OH radical sources and photolysis; J. Phys. Chem. A, 116, 5932−5940, 2012.

Hildebrandt, L.; Donahue, N. M.; Pandis, S. N.; High formation of secondary organic aerosol from the photo-oxidation of toluene; Atmos. Chem. Phys., 9, 2973–2986, 2009.

Kaltsonoudis, C.; Louvaris, E.; Florou, K.; Kostenidou, E.; Wang, N.; Liangou, A.; Tsiligiannis, E.; Jorga, S.; Pandis S. N.; A new portable dual smog chamber facility with UV lights for field studies; Atmos Meas Tech., in preparation.

Keywood, M. D.; Varutbangkul, V.; Bahreini, R.; Flagan, R. C.; Seinfeld, J. H. ; Secondary organic aerosol formation from the ozonolysis of cycloalkenes and related compounds; Environ. Sci. Technol., 38, 4157–4164, 2004.

Loza, C. L.; Chhabra, P. S.; Yee, L. D.; Craven, J. S.; Flagan, R. C.; Seinfeld, J. H.; Chemical aging of m-xylene secondary organic aerosol: laboratory chamber study; Atmos. Chem. Phys., 12, 151–167, 2012.

McMurry, P. H. and Grosjean, D.; Gas and aerosol wall losses in Teflon film smog chambers; Environ. Sci. Technol., 19, 1176-1182, 1985.

McMurry, P. H. and Rader, D. J.; Aerosol wall losses in electrically charged chambers; Atmos. Chem. Phys., 4, 249–268, 1985.

Nah, T.; McVay, R. C.; Pierce, J. R.; Seinfeld, J. H.; Ng, N. L.; Constraining uncertainties in particle-wall deposition correction during SOA formation in chamber experiments; Atmos. Chem. Phys., 17, 2297-2310, 2017.

Ng, N. L.; Kroll, J. H.; Chan, A. W. H.; Chhabra, P. S.; Flagan, R. C.; Seinfeld, J. H.; Secondary organic aerosol formation from m-xylene, toluene, and benzene; Atmos. Chem. Phys., 7, 3909–3922, 2007.

Pathak, R. K.; Stanier, C. O.; Donahue, N. M.; Pandis S. N.; Ozonolysis of α-pinene at atmospherically relevant concentrations: temperature dependence of aerosol mass fractions (yields); J. Geophys. Res., 112, D03201, 2007.

Pierce, J. R.; Engelhart, G. J.; Hildebrandt, L.; Weitkamp, E. A.; Pathak, R. K.; Donahue, N. M.; Robinson, A. L.; Adams, P. J.; Pandis, S. N.; Constraining particle evolution from wall losses, coagulation, and condensation-evaporation in smog-chamber experiments: optimal estimation based on size distribution measurements; Aerosol Science and Technology, 42,1001 — 1015, 2008.

Presto, A. A. and Donahue, N. M.; Investigation of α-pinene + ozone secondary organic aerosol formation at low total aerosol mass; Environ. Sci. Technol., 40, 3536–3543, 2006.

Qi, L.; Nakao, S.; Cocker, D. R.; Aging of secondary organic aerosol from α-pinene ozonolysis: Roles of hydroxyl and nitrate radicals; J. Air Waste Manag. Assoc., 62, 1359–1369, 2012.

Seinfeld, J. H., and Pandis, S. N.: *Atmospheric chemistry and physics: from air pollution to climate change*, Third edition. ed., John Wiley & Sons, Inc., Hoboken, New Jersey, 2016.

Stern, J. E.; Flagan R.C.; Grosjean D.; Seinfeld J.H.; Aerosol formation and growth in atmospheric aromatic hydrocarbon photooxidation; Environ. Sci. Technol., 21, 1224-1231, 1987.

Wang, N.; Kostenidou, E.; Donahue, N. M.; Pandis, S. N.; Multi-generation chemical aging of α-pinene ozonolysis products by reactions with OH; Atmos. Chem. Phys. Discuss., 10.5194/acp-2017-746, 2017.

Chapter 4

Multi-generation chemical aging of α-pinene ozonolysis products formed under high NO_x conditions

4.1 Introduction

The role of NO_x ($NO+NO_2$) in secondary organic aerosol (SOA) formation from biogenic volatile organic compounds (VOC) was first investigated in the early 1990s (Paulson et al., 1990; Pandis et al., 1991; Zhang et al., 1992). These chamber studies have found that in general the SOA yields are dependent on the initial VOC to NO_x ratio (Paulson et al., 1990; Pandis et al., 1991), and also identified organonitrate functional groups ($-ONO_2$) in the products (Palen et al., 1992). NO_x can react with the organo-peroxy radicals (RO_2) produced from the oxidation of organic compounds through the following reactions:

$$NO + RO_2 \xrightarrow{k_1} RO + NO_2 \quad \text{(R1)}$$

$$NO + RO_2 \xrightarrow{k_2} RONO_2 \quad \text{(R2)}$$

and form alkoxy radicals (RO) and organonitrates. The branching ratio ($k_2/(k_1+k_2)$) of the radical terminating pathway R2 ranges from 1-35 % depending on the carbon chain length/structure, pressure and temperature (Atkinson and Arey, 2003; Beaver et al., 2012). The NO_2 reaction with RO_2 is generally less important under tropospheric conditions due to rapid thermal decomposition of alkyl peroxynitrates back to reactants though NO_2 is important for peroxyacetyl nitrates (PAN) formation (Atkinson, 2007). By reacting with RO_2, NO_x thus introduces an important additional pathway for RO_2 that would otherwise react with other RO_2 and HO_2 radicals. This critical branching point for the fate of RO_2 is expected to change the product distribution.

More recent chamber studies of the NO_x effect on SOA formation have focused on the impact of the RO_2+NO reaction pathway on aerosol yields and product distribution for the classic α-pinene+O_3 system. They usually minimize undesired reaction pathways by adjusting the corresponding oxidant concentrations or using a scavenger. Some studies have focused on the

competition of the RO_2+NO with the RO_2+HO_2 pathway in the photooxidation of α-pinene (Ng et al., 2007; Eddingsaas et al., 2012) while others focused on the competition of the RO_2+NO against the RO_2+RO_2 pathway in the α-pinene ozonolysis system (Presto et al., 2005; Pathak et al., 2007). In general, the RO_2+NO pathway was found to reduce the SOA yields because it is believed to lead to more volatile products than those formed from the RO_2+HO_2 pathway (Hatakeyama et al., 1991; Ng et al., 2007) or the RO_2+RO_2 pathway (Presto et al., 2005). Chemical transport models have incorporated the NO_x effect on SOA yields by introducing a branching ratio based on relatively simple parameterization developed from these chamber yield measurements (Lane et al., 2008).

Recent chamber studies on chemical aging have shown that the first-generation products from α-pinene ozonolysis under initial low-NO_x conditions have moderate to low SOA forming potential when exposed to additional oxidants such as OH (Wang et al., 2017). The first-generation products from the RO_2+RO_2 and the RO_2+HO_2 pathways that remain in the gas phase can react with additional OH and form second-generation products of lower volatility. Wang et al. (2017) found an increase of 20-40 % in SOA mass concentration after aging. Since the first-generation products from the RO_2+NO pathway of the α-pinene ozonolysis products were found to have higher volatility, we expect them to behave differently when exposed to additional OH.

To our knowledge, no studies so far have probed the additional SOA forming potential from the products of the RO_2+NO pathway in the α-pinene ozonolysis system. In this work, we investigate the oxidation of the first-generation products of α-pinene ozonolysis from the RO_2+NO pathway with additional OH radicals by performing aging experiments of α-pinene ozonolysis products formed under high NO_x conditions. Presto et al. (2005) performed high-NO_x α-pinene ozonolysis experiments in the dark with additional NO_2 and also used a mixture of NO_x under UV

illumination. For the dark ozonolysis experiments under high NO_x, the authors reported SOA yields of 0.3-22 % (at 2-270 μg m^{-3} SOA assuming unit density), and 1-8 % (at 3-8 μg m^{-3} SOA assuming unit density). For the illuminated ozonolysis experiments, the authors found SOA yields of 0-4.3 % (0-3.6 μg m^{-3} SOA assuming unit density). Pathak et al. (2007) performed high-NO_x experiments for this system using NO_2 and found yields around 2.5 % at an SOA level of 5.5 μg m^{-3} (unit density) for both dark and the illuminated experiments. Draper et al. (2015) found that the addition of NO_2 in the dark α-pinene ozonolysis system reduced the aerosol yields due to formation of NO_3 via

$$NO + O_3 \rightarrow NO_2 + O_2 \quad \text{(R3)}$$

$$NO_2 + O_3 \rightarrow NO_3 + O_2 \quad \text{(R4)}$$

The NO_3 reaction with α-pinene has low SOA yields (0-16 %) compared to those of α-pinene ozonolysis (Hallquist et al., 1999; Spittler et al., 2006; Perraud et al., 2010; Fry et al., 2014; Nah et al., 2016). To quantify NO_3 formation in our system, we use a kinetic model to simulate the corresponding reactions and track the fate of RO_2.

4.2 Experimental approach

We conducted the experiments in this work in the 12 m^3 Teflon (Welch Fluorocarbons) environmental chamber at Carnegie Mellon University (CMU). The reactor was suspended in a temperature-controlled room with walls and roof covered with UV lights (GE 10526 and 10244). Prior to each experiment, we flushed the chamber overnight with purified air under UV illumination to remove any residual particles and gas-phase organics. We generated purified air by passing ambient air through a high-efficiency particulate air (HEPA) filter to remove particles, an

activated carbon filter to remove any organics, a Purafil filter to remove NO_x, and finally a silica gel filter, keeping relative humidity (RH) below 5 % in the chamber before each experiment.

Table 4.1: Initial conditions of the experiments performed in this work.

Exp.	α-pinene (ppb)	NO[a] (ppb)	NO_2 (ppb)	O_3 (ppb)	UV	Seed surface area (μm^2 cm^{-3})	HONO injection	First/ Second OH[b] ($\times 10^7$ molec cm^{-3})	OH introduction time (h after α-pinene consumption)
1	55	105+100	9	1000	On	1500	Twice	1.3/1.1	1.3
2	33	85+140	0	900	On	1461	Twice	1.2/0.8	1.2
3	30	32+105	8	1190	On	2079	Twice	1.3/1.2	1.2
4	24	100+270	20	900	On	2076	Once	1.5	1.3
5	13	62	82	280	On	2047	Once	2.9	0.8
6[c]	50	33	1700	450	Off	-	None	-	-
7	50	16	900	400	Off	1105	None	-	-

[a]For Exp. 1-4, 100-270 ppb of NO was injected into the chamber for a second time 15-25 min after the beginning of the ozonolysis.
[b]The OH concentration was calculated using the decay of butanol-d9 (monitored by PTR-MS) (Barmet et al., 2012).
[c]No initial seeds were used in the experiment.

We have performed both ozonolysis-only and ozonolysis plus aging experiments in this work, and the conditions for each experiment are listed in Table 4.1. For seeded experiments, we pumped an ammonium sulfate solution (1 g L^{-1}) at the beginning of each experiment through an atomizer (TSI, model 3076) at a constant rate of 90 mL h^{-1} to produce droplets. The droplets passed through a diffusion dryer and a neutralizer to produce dry ammonium sulfate seed particles. We injected these seeds with a number mode size of 110 nm into the chamber until they reached a number concentration of 3×10^4 cm^{-3}, resulting in an initial seed mass concentration of around 70

μg m^{-3} and a surface area concentration around 1500 μm^2 cm^{-3}. Typical organic vapors with a molar weight of 250 g mol^{-1} had an initial collision frequency of 0.01 s^{-1} with these seeds.

In all experiments, we added NO_x into the chamber from standard mixed cylinders of NO (1 ppm in N_2) or NO_2 (1% NO_2 in N_2) prior to the ozonolysis step. For Exp. 1-4, we introduced additional NO 20-25 min after the ozonolysis started at a constant flow rate using a mass flow controller in line between the chamber the NO cylinder.

We injected α-pinene (Sigma-Aldrich, ≥ 99 %) into the chamber using a septum injector with purified air as carrier flow. We generated ozone using a corona-discharge ozone generator (AZCO, HTU500AC) to initiate the ozonolysis reaction. We prepared a fresh HONO solution in a bubbler by adding a 4.9 g L^{-1} sulfuric acid solution to a 6.9 g L^{-1} sodium nitrite solution. We then turned on the UV lights to start the photo-dissociation of HONO, producing OH.

At the end of each aging experiment, we injected additional ammonium-sulfate seeds into the chamber using the same method with a more concentrated solution (5 g L^{-1}) in order to characterize the particle wall-loss rates a second time.

We added butanol-d9 (Cambridge Isotope Laboratories, 98 %) into the chamber through the septum injector as an OH tracer before the ozonolysis started and used the method described in Barmet et al. (2012) to calculate the OH produced by HONO photolysis. The OH concentration in these experiments was around 1.6×10^7 molecule cm^{-3} for the first hour, then dropped to around 10^6 molecule cm^{-3} afterwards.

We measured the particle size distribution (15-700 nm) using a TSI Scanning Mobility Particle Sizer, SMPS (classifier model 3080 or 3081; CPC model 3010 or 3772), and the particle composition and mass spectrum of the SOA with an Aerodyne High Resolution Time-of-flight Aerosol Mass Spectrometer (HR-Tof-AMS). We monitored the concentrations of α-pinene and

butanol-d9 using a Proton Transfer Reaction-Mass Spectrometer (PTR-MS, Ionicon), the ozone concentration using a Dasibi 1008 ozone monitor (ICE: Teledyne 400E), and NO_x ($NO + NO_2$) levels using a Teledyne API NO_x Analyzer 200A (ICE: Teledyne T201). We held the chamber temperature constant at 22 ^oC throughout all experiments.

4.3 Data analysis

4.3.1 SOA yields

The SOA mass yield, *Y*, is a metric of the ability of a gaseous precursor to form SOA, and is defined as $Y = C_{SOA}/\Delta VOC$, where C_{SOA} is the produced SOA mass concentration (in $\mu g\ m^{-3}$) and ΔVOC the amount of the VOC precursor (α-pinene in this case) reacted (in $\mu g\ m^{-3}$). To separate the effect of aging on SOA mass concentration, we define a first-generation SOA mass yield, $Y_1 = C_{SOA,1}/\Delta VOC$, and a second-generation SOA mass yield, $Y_2 = C_{SOA,2}/\Delta VOC$. $C_{SOA,1}$ and $C_{SOA,2}$ are the concentrations of SOA formed before, and after aging with hydroxyl radicals. All α-pinene reacts away during the first stage and thus ΔVOC for the second stage is the same as the initial α-pinene concentration in the chamber.

4.3.2 Particle wall-loss correction

For the seeded experiments in this work, we adopted the size-dependent particle wall-loss correction method with the coagulation-corrected, particle wall-loss rate constant, $k_c(D_p)$ (Wang et al., 2017; Wang et al., 2018). The coagulation-corrected particle wall-loss rate constants were derived based on the model used by Nah et al. (2016). The model assumes that only two processes take place: particle wall loss and coagulation. Using the measured particle number size distribution at a specific time step, the model simulates its evolution during the next step assuming coagulation

is the only process and using the coagulation rate constants in Seinfeld and Pandis (2006). The model attributes the difference between the predicted size distribution and the measured one to particle wall loss. Then the model calculates the "instantaneous" wall-loss rate constants for each time step for each size. To obtain the coagulation-corrected particle wall-loss rate constant, $k_c(D_p)$, the instantaneous rate constants are averaged over time. The reported uncertainty is calculated $as\ \sigma_{k_c}/\sqrt{N-1}$ where σ_{k_c} is the standard deviation of k_c for a certain size bin and N is the total number of time steps used. To minimize the uncertainty of k_c, we used a time step of 15 min for the averaging of the measurements. Only SMPS measurements from the seed wall-loss periods were used as the inputs for the model.

The corrected particle number concentration at size bin i, $N_i^{tot}(t)$, is calculated by,

$$N_i^{tot}(t) = N_i^{sus}(t) + k_{c,i} \int_0^t N_i^{sus}(t)dt. \quad (1)$$

We can then derive the corrected particle volume concentration at size bin i, $V_i^{tot}(t)$. In order to evaluate how well the correction works, we define the parameter: $\varepsilon_V = 2\sigma_{N_s}/\overline{V_s}$, where σ_{V_s} is the standard deviation of the particle wall-loss corrected volume concentration for the seed wall-loss periods and $\overline{V_s}$ the average. Only when both values of ε_V for the initial and the final seed periods are less than 5 % do we deem the particle wall-loss correction valid for that individual experiment. Experiments in which these criteria were not met were not included in the analysis.

The organic aerosol mass concentration corrected for wall losses can be then calculated during a seeded experiment using:

$$C_{SOA}^{tot}(t) = (V^{tot}(t) - V_s)\rho_{SOA}, \quad (2)$$

where $V^{tot}(t)$ is the corrected total particle volume concentration summed across all sizes, V_s is the corrected seed volume concentration and ρ_{SOA} is the SOA density, assumed to be equal to 1.4 μg m^{-3} (Kostenidou et al., 2007).

For the unseeded Exp. 6 we used the method described in Pathak et al. (2007) that involves determining the first-order particle wall-loss rate constant, *k*, from the SMPS-measured SOA mass concentration after chemical reactions have been completed. The constant *k* is found as the slope of the linear regression:

$$\ln[C_{SOA}^{sus}(t)] = -kt + Q, \quad (3)$$

where $C_{SOA}^{sus}(t)$ is the measured SOA mass concentration at time *t* and *Q* is an arbitrary constant. The values of $C_{SOA}^{sus}(t)$ used for the fit are taken after the SOA production has finished (condensation/evaporation is minimal). The corrected SOA concentration can be found by:

$$C_{SOA}^{tot} = C_{SOA}^{sus}(t) + k\int_0^t C_{SOA}^{sus}(t)dt. \quad (4)$$

4.3.3 Analysis of AMS measurements

We operated the HR-AMS in V mode during the experiments in this work. Squirrel v1.56D was used to analyze the unit resolution data and Pika 1.15D for the high-resolution data. Results based on AMS measurements reported in this work are based on high-resolution analysis. We determined the atomic oxygen to carbon ratio, O:C, based on the correlation described in Caragaratna et al. (2015). The elemental analysis informs the oxidation state of the carbon atoms and thus nitrate fragments (NO^+, NO_2^+) are not included in the calculation of O:C. When reporting organics mass, we attributed the nitrate signals to organics since the only sources of particulate nitrate fragments in these experiments are organonitrates.

To estimate the formation of organonitrates (ON) in these experiments, we assume that the organonitrates are composed of 10-carbon molecules of 250 g mol^{-1} with one $–ONO_2$ function group. Using the nitrogen in the nitrate fragments (NO^+, NO_2^+) measured by the AMS, we were

able to back calculate the mass concentration of the organonitrates, C_{ON}, with the following equation,

$$C_{ON} = C_N \times MW_{ON}/MW_N, \quad (5)$$

where MW refers to the molecular weight of the corresponding species and C_N the nitrogen concentration in μg m^{-3} is calculated by,

$$C_N = C_{NO_2^+} \times MW_N/MW_{NO_2^+} + C_{NO^+} \times MW_N/MW_{NO^+}. \quad (6)$$

4.3.4 Kinetics model

We used a kinetics box model to simulate the first-generation gas-phase chemistry in these experiments. The model contains reactions involving the gas-phase species (α-pinene, NO_x, O_3) and estimates the concentrations of radical species such as OH, RO_2 and NO_3. In the model, the precursor α-pinene can go through three reaction pathways i.e. α-pinene+O_3, α-pinene+OH and α-pinene+NO_3. The model assumes four reaction pathways for RO_2: reaction with RO_2, NO_3, HO_2, NO_x (with the majority being NO). Actinometry experiments were performed in the CMU chamber to determine the corresponding j_{NO_2} for our experiments and it was found to be 0.13 min^{-1}. The model incorporates 26 reactions and simulates the concentration of 16 species. A complete list of reactions and the corresponding rate constants can be found in Table D.1.

4.4 Results and discussion

4.4.1 Aging experiments with high initial NO_x

The SMPS-measured particle volume concentration time series of a typical aging experiment with high initial NO_x (Exp. 1) is shown in Fig. 4.1a. The coagulation-corrected, size-dependent particle wall-loss rate constants derived from the initial seed-loss period shown in Fig.

D1c. The rate constants for 50-400 nm particles are derived from SMPS measurement while those for particles bigger than 400 nm from a constant fit. Applying $k_c(D_p)$ to the SMPS-measured size distributions, we determined the particle-loss corrected aerosol volume concentration, shown in Fig. 4.1a with $\varepsilon_V = 4.2\ \%$. The particle-loss corrected SOA ($\rho_{SOA} = 1.4$ μg m^{-3}) mass concentration time series is shown in Fig. 4.1b with the uncertainty of 4.2 %. The initial seed particles in the chamber were getting lost to the walls from *t*=-3.5-0 h. At *t*=0, ozone was introduced into the chamber to initiate the ozonolysis in the presence of NO_x and UV illumination. The first-generation products formed rapidly and condensed onto the seed particles as the total aerosol mass concentration increased about 50 μg m^{-3}. About an hour after the aerosol mass peaked, we introduced the first HONO with the UV lights off. At *t*=1.6 h, OH radicals were produced under UV illumination and the second round of oxidation occurred, forming an additional 7 μg m^{-3} of SOA. No change in the aerosol mass was observed after the second introduction of OH at *t*=3.2 h. At *t*=4.5 h, seed particles were introduced into the chamber to characterize the particle loss processes for a second time. The AMS-measured organics (CE=1) show similar stepwise increases (Fig. 4.1c) after the oxidations as the SOA derived based on the SMPS measurements. The measured aerosol volume size distributions before oxidation (*t*=0), after the first-generation oxidation (*t*=0.5 h) and after the second-generation oxidation (*t*=4 h) are shown in Fig. D1b. The distribution moved to bigger size range as the multiple generations of condensation occurred, with the majority of the volume distributed across 100-600 nm. The mode diameter of the volume distribution shifted from 250 nm (*t*=0) to 259 nm (*t*=0.5 h) after the first-generation oxidation, and to 269 nm (*t*=4 h) after the second-generation oxidation.

The organics to sulfate ratio (Org:Sulf), nitrates (NO^++NO_2^+) to organics ratio (Nitrates:Org) and the atomic oxygen to carbon ratio (O:C) derived from AMS measurements for

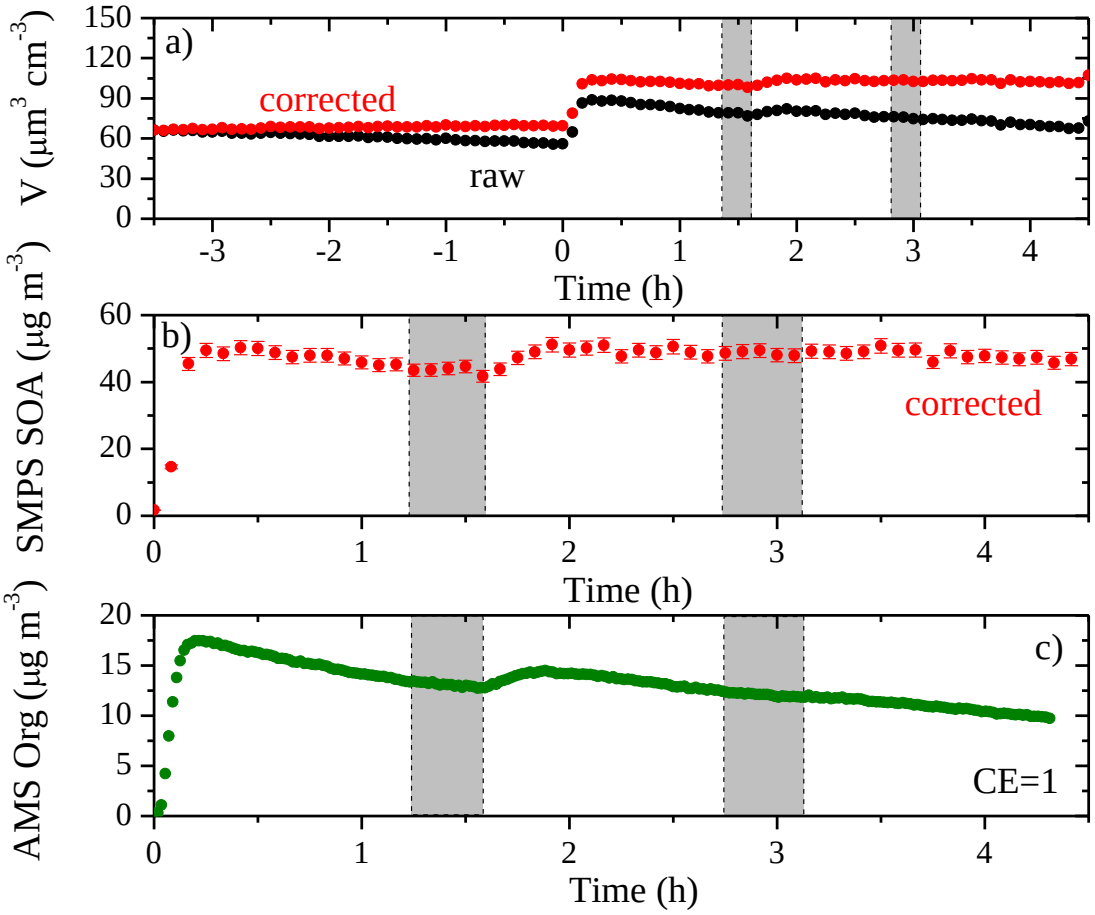

Figure 4.1: a) The SMPS-measured (black symbols) and the particle loss corrected (red symbols) aerosol volume concentration evolution during Exp. 1. **b)** The particle loss corrected SOA mass concentration (ρ=1.4 g cm^{-3}) evolution for Exp. 1 derived from the SMPS measurements. **c)** The AMS-measured organics time series for Exp. 1 with wall loss and collection efficiency corrections (CE=1). Ozone was added into the chamber at time zero to initiate α-pinene ozonolysis under high NO_x and UV illumination. The shaded areas indicate that the chamber was dark. The dashed lines mark the beginning and the end of the two times HONO were added, respectively.

measurements for Exp. 1 are shown in Fig. 4.2. For this experiment, Org:Sulf increased stepwise by about 15 % after the first introduction of OH. No increase was observed after the second OH introduction. The measured nitrate fragments accounted for about 3.7 % of the freshly-formed SOA. Their fraction increased to 4.7 % after the first OH introduction, and to 5 % after the second

OH introduction. The O:C for the freshly formed SOA was 0.41. It then increased stepwise to 0.44 after the first introduction of OH and to 0.45 after the second.

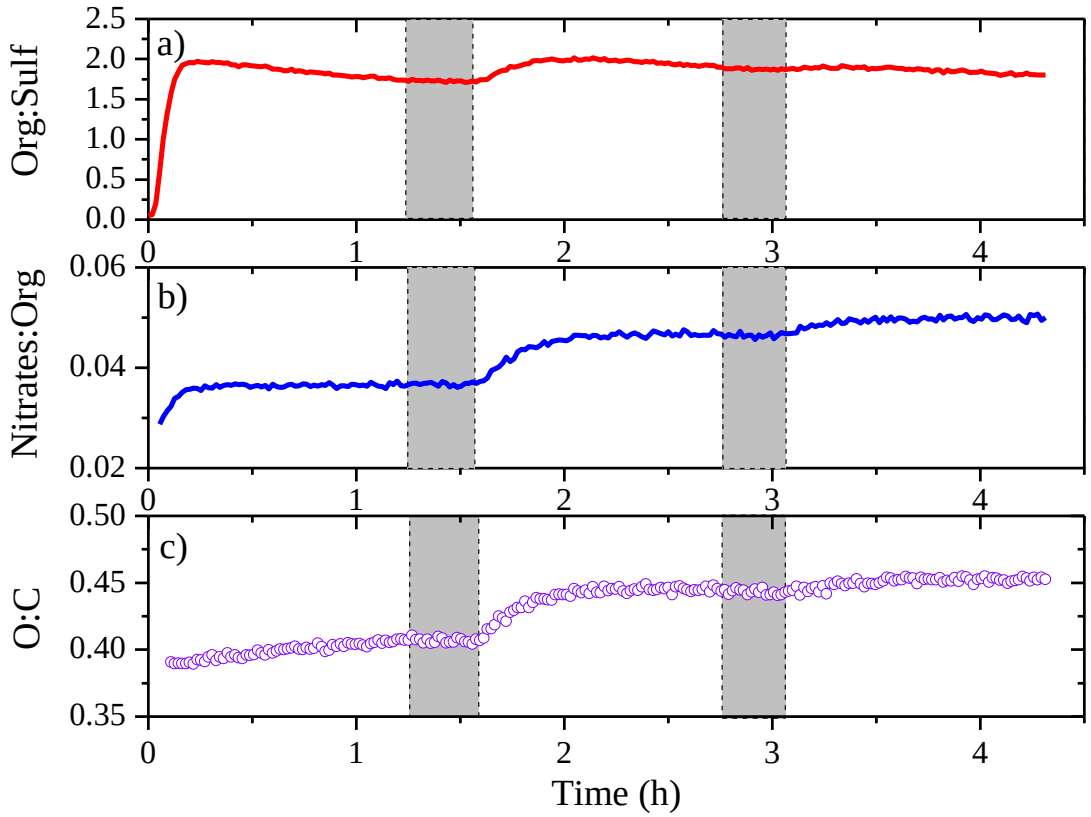

Figure 4.2: The **a)** organics to sulfate ratio, **b)** nitrates (NO^++NO_2^+) to organics (blue) ratio, and **c)** atomic oxygen to carbon ratio time series derived from the AMS measurements for Exp. 1. Ozone was added into the chamber at time zero to initiate α-pinene ozonolysis under UV illumination. The shaded areas indicate that the chamber was dark. The dashed lines mark the beginning and the end of the two times HONO were added, respectively.

The analysis of the AMS spectra suggested that there were few $C_xH_yO_zN_w$ fragments produced (not shown in figures). The formed organonitrates (R-ONO_2) fragmented into R-O- (accounted for in the organics) and –NO_2 (which further fragmented into NO^++NO_2^+ detected as nitrates). The composition of the SOA before and after the exposure to OH can be used to provide

some insight into the chemical composition of the second generation SOA. The fresh SOA in Exp. 1 consisted of 1.9 μg m^{-3} –NO_2, 28.7 μg m^{-3} carbon (C), 15.7 μg m^{-3} additional oxygen (O) and 3.8 μg m^{-3} hydrogen (H). After aging the corresponding concentrations increased by: -NO_2 0.8 μg m^{-3}, C 3.1 μg m^{-3}, O 3 μg m^{-3} and H 0.4 μg m^{-3}. This implies that the additional SOA formed after first OH introduction has an O:C of 0.7, an H:C of 1.5 and an (–NO_2):C of 0.08. Assuming the additional SOA was composed of 10-carbon atoms, its corresponding chemical formula would be $C_{10}H_{15}O_7$-$(NO_2)_{0.8}$. Similar highly oxygenated compounds have been identified as second-generation products from the monoterpene ozonolysis system (Schobesberger et al., 2013).

4.4.2 Comparison of aging effects in low and high initial NO_x systems

The additional SOA formation after the first OH introduction is expressed in percent increase in the SOA concentration derived from the SMPS measurements and Org:Sulf derived from the AMS measurements. The $\Delta[OA]$ and $\Delta[Org:Sulf]$ for Exp. 1-5 are shown in Fig. 4.3. The results derived from the SMPS and the AMS agreed reasonably well for each experiment. From the SMPS, the percent increase in SOA after aging ranges from 15 to 22 % with an average of 20 %. Based on the AMS, the percent increase in Org:Sulf is 15-24 % with an average of also 20 %. Wang et al. (2017) have performed similar aging experiments without initial NO_x, and reported an average of 24 % increase in $\Delta[OA]$ ranging from 20-29 %. Our results are quite similar to those of the low-NO_x experiments.

The absolute increase in O:C after both OH introductions for Exp. 1-5 are shown as a function of OH exposure in Fig. 4.4. In all experiments, a stepwise increase was observed after the first introduction of OH. It took 25–30 min for the O:C to increase 0.03-0.05 for an equivalent of

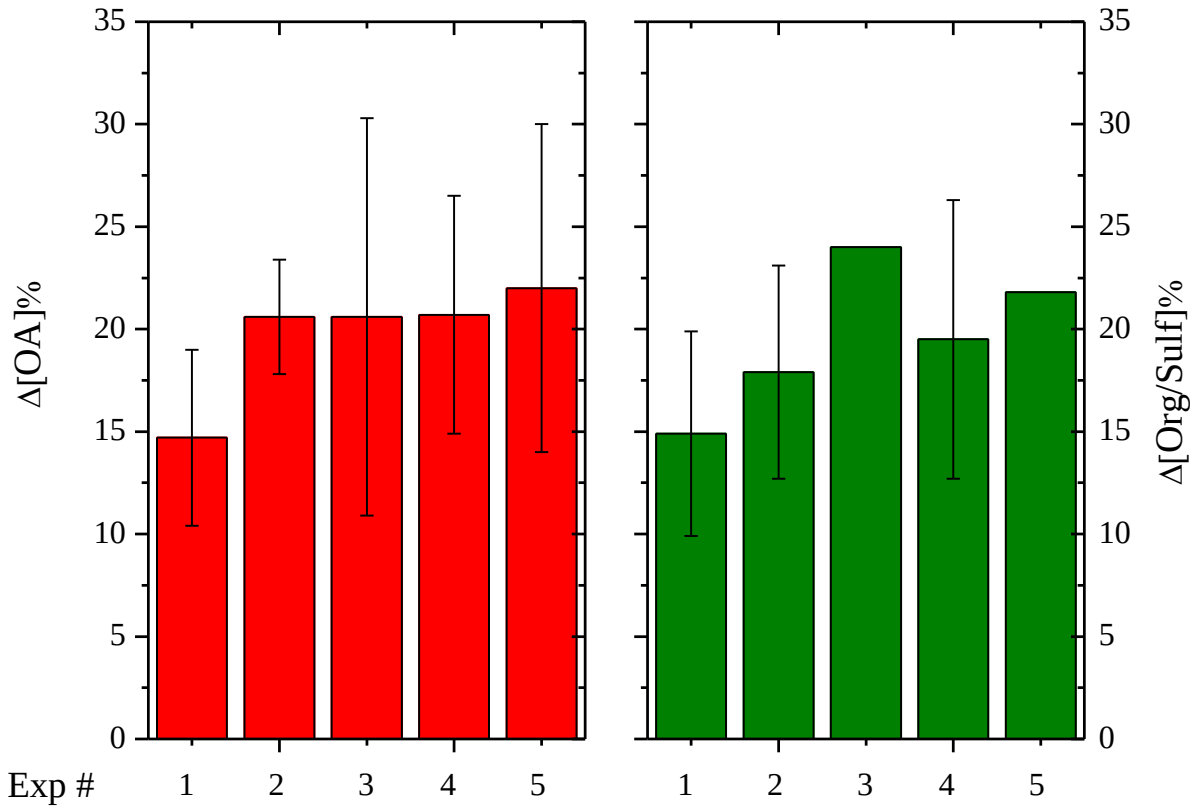

Figure 4.3: The percent increase in the particle loss corrected SOA mass concentration (red) after aging derived from the SMPS measurements, and the percent increase in organic to sulfate ratio (green) derived from the AMS measurements after aging for Exp. 1-5.

2-6 h of ambient daytime exposure (assuming OH=2×10^6 molecule cm^{-3}). This timescale is consistent with the first-generation vapor products reacting with OH and condensing onto the particles (Wang et al., 2017). For Exp. 1-3, a total increase of 0.05-0.06 in the absolute O:C was observed with an ambient equivalent exposure of up to 12 h. The increase in O:C with the corresponding OH exposure for aging experiments with initial NO_x in this work is similar to that observed in aging experiments without initial NO_x from Wang et al. (2017).

Comparing the aging effect on both additional SOA formation and increase in O:C from

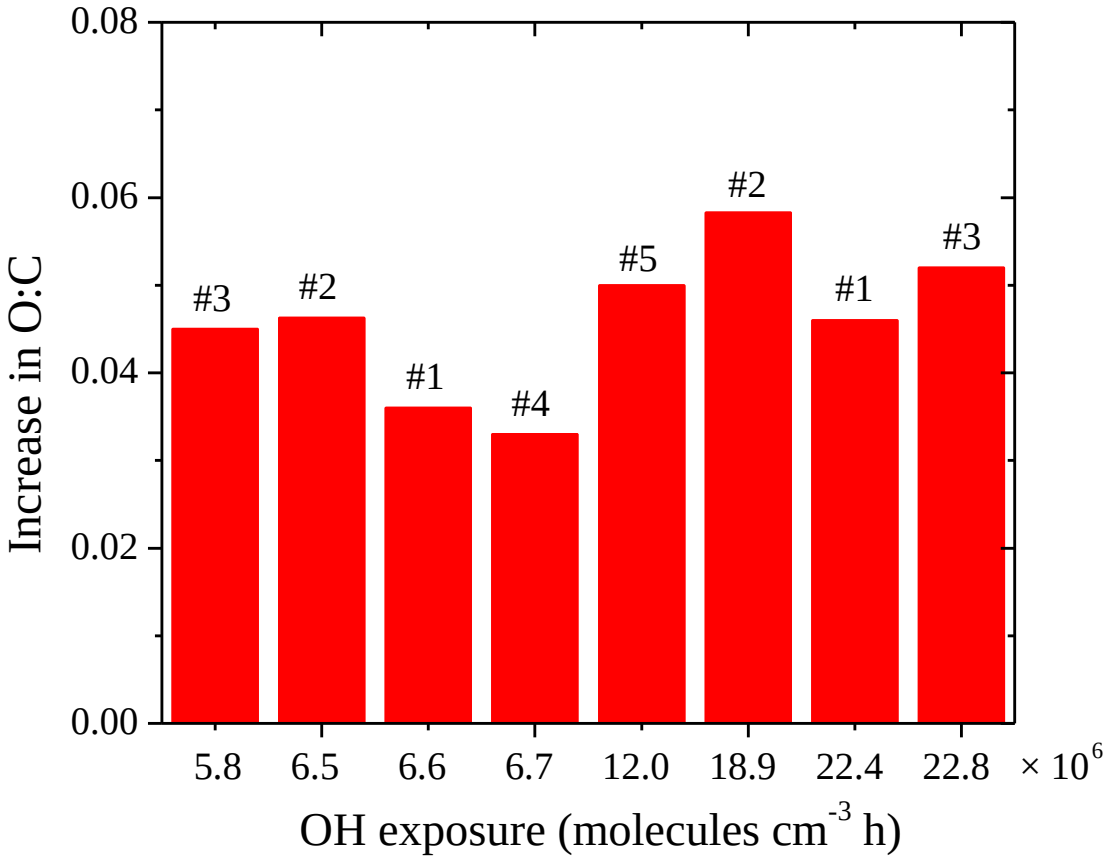

Figure 4.4: The absolute increase in O:C after OH introduction with the corresponding exposure. Experiments 1-3 are plotted twice, both after the first OH introduction and the second, respectively.

Exp. 1-5 to those from the aging experiments without initial NO_x in Wang et al. (2017), we did not observe any major differences.

4.4.3 SOA yields

We compared the first-generation SOA yields of our aging experiments with initial NO_x (Exp. 1-5) to those of aging experiments without initial NO_x from Wang et al. (2017) and those of Henry et al. (2012). The results are shown in Fig. 4.5.

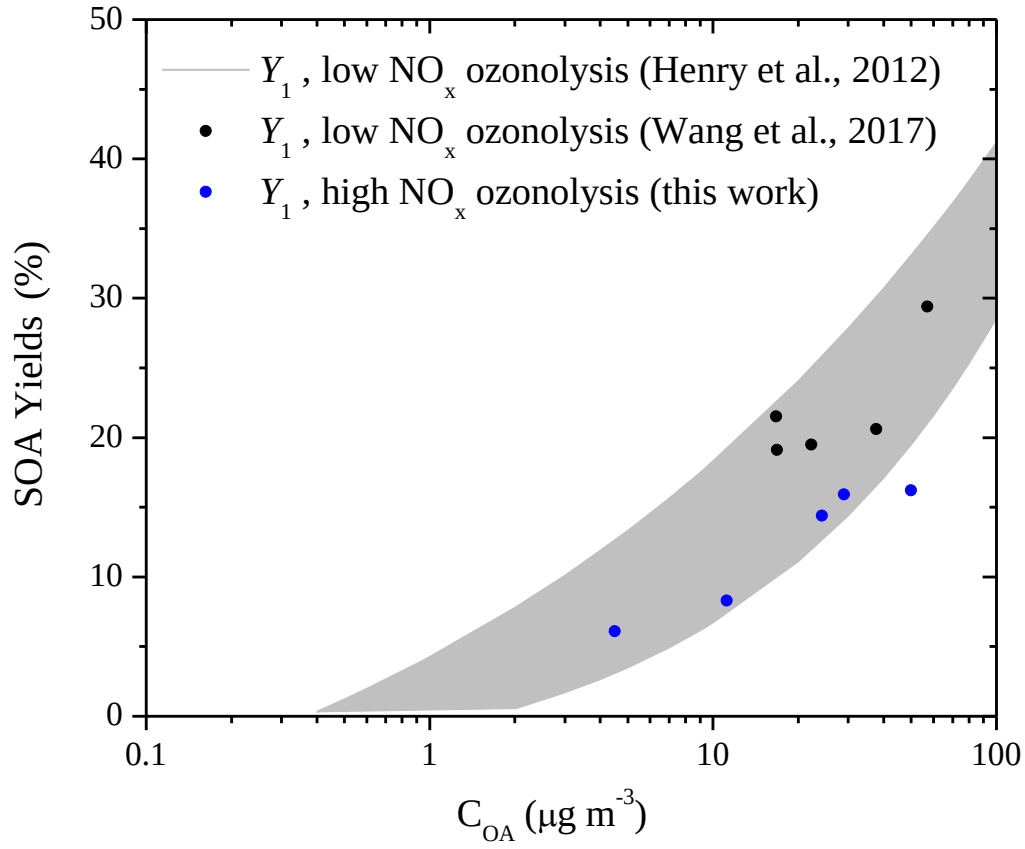

Figure 4.5: The first-generation (blue symbols) high NO_x SOA yields as a function of the formed SOA mass concentration for Exp. 1-5, together with the first-generation (black symbols) low NO_x SOA yields from Wang et al. (2017). The first-generation SOA yields of α-pinene ozonolysis without OH scavenger from Henry et al. (2012) are shown as the grey area. The ozonolysis experiments in this work were performed with initial NO_x while those from Wang et al. (2017) or Henry et al. (2012) without any added NO_x initially.

The first-generation yields from dark ozonolysis without initial NO_x (Wang et al. 2017) fall within the range of those from Henry et al. (2012). The initial yields from ozonolysis with initial NO_x (Exp. 1-5) fall on the lower end of the low-NO_x yields of Henry et al. (2012) or are lower (for example Exp. 1). The yields without initial NO_x (Wang et al. 2017) range from 19-30 % at 20-60 μg $m^{-3}$of SOA. With similar SOA levels, the yields with initial NO_x (Exp. 1-3) are 14-16 %, about

half of those from experiments with no initial NO_x. This supports the previous findings that NO_x can potentially lower the SOA yields in the α-pinene ozonolysis system (Presto et al., 2005; Pathak et al., 2007).

Table 4.2: SOA mass concentration and yields of the experiments performed in this work

Experiment	$C_{SOA,1}$ (μg m^{-3})	Y_1 (%)	$C_{SOA,2}$ (μg m^{-3})	Y_2 (%)	**ΔOA** (μg m^{-3})	**ΔOA** (%)	**Δ[Org/Sulf]** (%)
1	50.0±1.6	16.2	51.2±1.6	16.6	7.3±2.2	14.7±4.3	14.9±5.0
2	29.0±0.5	15.9	35.0±0.6	19.2	6.0±0.8	20.6±2.8	17.9±5.2
3	24.2±1.5	14.4	29.2±1.8	17.4	5.0±2.3	20.6±9.7	24[a]
4	11.2±0.4	8.3	13.5±0.5	10.1	2.3±0.6	20.7±5.8	19.5±6.8
5	4.5±0.2	6.1	5.5±0.3	7.5	1.0±0.4	22.0±8.0	21.8[b]
6[c]	3.5[d]	1.2	NA	NA	NA	NA	NA
7	27.7±0.8	9.8	NA	NA	NA	NA	NA

[a]Uncertainty unavailable due to lack of PToF measurements
[b]Uncertainty unavailable due to noisy PToF measurements caused by low organic mass concentration
[c]No initial seeds were used in the experiment.
[d]Uncertainty unavailable due to lack of seed-loss periods

We also compared the second-generation SOA yields of our aging experiments with initial NO_x (Exp. 1-5) to those of aging experiments without initial NO_x from Wang et al. (2017). The second-generation yields of the aging experiments without initial NO_x (Wang et al. 2017) range from 22-36 % at 25-70 μg m^{-3} of SOA. With similar SOA levels, the second-generation yields of the aging experiments with initial NO_x (Exp. 1-3) are 17-19 % (Table 4.2), also lower than those from experiments with no initial NO_x.

The second-generation yields for Exp. 1-5 range from 7.5-20 %, 0.5-3.5 % higher (in absolute terms) than the first-generation yields. This small to moderate increase is similar to the observed 2-6 % from the aging experiments without initial NO_x from Wang et al. (2017). This is consistent with the fact that the initial NO_x in the system did not significantly impact the aging effect under these experimental conditions.

4.4.4 Kinetics model results

We used the kinetic model to probe the chemistry involved in the first stage of these α-pinene ozonolysis experiments with and without initial NO_x. For the experiment of initial low-NO_x, dark α-pinene ozonolysis, we used the conditions of Exp. 1 from Wang et al. (2017) as the model inputs. The modeled gas and VOC concentrations for the initial stage of the high-NO_x experiment (Exp. 1) and low-NO_x experiment (Wang et al., 2017) are shown in Fig. 4.6, together with the measurements. For Exp. 1, 105 ppb NO and 9 ppb NO_2 were added into the chamber before the ozonolysis. At t=0, about 1000 ppb of O_3 was added into the chamber within 3 min to initiate both the reactions under UV illumination with both the precursor and NO_x. At the meantime, we introduced an additional 100 ppb of NO at a constant flow rate over the next 20 min. The stepwise increase in NO_2 concentration at t=0 corresponds to the consumption of the initial 100 ppb NO, after which it increased steadily over the next 20 min, corresponding to the constant flow of NO into the chamber reacting with excess O_3 continuously. The model captured the NO_x reactions fairly well, and predicted that 55 ppb α-pinene were consumed within 8 min. For the low NO_x experiment, there was no initial NO_x and the chamber was under dark conditions during the ozonolysis step. At t=0, about 480 ppb O_3 was introduced into the chamber to react with α-pinene. After the initial overshoot in its concentration due to injection, the O_3 stabilized at 450 ppb. The

model also captured the decay of O_3 and α-pinene, with 33 ppb of the precursor consumed within half an hour.

In the ozonolysis experiments (Exp. 1-5) with initial NO_x, the model results show that a

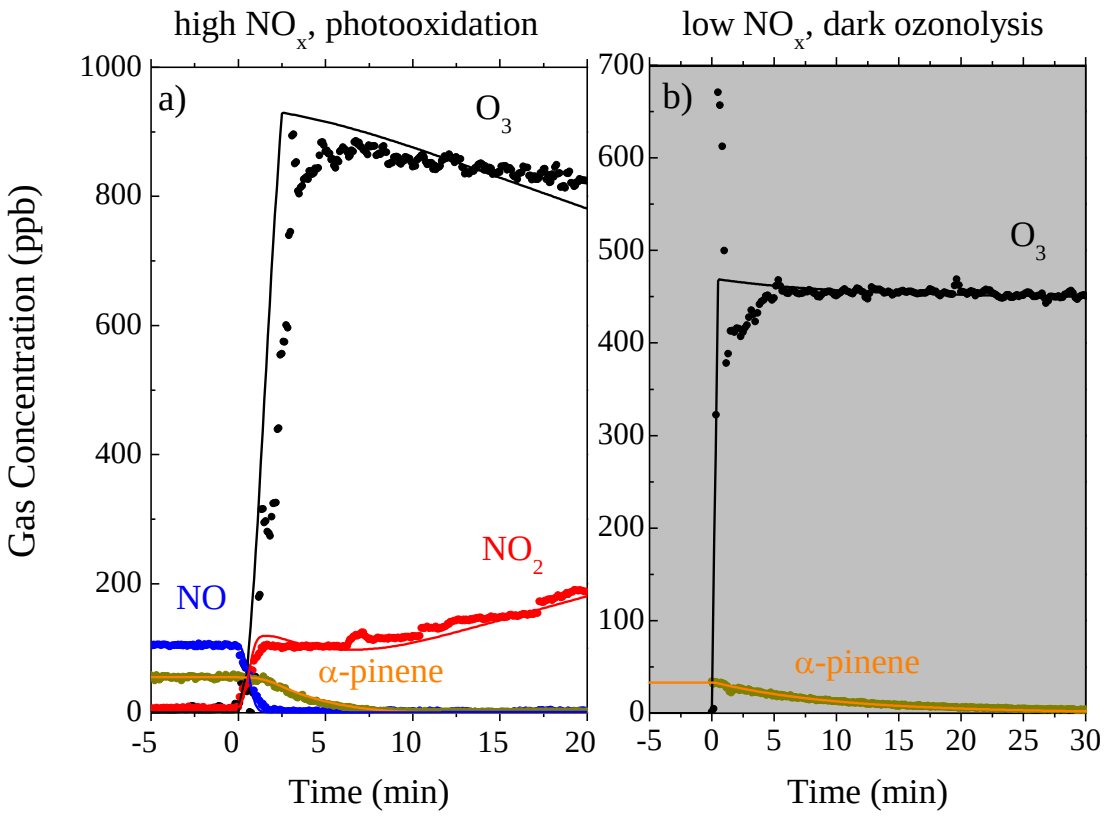

Figure 4.6: Model results of the gas and VOC concentrations (lines) together with the measurements (symbols) for **a)** Exp. 1 and **b)** the low-NO_x dark ozonolysis experiment from Wang et al. (2017).

significant fraction of α-pinene reacted with NO_3 despite the UV illumination. This is mostly due to the rapid and sustained production of NO_3 from the reactions between NO_x and excess O_3, and the lack of NO to efficiently scavenge the NO_3. The rate constant for reaction of α-pinene with NO_3 radicals (Table D1) is 5 orders of magnitude higher than that with O_3, and the NO_x

concentration was at least 4 times that of the precursor. The UV illumination did not sustain a level of NO in the chamber high enough to effectively scavenge the NO_3, nor did it photo-dissociate the NO_3 fast enough. As a result, NO_3 competed against O_3 and OH for the available α-pinene. The α-pinene reacted with the three oxidants for Exp. 1 are shown in Fig. 4.7.

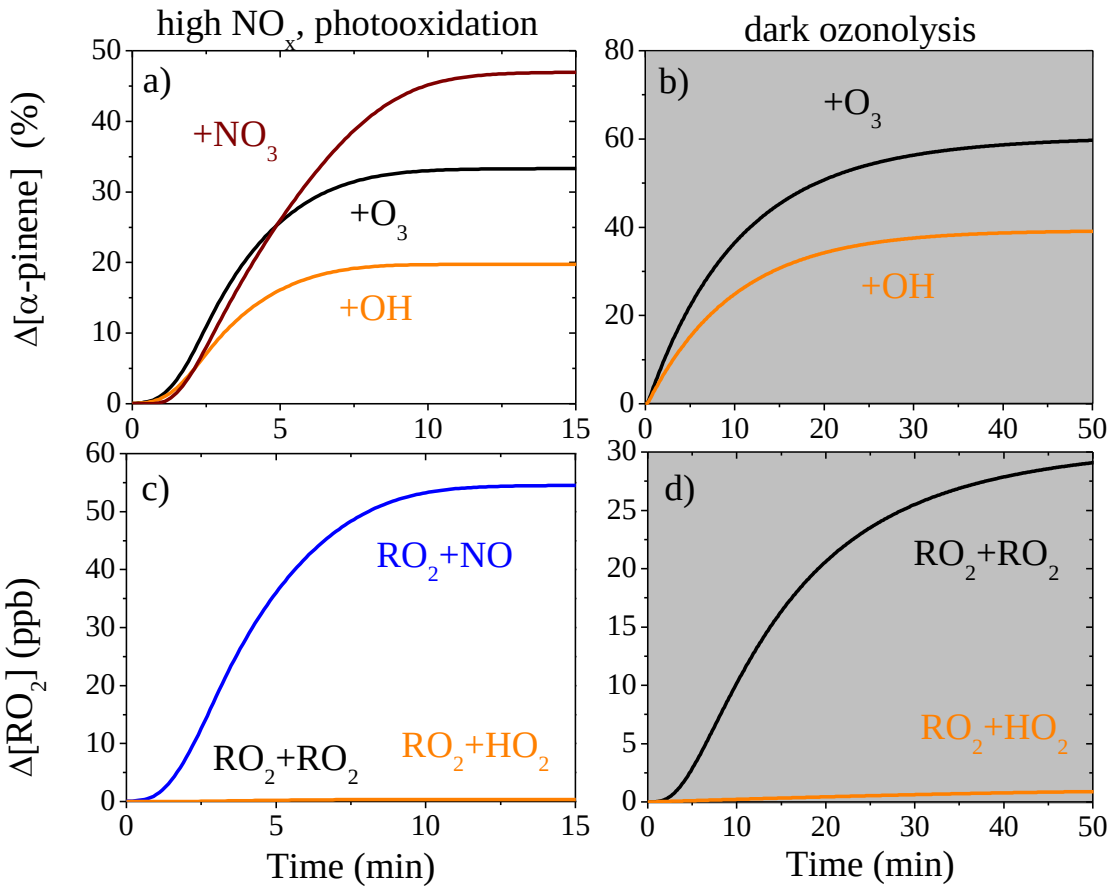

Figure 4.7: Model results of the fractions of α-pinene reacted with O_3, NO_3 and OH and fate of RO_2 for Exp. 1 and the low-NO_x dark ozonolysis experiment from Wang et al. (2017).

As O_3 entered the chamber at t=0, it first reacted with the large amount of NO (compared to α-pinene) due to higher reaction rate constants, resulting in slow α-pinene consumption at t<1 min. The ozonolysis of α-pinene produced OH, which in turn reacted with α-pinene. The NO_3 pathway kicked in at t=1 min due to the fact that the NO_3 has to be generated first through $NO+O_3 \rightarrow NO_2$

and $NO_2+O_3 \rightarrow NO_3$. The precursor was consumed in 12 min with 47 % reacted with NO_3, 33 % with O_3 and 20 % with OH. For the low-NO_x experiment under dark chamber conditions, O_3 reacted with α-pinene immediately after its introduction at t=0. Due to lower concentration of the reactants, the complete consumption of α-pinene took about 50 min. About 60 % of the precursor reacted with O_3 and 40 % with OH. The fractions of α-pinene reacted with different oxidants for experiments in this work are listed in Table 4.3.

Table 4.3: Kinetics box model results for the α-pinene ozonolysis in experiments in this work.

Experiment	**α-pinene** (%)			**RO_2[a]** (ppb)			
	+NO_3	**+O_3**	**+OH**	**+RO_2**	**+HO_2**	**+NO**	**+NO_3**
1	47	33	20	0.1	0.4	54.5	0.0
2	52	31	18	0.0	0.2	32.8	0.0
3	41	37	22	0.1	0.5	29.4	0.0
4	64	24	12	0.0	0.0	23.9	0.0
5	61	28	11	0.0	0.0	13.0	0.0
6[b]	94	5	1	6.6	0.0	4.5	39.0
7	89	8	3	11.3	0.0	2.8	35.9

[a]Minimal RO_2 reacted with NO_2 in all experiments and thus this reaction pathway is not listed.
[b]No initial seeds were used in the experiment.

The fate of RO_2 according to the model for Exp. 1 and the low-NO_x experiment from Wang et al. (2017) are shown in Fig. 4.7. For Exp. 1, >99 % of RO_2 reacted with NO, indicating that this experiment was indeed in the high-NO_x regime. For the low-NO_x experiment, 96 % of RO_2 went through the RO_2+RO_2 pathway and the other 4 % the RO_2+HO_2 pathway. For all aging

experiments in this work (Exp. 1-5), the first-generation chemistry was in the high NO_x regime even if half of the precursor reacted with NO_3 (Table 4.3).

4.4.5 Formation of organonitrates

Fig. 4.8 shows the fractional contribution of organonitrates to total organics during the six seeded experiments in this work plotted against the fraction of RO_2 reacted with NO during ozonolysis and that of the aging experiment without initial NO_x from Wang et al. (2017). During

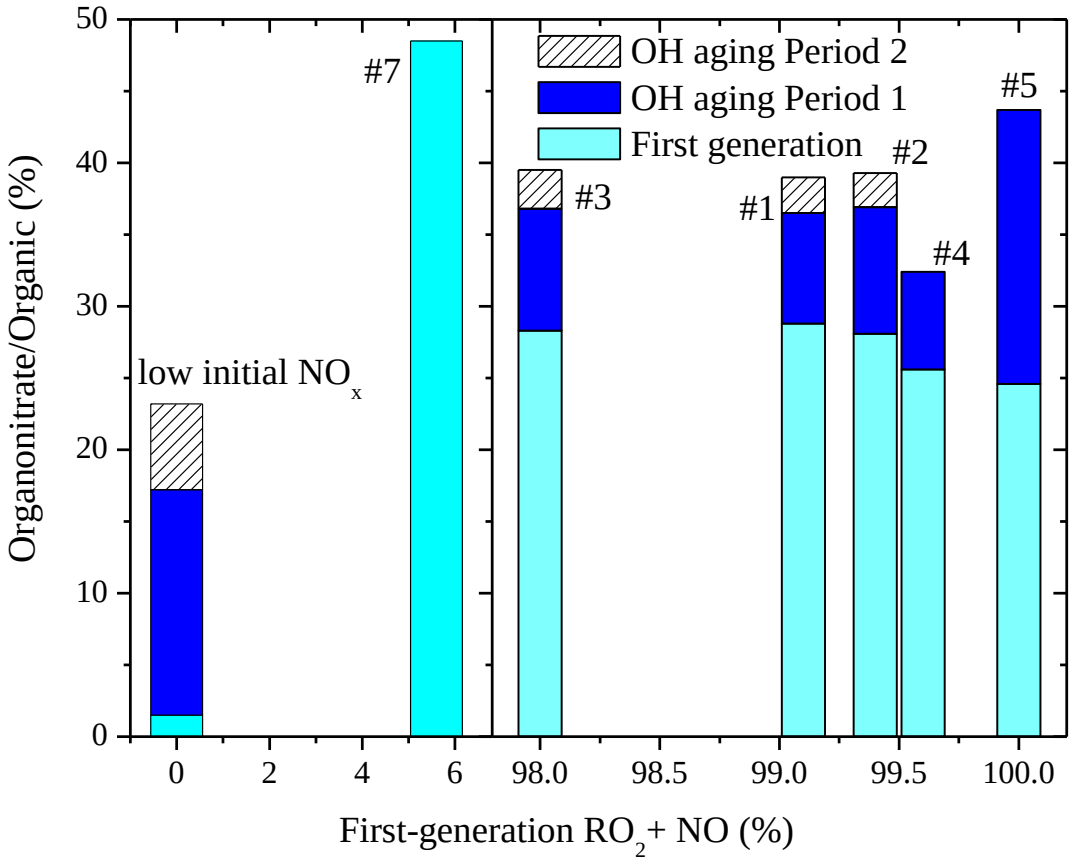

Figure 4.8: The fraction of organonitrates to organics as a function of the fraction of RO_2 reacted with NO for the six seeded experiments and the low initial NO_x aging experiment from Wang et al. (2017). The cyan columns represent the increase in ON/Org during the first-generation oxidation while the blue columns that after the first OH introduction. The hatched columns on top represent the increase in ON/Org after the second OH introduction.

the first-generation oxidation, ON/Org from Exp. 1-5 ranged from 25 % to 29 % with the fraction of RO_2+NO >98 %. Exp. 7 in this work had 89 % of the α-pinene and 72 % of the RO_2 reacted with NO_3, and formed the most (around 50 %) organonitrates during the ozonolysis step. The observed mass fraction of around 50 % of organonitrates in the condensed phase products is similar to the 60 % organonitrates (MW_{ON} =200-300 amu) mass fraction in the SOA formed purely from α-pinene+NO_3 (Nah et al. (2016). Since about half of the precursor in Exp. 1-5 reacted with NO_3, it is plausible that the formation of the organonitrates during the ozonolysis step in these experiments was driven by the α-pinene+NO_3 pathway.

For the experiment from Wang et al. (2017) performed without initial NO_x, ON/Org is close to zero initially as expected. With the first introduction of HONO, high concentrations of NO_x (>1000 ppb) were introduced into the chamber. The fractional contribution of organonitrates to organics increased once we turned on the UV lights. The ON/Org increased to 7-19 % with the first introduction of OH and by an additional 3-6 % with the second introduction of OH.

4.4.6 SOA yields from α-pinene+NO_3

The fact that a significant amount of the precursor reacted with NO_3 in these experiments with initial NO_x and excess O_3 suggests that the SOA yield reduction observed in previous chamber studies of this kind was not solely due to the high-NO_x conditions influencing molecular products from ozonolysis (i.e. RO_2+NO). We performed Exp. 7 as an attempt to replicate conditions in previous chamber studies (Presto et al., 2005). Exp. 7 is an ozonolysis experiment with high initial NO_2 and under dark conditions. Model results shown in Fig. 4.9 indicate that around 90 % of the precursor reacted with NO_3 and 72 % of the RO_2 reacted with NO_3 without UV illumination. Before *t*=0, we introduced about 900 ppb of NO_2 and 16 ppb NO into the chamber. O_3 was injected

into the chamber at *t*=0 and started reacting with both the NO_x and the precursor. NO_3 radicals were rapidly produced from the NO_2+O_3 reaction, and reacted with the α-pinene. Due to the dark conditions and the lack of NO in the system, only 6 % of the RO_2 went through the RO_2+NO pathway. This experiment is a typical example of experiments with initial high NO_x concentrations while the fate of RO_2 is other than consumption by NO. UV illumination is key to the RO_2+NO pathway due to regeneration of NO.

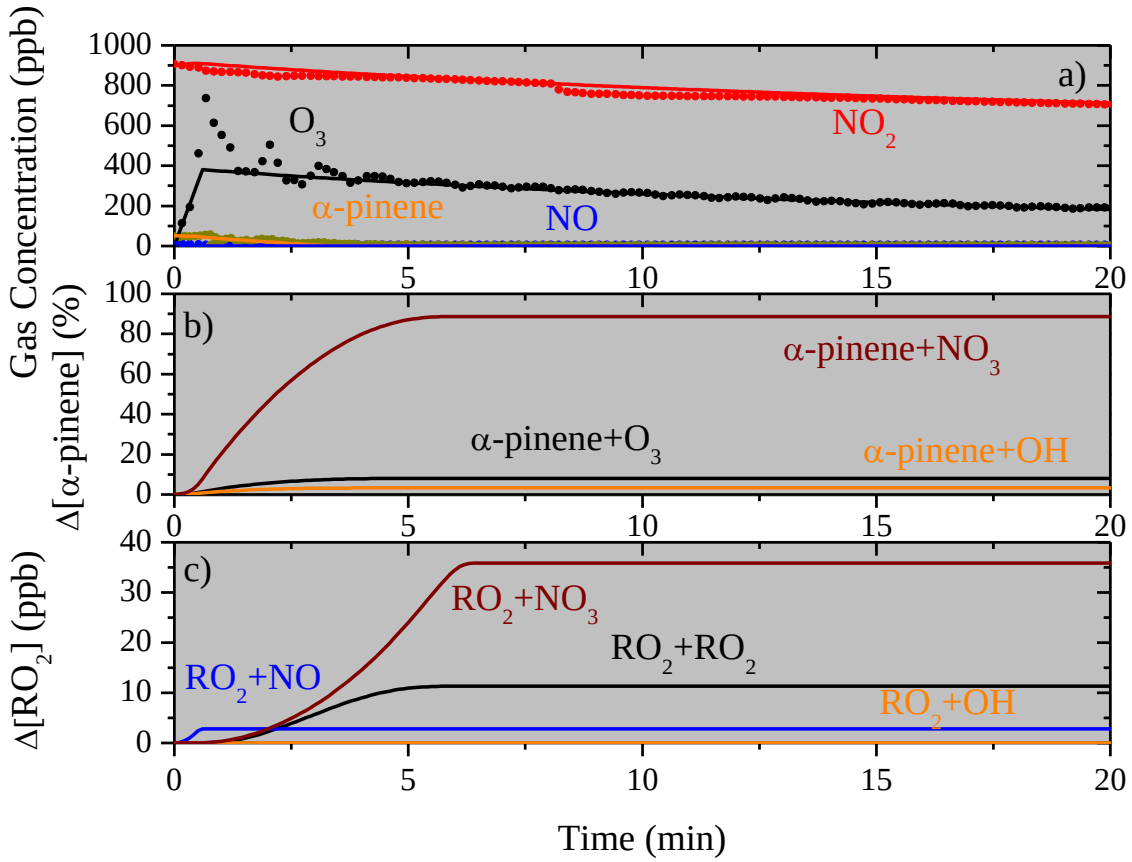

Figure 4.9: Model results of **a)** gas and VOC concentrations (lines) together with the measurements (symbols); **b)** fractions of α-pinene reacted with O_3, NO_3 and OH; **c)** amount of RO_2 reacted with NO, RO_2, NO_x and OH for Exp. 7.

Previous chamber studies of α-pinene+NO_3 with initial precursor concertation relevant to

this study (α-pinene<50 ppb) have found close to zero SOA yields (Hallquist et al., 1999; Fry et al., 2014). Fry et al. (2014) reported a yield of zero with 48 ppb of precursor, and Hallquist et al. (1999) reported yields of 0.4 % and 1 % at the corresponding SOA (ρ_{SOA} adjusted to 1.4 g cm^{-3}) level of 0.2 μg $m^{-3}$and 0.5 μg m^{-3}, respectively. With a higher precursor concentration (approximately 100 ppb), Hallquist et al. (1999) reported an SOA yield of 9.8 % at 54.4 μg m^{-3} of SOA. We observed an SOA yield of 9.8 % from Exp. 7, but at a lower SOA level of 27.7 μg m^{-3}. We thus postulate that the seed particles (1105 μm^2 cm^{-3}; mode diameter of 113 nm) used in Exp. 7 reduced significantly the condensation of products formed from the α-pinene+NO_3 pathway to the walls of the chamber. To test this hypothesis, we performed Exp. 6 with the same precursor concentration (50 ppb) as that of Exp. 7, but without initial seeds. According to the model, the chemistry of Exp. 6 is similar to that of Exp. 7, with 94 % of the precursor and 78 % of the RO_2 reacted with NO_3 (Table 4.3). We observed an SOA yield of 1.2 % (at 3.5 μg m^{-3}) from Exp. 6 as compared to the 9.8 % (at 27.7 μg m^{-3}) from Exp. 7. The results from these two experiments suggest that the seed surface concentration (1105 μm^2 cm^{-3}) was enough to compete with the chamber walls and reduced the losses of the products from the α-pinene+NO_3 reaction.

Most earlier experiments on SOA formation from α-pinene+NO_3 have been conducted in nucleation conditions (Hallquist et al., 1999), and it is plausible that the α-pinene+NO_3 reaction does not produce rapidly a sufficient yield of extremely low volatility species to cause nucleation. During the period before nucleation, condensation to the walls is the only pathway available for semivolatile organics with concentrations above saturation. Fry et al. (2014) performed the α-pinene+NO_3 experiment with initial seeds, but reported a mode diameter of 40 nm for the seed particles. Compared to the 110 nm in this work, it is likely that there was not enough particle present to compete effectively with the chamber walls. Previous experiments have shown that SOA

mass yields from the reaction of β-pinene+O_3 are extremely sensitive to seed surface area (Pathak et al., 2008), and models with wall uptake of condensable vapors have shown that this can be

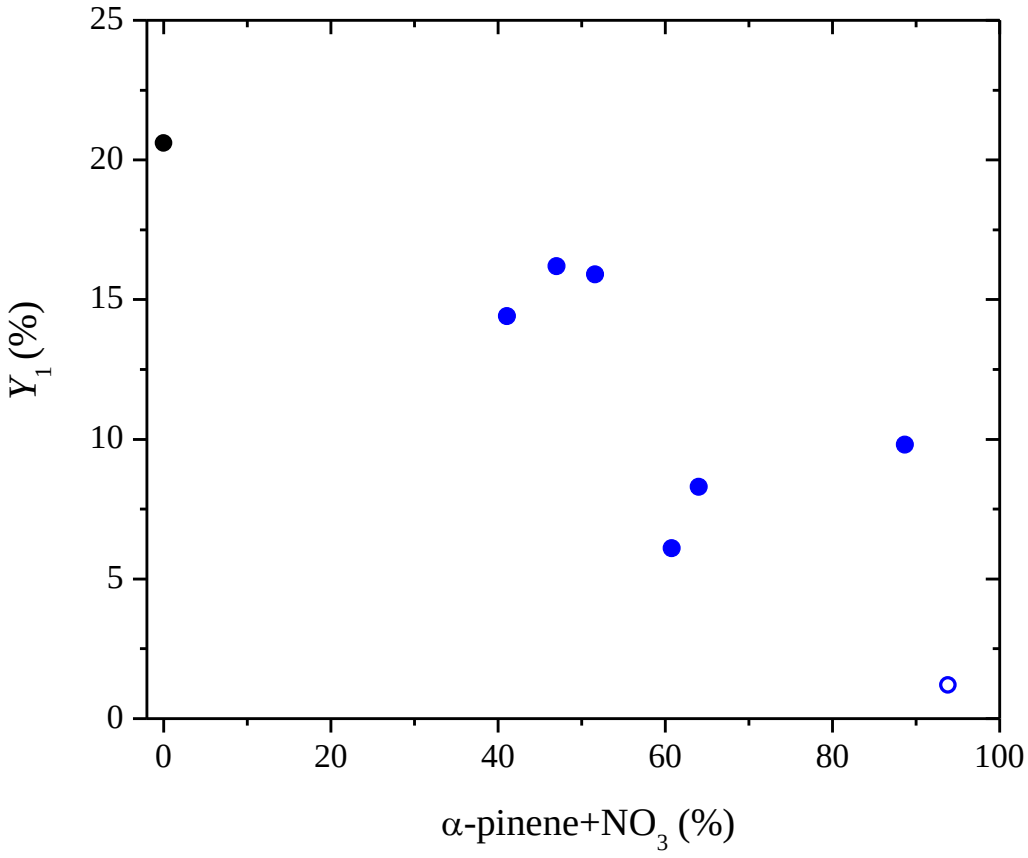

Figure 4.10: The first-generation yields (blue) of all 7 experiments in this work and that of the aging experiment without initial NO_x from Wang et al. (2017) (black) as a function of the fraction of α-pinene reacted with NO_3. The open symbol represents the first-generation yield from the unseeded Exp. 6.

explained by uptake of condensable (but non-nucleating) vapors to the chamber walls. Nah et al. (2016) performed seeded chamber experiments of the α-pinene+NO_3 system with the initial seed number and volume concentration of 1.6×10^4 cm^{-3} and 36 μg m^{-3}, similar to those of experiments in this work. With 12 ppb precursor, they reported SOA yields of 3.5 % and 1.7 % at 2.4 μg m^{-3}

and 1.2 μg m^{-3} (ρ_{SOA} adjusted to 1.4 g cm^{-3}), respectively, significantly higher than the close to zero yields observed from previous chamber studies under similar conditions.

Fig. 4.10 shows the first-generation yields of all 7 experiments in this work as a function of the fraction of α-pinene reacted with NO_3, together with that of the aging experiment without initial NO_x from Wang et al. (2017). The yields in general present a decreasing trend as the fraction of α-pinene reacted with NO_3 increases, with the yield for the unseeded Exp. 6 close to zero.

4.4.7 SOA ozonolysis yields from RO_2+NO

In our high-NO_x experiments (Exp. 1-5) during which >98 % RO_2 reacted with NO, about half of the precursor reacted with NO_3, which appeared to have reduced the apparent ozonolysis yields. This complicates the determination of how the RO_2 fate may have affected the first-generation yields in this system compared to those of the low initial NO_x experiments from Wang et al. (2017). Based on our model results, minimum RO_2 reacted with HO_2 in both systems (Fig. 4.7). Assuming that the yield of 9.8 % at 27.7 μg m^{-3} from Exp. 7 is the yield from the α-pinene+NO_3 pathway, we can deduce the high-NO_x ozonolysis yields for Exp. 2 and Exp. 3 of similar SOA levels since we know the fraction of α-pinene reacted with NO_3 versus O_3 and OH (Table 4.3). At 29 μg m^{-3}, the first-generation yield of Exp. 2 is 15.9 %. Therefore, 95.5 μg m^{-3} (out of the total 185 μg m^{-3}) α-pinene reacted with NO_3, and should produce 9.4 μg m^{-3} SOA. Assuming the SOA formation from each α-pinene pathway in this system is independent, the SOA formed from the α-pinene+O_3/OH in Exp. 2 should be 19.6 μg m^{-3} corresponding to a yield of 21.9 %. The corresponding point falls right among the low initial NO_x experiments in Fig. 4.5. Performing the same zeroth order estimate for Exp. 3 with a first-generation SOA yield of 14.4 % at 24.2 μg m^{-3} while the SOA formed from the α-pinene+O_3/OH should be 17.4 μg m^{-3} with the

yield being 17.6 %. This point aligns well with the low initial NO_x experiments from Wang et al., (2017) as plotted in Fig. 4.5.

The results of this simple exercise suggest that the RO_2+NO pathway yields similar SOA concentrations as the RO_2+RO_2 one for the α-pinene ozonolysis system. Given that the main products of these two pathways are both RO, it is not unreasonable that the SOA yields are similar.

4.5 Conclusion

For the α-pinene ozonolysis experiments performed in this work with high initial NO_x conditions, we observed up to 25 % additional SOA formation after aging, and an absolute increase of 0.03-0.06 in O:C with OH exposure equivalent to 1-2 days of ambient daytime conditions. These increases in both SOA formation and O:C are similar to those observed in the aging experiments with low initial NO_x conditions performed by Wang et al. (2017). The first-generation yields of these high NO_x experiments ranged from 14-16 % for SOA of 24-50 μg m^{-3}, about half of those from low-NO_x α-pinene ozonolysis experiments.

Model results show that about half of the precursor in these high-NO_x ozonolysis experiments reacted with NO_3 while >98 % RO_2 reacted with NO. Organonitrates accounted for around 27 % of the first-generation SOA. Their fractional contribution to total SOA increased to 37-43 % after aging.

The first-generation yield reduction observed in our high-NO_x experiments was due to the α-pinene+NO_3 pathway forming less SOA. The yield from this pathway was 9.8 % at an SOA level of 27.7 μg m^{-3}. The observed close to zero yields of this pathway from previous studies were probably underestimated due to the lack of seeds. This indicates that although the products from the α-pinene+NO_3 pathway are of higher volatility and unlikely to nucleate by themselves, a seed

surface concentration of >1100 μm^2 cm^{-3} is conducive to their condensation. The α-pinene in our experiments reacted with O_3, NO_3 and OH. Decoupling these SOA pathways is challenging. Our zeroth-order estimation suggests that the RO_2+NO pathway yielded similar amount of SOA compared to the RO_2+RO_2 alternative.

For these chamber experiments with initial high NO_x and excess O_3, a significant amount of the precursor will react with NO_3. UV illumination is key to ensure that during high NO_x experiments the majority of RO_2 reacts with NO. These call into question some results of previous high-NO_x chamber studies that had excess O_3 and no UV illumination. To study the effect of the RO_2+NO pathway on SOA yields for the α-pinene ozonolysis system, it is important to reduce the levels of NO_3 radicals in these chamber experiments.

4.6 References

Atkinson, R., and Arey, J.: Atmospheric degradation of volatile organic compounds, Chemical Reviews, 103, 4605-4638, 2003.

Atkinson, R.: Gas-phase tropospheric chemistry of organic compounds: a review, Atmospheric Environment, 41, 200–240, 2007.

Barmet, P., Dommen, J., DeCarlo, P. F., Tritscher, T., Praplan, A. P., Platt, S. M., Prévôt, A. S. H., Donahue, N. M., and Baltensperger, U.: OH clock determination by proton transfer reaction mass spectrometry at an environmental chamber, Atmos. Meas. Tech., 5, 647–656, 2012.

Beaver, M. R., Clair, J. M. St., Paulot, F., Spencer, K. M., Crounse, J. D., LaFranchi, B. W., Min, K. E., Pusede, S. E., Wooldridge, P. J., Schade, G. W., Park, C., Cohen, R. C., and Wennberg, P. O.: Importance of biogenic precursors to the budget of organic nitrates: observations of multifunctional organic nitrates by CIMS and TD-LIF during BEARPEX 2009, Atmos. Chem. Phys., 12, 5773-5785, 2012.

Canagaratna, M. R., Jimenez, J. L., Kroll, J. H., Chen, Q., Kessler, S. H., Massoli, P., Hildebrandt Ruiz, L., Fortner, E., Williams, L. R., Wilson, K. R., Surratt, J. D., Donahue, N. M., Jayne, J. T., and Worsnop, D. R.: Elemental ratio measurements of organic compounds using

aerosol mass spectrometry: characterization, improved calibration, and implications, Atmos. Chem. Phys., 15, 253-272, 2015.

Draper, D. C., Farmer, D. K., Desyaterik, Y., and Fry, J. L.: A qualitative comparison of secondary organic aerosol yields and composition from ozonolysis of monoterpenes at varying concentrations of NO_2, Atmos. Chem. Phys., 15, 12267-12281, 2015.

Eddingsaas, N. C., Loza, C. L., Yee, L. D., Chan, M., Schilling, K. A., Chhabra, P. S., Seinfeld, J. H., and Wennberg, P. O.: α-pinene photooxidation under controlled chemical conditions – Part 2: SOA yield and composition in low- and high-NO_x environments, Atmos. Chem. Phys., 12, 7413-7427, 2012.

Fry, J. L., Draper, D. C., Barsanti, K. C., Smith, J. N.; Ortega, J., Winkler, P. M., Lawler, M. J., Brown, S. S., Edwards, P. M., Cohen, R. C., and Lee L.: Secondary organic aerosol formation and organic nitrate yield from NO_3 oxidation of biogenic hydrocarbons, Environ. Sci. Technol., 48, 11944-11953, 2014.

Hallquist, M.; Wängberg, I.; Ljungstrom, E.; Barnes, I.; Becker, K: Aerosol and product yields from NO_3 radical-initiated oxidation of selected monoterpenes, Environ. Sci. Technol., 33, 553, 1999.

Hatakeyama, S., Izumi, K., Fukuyama, T., Akimoto, H., and Washida, N.: Reactions of OH with α-pinene and β-pinene in air: Estimates of global CO production from the atmospheric oxidation of terpenes, J. Geophys. Res., 96, 947–958, 1991.

Henry, K. M., Lohaus T., and Donahue, N. M.: Organic aerosol yields from α-pinene oxidation: bridging the gap between first-generation yields and aging chemistry, Environ. Sci. Technol., 46, 12347−12354, 2012.

Kostenidou, E., Pathak, R. K., and Pandis, S. N.: An Algorithm for the calculation of secondary organic aerosol density combining AMS and SMPS data, Aerosol Science and Technology, 41, 1002–1010, 2007.

Lane, T. E., Donahue, N. M., and Pandis, S. N.: Effect of NO_x on secondary organic aerosol concentrations, Environ. Sci. Technol., 42, 6022-6027, 2008.

Nah, T., Sanchez, J., Boyd, C. M. and Ng, N. L.: Photochemical aging of α-pinene and β-pinene secondary organic aerosol formed from nitrate radical oxidation, Environ. Sci. Technol., 50, 222-231, 2016.

Ng, N. L., Chhabra, P. S., Chan, A. W. H., Surratt, J. D., Kroll, J. H., Kwan, A. J., McCabe, D. C., Wennberg, P. O., Sorooshian, A., Murphy, S. M., Dalleska, N. F., Flagan, R. C., Seinfeld, J. H.: Effect of NO_x level on secondary organic aerosol (SOA) formation from the photooxidation of terpenes, Atmos. Chem. Phys., 7, 5159-5174, 2007.

Palen, E. J., Allen, D. T., Pandis, S. N., Paulson, S. E., Seinfeld, J. H., and Flagan, R. C.: Fourier transform infrared analysis of aerosol formed in the photo-oxidation of isoprene and β-pinene: Atmospheric Environment, 26, 1239-1251, 1992.

Pandis, S. N., Paulson, S. E., Seinfeld, J. H., and Flagan, R. C.: Aerosol formation in the photooxidation of isoprene and β-pinene, Atmospheric Environment, 25, 997-1008, 1991.

Pathak, R., Presto, A. A., Lane, T. E., Stanier, C. O., Donahue, N. M., and Pandis, S. N.: Ozonolysis of α-pinene: parameterization of secondary organic aerosol mass fraction, Atmos. Chem. Phys., 7, 3811-3821, 2007.

Pathak, R., Donahue, N. M., and Pandis, S. N.: Ozonolysis of β-Pinene: Temperature dependence of secondary organic aerosol mass fraction, Environ. Sci. Technol., 42, 5081-5086, 2008.

Paulson, S. E., Pandis, S. N., Baltensperger, U., Seinfeld, J. H., Flagan, R. C., Palen, E. J., Allen, D. T., Schaffner, C., Giger, W., and Portmann, A.: Characterization of photochemical aerosols from biogenic hydrocarbons, Journal of Aerosol Science, 21, 245-248, 1990.

Perraud, V., Bruns, E. A., Ezell, M. J., Johnson, S. N., Greaves, J., and Finlayson-Pitts, B. J.: Identification of organic nitrates in the NO_3 radical initiated oxidation of α-pinene by atmospheric pressure chemical ionization mass spectrometry, Environ. Sci. Technol., 44, 5887–5893, 2010.

Presto, A. A., Huffhartz, K. E., and Donahue, N. M.: Secondary organic aerosol production from terpene ozonolysis. 2. Effect of NO_x concentration, Environ. Sci. Technol., 39, 7046–7054, 2005.

Schobesberger, S., Junninen, H., Bianchi, F., Lönn, G., Ehn, M., Lehtipalo, K., Dommen, J., Ehrhart, S., Ortega, I. K., and Franchin, A.: Molecular understanding of atmospheric particle formation from sulfuric acid and large oxidized organic molecules, P. Natl. Acad. Sci. USA, 110, 17223–17228, 2013.

Seinfeld, J. H., and Pandis, S. N.: *Atmospheric chemistry and physics: from air pollution to climate change*, Third edition. ed., John Wiley & Sons, Inc., Hoboken, New Jersey, 2016.

Spittler, M., Barnes, I., Bejan, I., Brockmann, K. J., Benter, T., and Wirtz, K.: Reactions of NO_3 radicals with limonene and α-pinene: Product and SOA formation, Atmos. Environ., 40, 116−127, 2006.

Wang, N., Kostenidou, E., Donahue, N. M., and Pandis, S. N.: Multi-generation chemical aging of α-pinene ozonolysis products by reactions with OH, Atmos. Chem. Phys. Discuss., 10.5194/acp-2017-746, 2017.

Wang, N., Jorga, S. D., Pierce, J. R., Donahue, N. M., and Pandis, S.N.: Particle wall-loss correction methods in smog chamber experiments, Aerosol Science and Technology, in preparation, 2018.

Zhang, S.-H., Shaw, M., Seinfeld, J. H., and Flagan, R. C.: Photochemical aerosol formation from α-pinene- and β-pinene, J. Geophys. Res., 97, 20717–20729, 1992.

Chapter 5

Summary and suggestions for future work

5.1 Summary

We investigated the effect of chemical aging on SOA formation and composition for the α-pinene ozonolysis system via smog chamber experiments. The effect of initial NO_x levels in the aging processes was also explored. We adopted a particle correction method that addresses both the size and the time dependence of the particle wall-loss rate and explored the potential complications introduced by particle coagulation. Finally, we proposed an operating procedure for Teflon smog chamber to achieve minimal particle wall loss for precise SOA quantification.

The OH aging of the α-pinene ozonolysis products formed 20-40 % additional SOA mass for an OH exposure equivalent to 2-4 days. Elevating RH up to 50 % had minimum effect on SOA production due to aging. A more oxygenated product distribution was observed after aging. A stepwise increase of 0.02-0.04 in O:C was observed within half an hour after the first introduction of OH. During additional exposure to OH, the O:C grew continuously until the end of the experiments with an absolute increase of up to 0.04. During this second period, minimum SOA production was observed. We attribute this phenomenon to condensed-phase reactions.

Particle number losses in chamber experiments due to coagulation can be significant for small particles (< 150 nm). It is thus important to correct for this coagulation effect when calculating the particle wall-loss rate constants especially for experiments in which the behavior of the nanoparticles is important (e.g., when they carry a significant fraction of the total particle mass).

The CMU chamber used in this study appeared to operate in two different states: an undisturbed and a disturbed one. The chamber entered the second state after either major repairs or even after smaller changes (e.g. addition of a sampling line or replacement of a few lights) probably because it was touched by the researchers or because friction was created during the

repairs. The disturbed state could last for several weeks. In this state the particle loss rates increased by more than a factor of 3-4 and their size dependence became more pronounced. There was significant variation of the losses from experiment to experiment and even within the same experiment. In the undisturbed state, the loss rate constant was less than 0.1 h^{-1} for particles larger than approximately 200 nm and was constant from experiment to experiment. Under these conditions the cleaning of the chamber, turning on the chamber lights, injection of reactants, etc., did not have a statistically significant impact on the loss rate constants.

The accuracy of the use of size-independent loss rate constants for the correction of the experimental results depends on the state of the chamber and the size distribution of the aerosol during the experiment. If the aerosol volume is dominated by particles larger than 200 nm and the chamber is undisturbed its results can be quite accurate. However, if the chamber has been disturbed or if the size distribution during some phase of the experiment includes a lot of ultrafine particles, significant errors can be introduced.

The correction based on the OA/Sulfate ratio can also introduce uncertainties. The SOA mass distribution is usually shifted towards the smaller particles compared to that of the sulfate seeds. As a result, the losses of sulfate can be different than those of the organics. The sign and the magnitude of the error depends on both the differences between the two size distributions and also the size dependence of the losses in this specific experiment. A method to correct the OA/Sulfate ratio for these effects has been developed. In one of the experiment, this explains the apparent decreases of the ratio from 1.0 to 0.9 in less than one hour.

Due to the above complexities, seed experiments for testing the particle loss rates in Teflon chambers should be performed regularly, probable before each experiment. If the rates are high a second measurement of the losses should be performed after the end of the experiment to constrain

any potential changes. The use of size-dependent corrections accounting for coagulation effects is the preferred approach even if in a number of experiments when the chamber is undisturbed the errors introduced by neglecting the size dependence or the role of coagulation could be small. However, this depends a lot on the evolution of the aerosol volume distribution during the experiment and especially on the importance of the particles smaller than 200 nm or so for the objectives of the experiment.

For the α-pinene ozonolysis experiments performed in this work with high initial-NO_x conditions, we observed up to 25 % additional SOA formation after aging, and an absolute increase of 0.03-0.06 in O:C with OH exposure equivalent to 1-2 days of ambient daytime conditions. These increases in both SOA formation and O:C are similar to those observed in the aging experiments with initial low-NO_x conditions. The first-generation yields of these initial high-NO_x experiments ranged from 14-16 % for SOA of 24-50 μg m^{-3}, about half of those from low-NO_x α-pinene ozonolysis experiments.

Model results show that about half of the precursor in these high-NO_x ozonolysis experiments reacted with NO_3 while >98 % RO_2 reacted with NO. Organonitrates accounted for around 27 % of the first-generation SOA. Their fractional contribution to total SOA increased to 37-43 % after aging.

The first-generation yield reduction observed in our high-NO_x experiments was due to the α-pinene+NO_3 pathway forming less SOA. The yield from this pathway was 9.8 % at an SOA level of 27.7 μg m^{-3}. The observed close to zero yields of this pathway from previous studies were probably underestimated due to the lack of seeds. This indicates that although the products from the α-pinene+NO_3 pathway are of higher volatility and unlikely to nucleate by themselves, a seed surface concentration of >1100 μm^2 cm^{-3} is conducive to their condensation. The α-pinene in our

experiments reacted with O_3, NO_3 and OH. Decoupling these SOA pathways is challenging. Our zeroth-order estimation suggests that the RO_2+NO pathway yielded similar amount of SOA compared to the RO_2+RO_2 alternative.

For these chamber experiments with initial high NO_x and excess O_3, a significant amount of the precursor will react with NO_3. UV illumination is key to ensure that during high NO_x experiments the majority of RO_2 reacts with NO. These call into question some results of previous high-NO_x chamber studies that had excess O_3 and no UV illumination. To study the effect of the RO_2+NO pathway on SOA yields for the α-pinene ozonolysis system, it is important to reduce the levels of NO_3 radicals in these chamber experiments.

5.2 Suggestions for future work

In this work we quantified the additional SOA formation during aging and explored the changes in the SOA composition via the overall oxygen to carbon ration (O:C). Future studies should focus on the chemical processes taking place during aging at a molecular level. With the help of the chemical ionization mass spectrometer (CIMS) or other instruments using soft ionization techniques such studies are now possible.

Use of a thermodenuder (TD) could help in the study of the volatility of the various SOA components before and after aging. This especially important for the organonitrates for which there have been few experimental measurements of their saturation vapor pressure.

Future experiments of the α-pinene ozonolysis conducted in an NO_3-free environment that focus on the competition of SOA formation between the RO_2+NO and the RO_2+RO_2 pathway will facilitate the development of better SOA parameterizations under high NOx conditions. Very high

actinic fluxes to maximize the rate of NO_3 photolysis and optimization of the reactant concentrations could help to achieve this goal.

Appendices

Appendix A
Dual-chamber perturbation experiment of ambient air on CMU campus

A.1 Experimental procedure

A.1.2 The dual-chamber system

We conducted this experiment in the CMU dual-chamber system with two pillow-shaped Teflon (PTFE) reactors (1.5 m^3 each) mounted on metal frames. A panel of UV lights (Osram, L36W/73) were lined on the floor below the chambers. A detailed description of this system can be found in Kaltsonoudis et al. (2018). Sampling between the two chambers was altered every four minutes by an automated three-way valve. In order to eliminate interferences and memory effects due to this periodical alteration of the sampling direction, adequate time (1 min) was allowed within the 4-min sampling cycle for the lines to be flushed with the sample air from the next chamber. This is achieved by synchronizing the line flushing with the measuring instrumentation and discarding the 1-min period.

A.1.2 Experimental procedure

Prior to the experiment, we flushed the chambers overnight with purified air under UV illumination to remove any residual particles and gas-phase organics. We generated purified air by passing ambient air through a high-efficiency particulate air (HEPA) filter to remove particles, an activated carbon filter to remove any organics, a Purafil filter to remove NO_x, and finally a silica gel filter, keeping relative humidity (RH) below 5 % in the chamber before each experiment. The chambers were left in a state where there was just enough air inside to keep the walls away from

each other. Before the experiment, we measured the particle concentrations in the chambers to make sure that they were practically zero.

On the day of the experiment, we sampled ambient air outside the CAPS Air Quality lab for a few hours through a metal sampling line. Once the ambient conditions were stable, we started filling the chambers with ambient air using a dual-head Metal Bellows pump (model MB-602). The instruments kept measuring ambient conditions during the filling process. The filling took about 20 min. After this, we switched the sampling from ambient air to the two chambers.

During the first 15 min the air inside the two chambers was characterized. We then added butanol-d9 (Cambridge Isotope Laboratories, 98 %) as an OH tracer into both chambers through a septum injector. Freshly prepared HONO (4.9 g L^{-1} sulfuric acid solution + a 6.9 g L^{-1} sodium nitrite solution) was injected only into the perturbation chamber for about 3 min to produce OH upon UV illumination. We then turned on the UV lights illuminating both the perturbed and the control chamber.

After the completion of the perturbation experiment, we conducted a seed wall-loss experiment to characterize the particle wall-loss rate constants for the two chambers. We refilled the chambers with clean air (about 1/3 of the volume was lost during the 3 hours of sampling). We pumped an ammonium sulfate solution (5 g L^{-1}) into the chambers through an atomizer (TSI, model 3076) at a constant rate of 90 mL h^{-1} to produce droplets. The droplets passed through a diffusion dryer and a neutralizer to produce dry ammonium sulfate seed particles.

A.1.3 Instrumentation

We measured the particle size distribution using a TSI Scanning Mobility Particle Sizer,

SMPS (classifier model 3081; CPC model 3775), and the particle composition and mass spectrum of the OA with an Aerodyne High Resolution Time-of-flight Aerosol Mass Spectrometer (HR-Tof-AMS). We monitored the VOC concentrations and butanol-d9 using a Proton Transfer Reaction-Mass Spectrometer (PTR-MS, Ionicon), the ozone concentration using a Dasibi 1008 ozone monitor (ICE: Teledyne 400E), and NO_x ($NO + NO_2$) levels using a Teledyne API NO_x Analyzer 200A (ICE: Teledyne T201). The relative humidity (RH) in both chambers after filling remained around 20 %, and the temperature around 23 ^oC during the experiment.

A.2 Results and discussion

The SMPS-measured particle number and volume concentration during the experiment are shown in Fig. A.1. The instruments were measuring ambient conditions during the filling process of the chambers from t=-0.5 h to t=0. The total ambient number concentration measured by the SMPS was 8000 cm^{-3} while the corresponding volume concentration was 8 μm^3 cm^{-3}. The number size distribution peaked at D_p=70 nm, while the volume at 250 nm (Fig. A.2). After filling, we switched the instruments to sample from the chambers at time zero. The initial concentration of particles in both chambers was 3000 cm^{-3} (volume concentration 2.6 μm^3 cm^{-3}). These values are lower than ambient due to dilution (the chambers were partially filled with clean air) and also losses in the transfer system. Dilution was dominant and as a result, the peaks of the particle number and volume size distribution were the same as these of the ambient distributions. At t=0.4 h, we introduced HONO to produce OH in one of the chambers. The SMPS measurements suggested a graduate decrease of the number and volume of the particles due to losses to the walls for the first hour of OH exposure. However, at t=1.5 h the particle number concentration in the

perturbation chamber started increasing gradually from 2000 cm^{-3} to 4000 cm^{-3} until the end of the experiment. Our hypothesis is that this is due to nucleation and growth in the perturbation chamber.

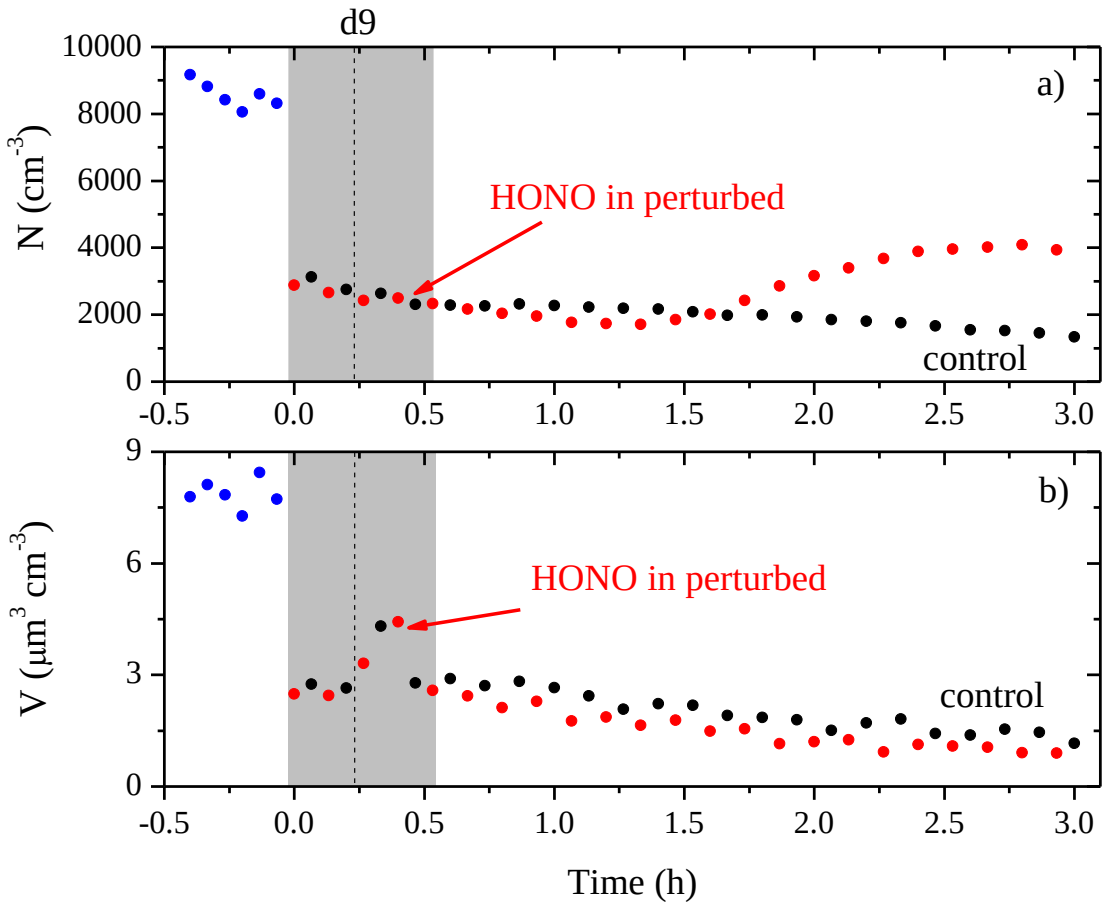

Figure A.1: The SMPS-measured **a)** aerosol number concentration evolution and **b)** aerosol volume concentration evolution during Exp. 1 for ambient (blue symbols), the perturbed chamber (red symbols) and the control chamber (black symbols). At time zero, the instruments switched from measuring ambient to the chambers. Butanol-d9 was added to both chambers at *t*=0.25 h. At *t*=0.4 h, HONO was added only to the perturbed chamber to produce OH under UV illumination. The shaded area indicates that the chambers were dark. These measurements have not been corrected for losses.

The SMPS measured particles with diameters above 15 nm or so, therefore the time delay of 1 h probably corresponds to the time required for the newly formed particles to grow to the detection limit of our instruments. This corresponds to a growth rate of around 15 nm h^{-1}. From *t*=1.5-2.5 h,

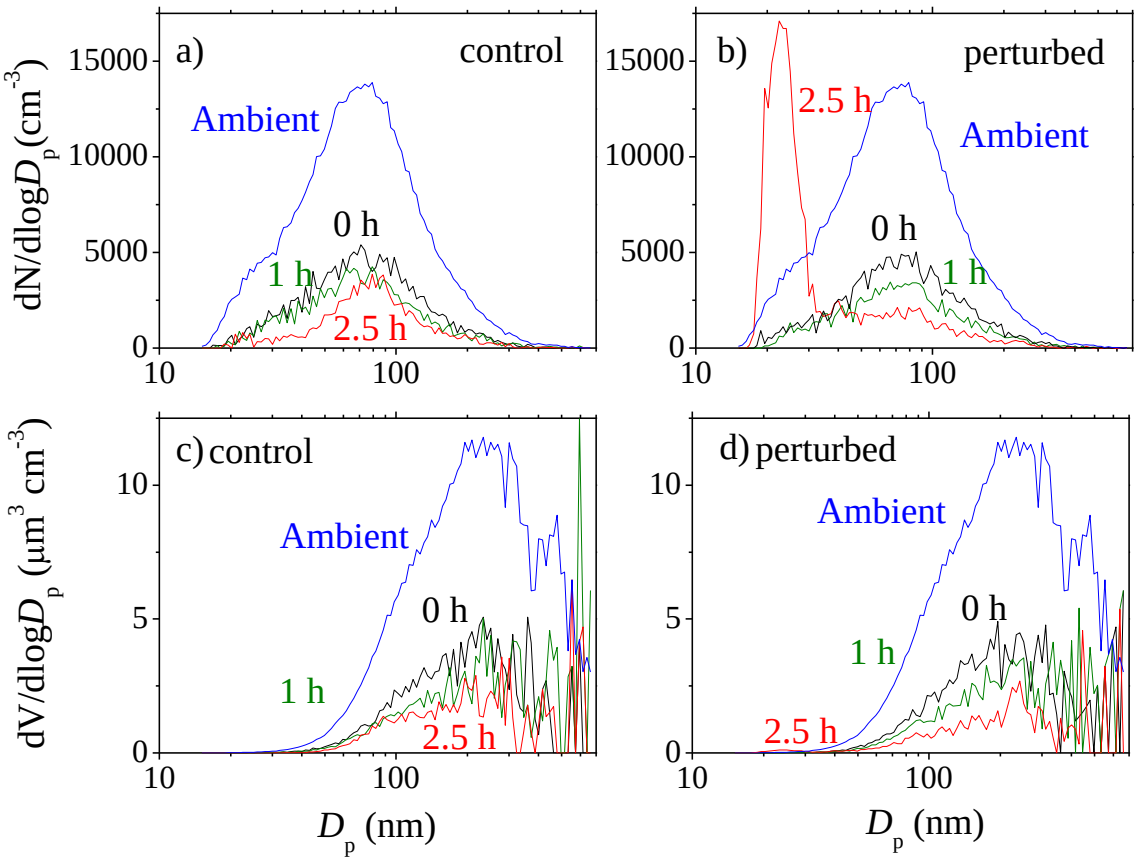

Figure A.2: The SMPS-measured aerosol number and volume size distributions for the control and the perturbed chamber during Exp. 1.

the nucleation mode peak shifted from 15 nm to 24 nm (Fig. A.3). Due to the small mass of the nucleated particles, no changes in the total particle volume were observed.

The evolution of the SMPS particle number and volume size distributions in both chambers show that the particles were getting lost to the walls during the experiment (Fig. A.2). It is not clear whether there was condensation based on these SMPS measurements that covered only part of the particle size distribution and were quite noisy for particles above 300 nm or so. The AMS

measurements can provide additional information about what happened during the aging phase in our experiment.

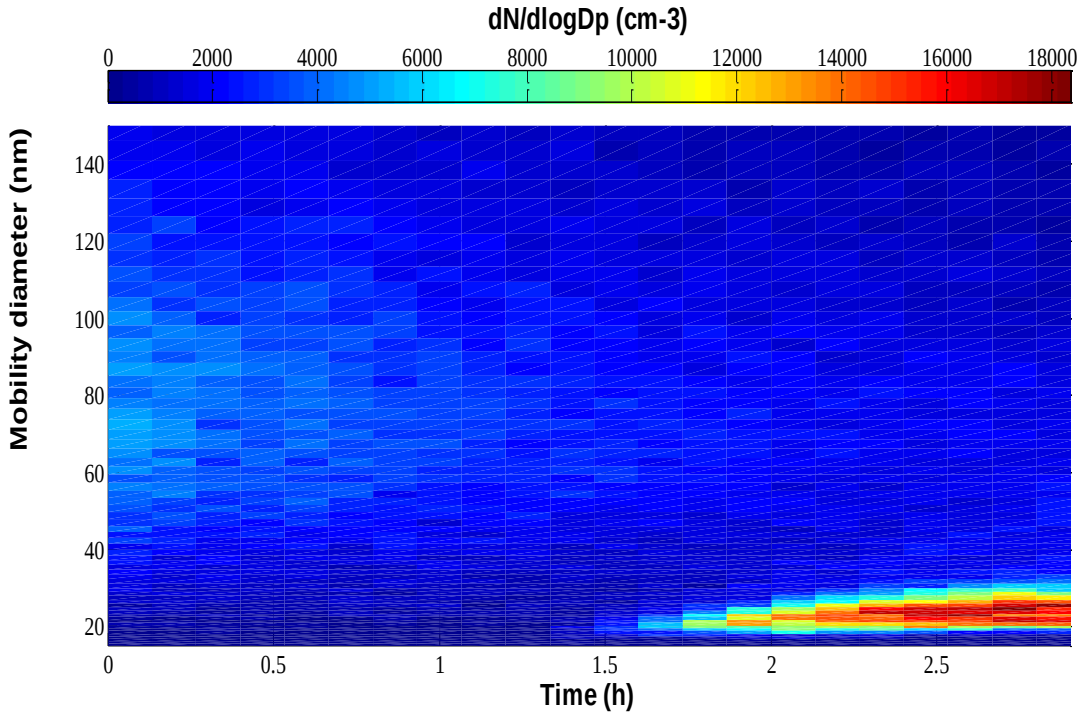

Figure A.3: Time evolution of the particle number size distribution of the aerosols in the perturbed chamber during Exp. 1. The red end of the spectrum indicates more particles while the blue fewer. Nucleation was observed at *t*=1.5 h. At the end of the experiment, the nucleation peak centered around 25 nm.

A.2.1 Ambient aerosol composition

The collection efficiency of the AMS measurements was found to be 0.8 based on the algorithm from Kostenidou et al. (2007), while the estimated OA density was 1.2 g cm^{-3}. Based on the AMS measurements, the ambient air used to fill the chambers contained 13.2 μg m^{-3} (CE=0.8) of non-refractory PM_1 with organics accounting for 63 %, sulfate 15 %, nitrate 14 % and ammonium 8 % (Fig. A.4). To estimate how much of the nitrates we observed were organonitrates (-ONO_2), we adopted the method described in Farmer et al. (2010) based on the AMS-measured

NO_x^+ ratio ($R=NO^+/NO_2^+$). The fractional contribution of the organonitrates (ONit) to total nitrates (TotNit) can be calculated as:

$$\frac{ONit}{TotNit} = [(R_{mea} - R_{cal})(1 + R_{ONit})]/[(R_{ONit} - R_{cal})(1 + R_{mea})], \quad (1)$$

where R_{mea} is the measured R during the ambient sampling and R_{cal} is the ratio of m/z 30 to m/z 46 during NH_4NO_3 calibration. R_{ONit} is the R derived from organonitrates, which in our case was the maximum R (2.10) we observed during the half-hour ambient sampling. Using an R_{mea} of 2.02 and R_{cal} of 1.33, more than 90 % of the measured nitrates were organonitrates based on this

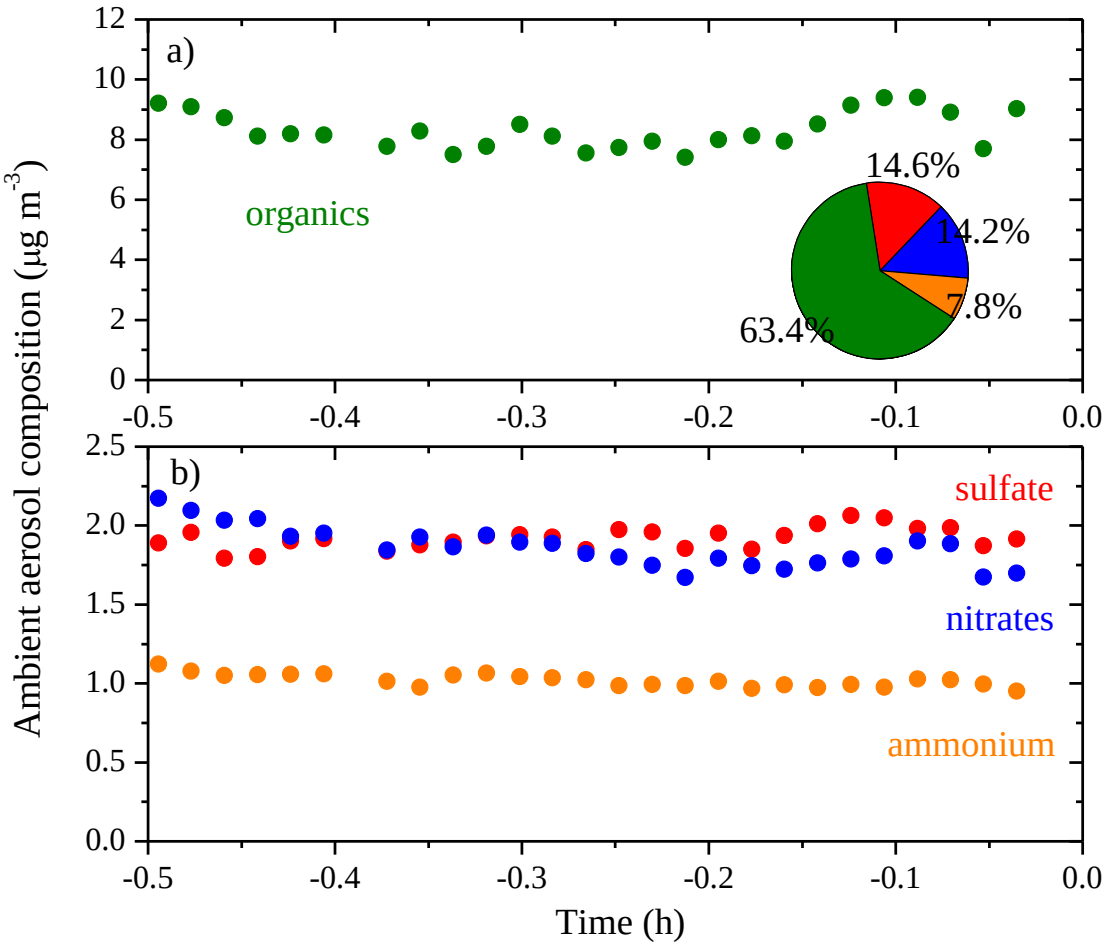

Figure A.4: The AMS-measured ambient aerosol composition during the filling process of the chambers of Exp. 1. The percentage of each aerosol component is shown in the inset pie chart.

method. The organonitrate fraction can also be estimated using an ion balance. Approximately 0.8 μg m^{-3} of ammonium is needed to fully neutralize the 2 μg m^{-3} of sulfate present in the sample. The additional 0.2 μg m^{-3} of ammonium available were probably combined with 0.7 μg m^{-3} of inorganic nitrate to form ammonium nitrate. This approach suggests that approximately 65 % of the nitrates were organonitrates. Therefore, even if both approaches provide zeroth order estimates, they do agree that the majority of the nitrates present were organonitrates.

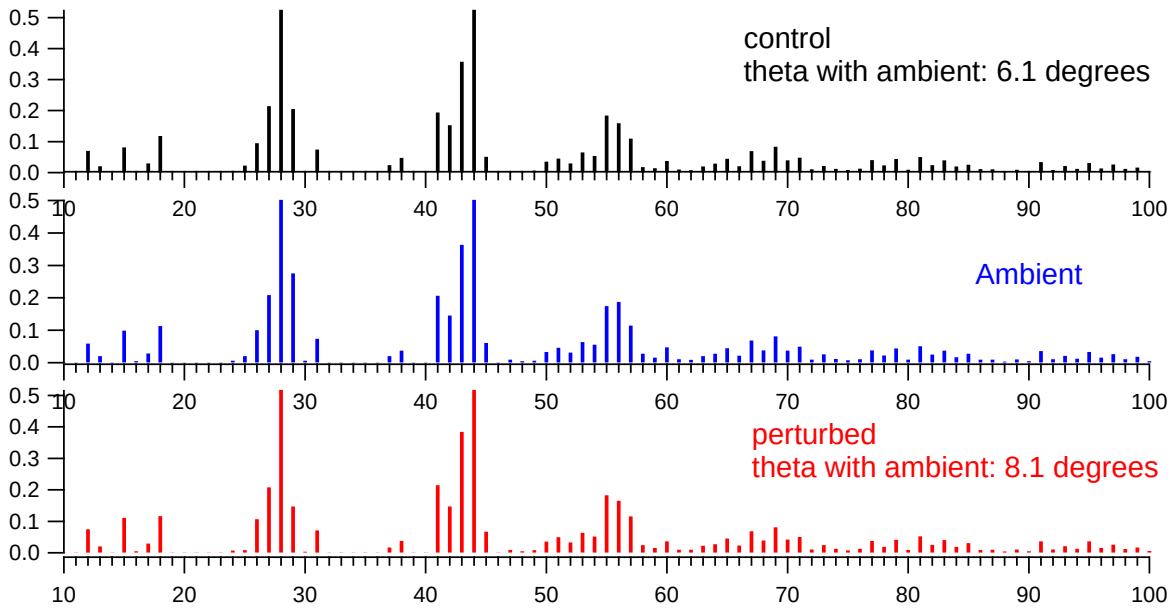

Figure A.5: The normalized AMS unit resolution mass spectra of the organics in the ambient air during the filling process of the chambers (*t*=-0.5-0 h) and those during the initial period during Exp. 1.

The potential introduction of impurities or other artifacts during the filling of the chambers can be evaluated comparing the AMS spectra of the ambient and chamber organic aerosol in the beginning of the measurements. To evaluate the similarity of the aerosol components in the ambient and in the chambers, we calculated the angle theta (Kostenidou et al., 2009) between the mass spectra vectors (Fig. A.5) of the ambient measurements and the initial measurements of the

chambers (t=0-0.3 h). θ's of 6.1 and 8.1 degrees were found, indicating that the aerosol composition inside the chambers was essentially the same as that in the ambient. This indicates that the transfer process of the ambient aerosol into the chambers did not introduce any serious artifacts.

A.2.2 Aerosol formation during aging

To quantify potential aerosol formation in the chambers due to perturbation, we corrected the AMS measurements for particle wall-losses. The measured coagulation-corrected particle wall-loss rate constants $k_c(D_p)$ were approximately constant in the 50-500 nm diameter range (Fig. A.13). We thus used a constant k_c=0.2 h^{-1} for particles of all measured sizes. An ε_V of 2.7 % was found using the method described in Wang et al. (2017) based on the corrected seed volume concentration for the seed period at the end of the perturbation experiment (Fig. A.14). The particle wall-loss corrected aerosol mass concentration for species i, C_i^{tot} was then be found by:

$$C_i^{tot} = C_i^{sus}(t) + k_c \int_0^t C_i^{sus}(t)dt, \quad (2)$$

where C_i^{sus} is the AMS-measured (CE=0.8) mass concentration for species i.

The particle wall-loss corrected aerosol mass concentration for each component in both chambers is shown in Fig. A.6. All four components of the aerosol kept decreasing gradually during the course of the experiment even after the wall correction. This decreasing trend for the control chamber too strongly suggests that the losses to the walls of the aerosol particles were higher (almost double) during the experiment than during the wall loss characterization period. This behavior requires additional work but also demonstrates the utility of the control chamber in this experimental system.

A first order analysis can be performed by using the aerosol mass concentrations in the

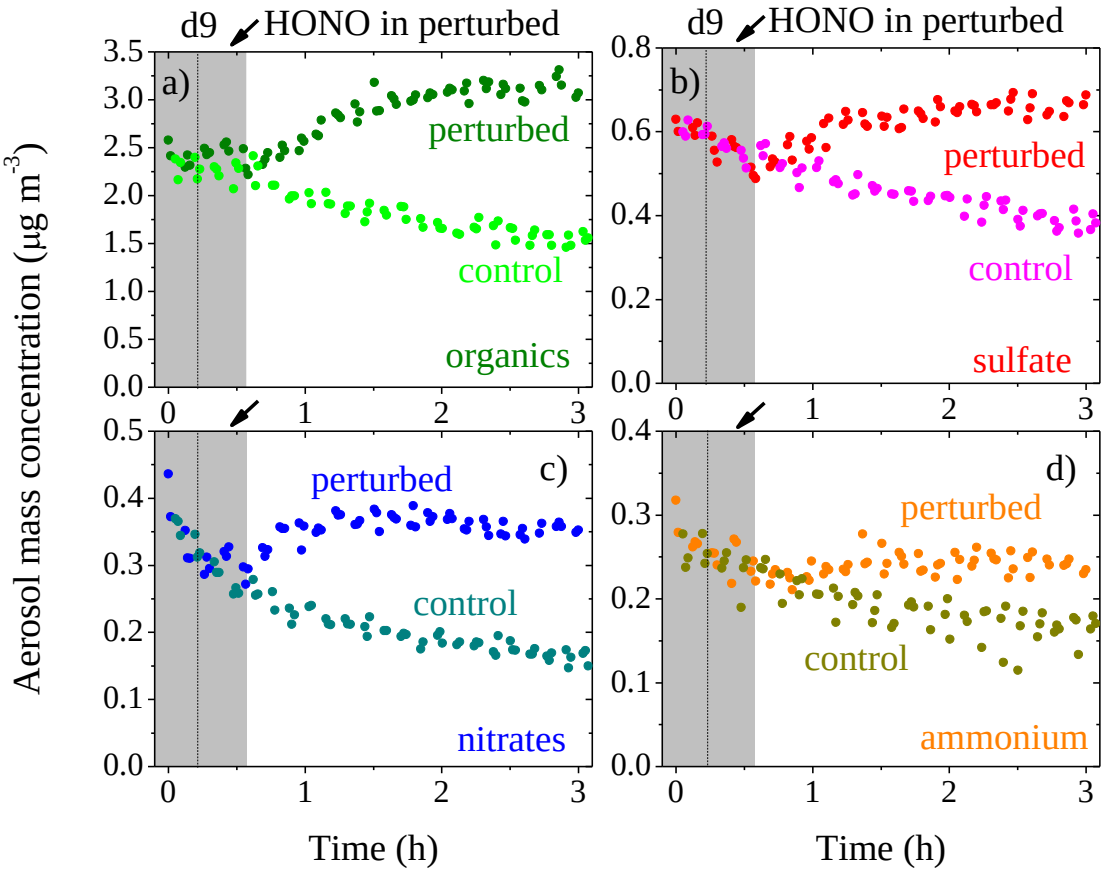

Figure A.6: The particle wall-loss corrected aerosol mass concentration (CE=0.8) for the AMS-measured **a)** organics, **b)** sulfate, **c)** nitrates and **d)** ammonium in both the perturbed and the control chamber during Exp. 1. At time zero, the instruments switched from measuring ambient to the chambers. Butanol-d9 was added to both chambers at *t*=0.25 h. At *t*=0.4 h, HONO was added only to the perturbed chamber to produce OH under UV illumination. The shaded area indicates that the chambers were dark.

control chamber as our baseline when calculating additional SOA formation in the perturbed chamber. Increases in organics and nitrates were observed in the perturbed chamber after the OH introduction. An additional 1.5 µg m^{-3} organics and 0.2 µg m^{-3} nitrates were formed in the perturbed chamber after two hours of exposure to OH. The AMS-measured NO_x^+ ratio ($R=NO^+/NO_2^+$) increased from 2.09 to 2.83 in the perturbation chamber, indicating that practically

all 0.2 μg m^{-3} of formed nitrates were organonitrates. So an additional SOA of 1.7 μg m^{-3} (including organonitrates) was formed after the OH exposure. The HONO photolysis produced NO_x levels of up to 2 ppm in the perturbed chamber. The additional formation of sulfate and ammonium in the perturbed chamber was somewhat delayed, starting at t=1 h. At the end of the experiment, an additional 0.2 μg m^{-3} sulfate and 0.06 μg m^{-3} ammonium were formed. The molar ratio of the additional NH_4^+ and SO_4^{2-} was 1.6, suggesting that the newly formed NH_4^+ and SO_4^{2-} were a mixture of ammonium bisulfate and ammonium sulfate. This is thermodynamically consistent with the lack of formation of ammonium nitrate.

The OH concentration in the perturbed chamber was 1.8×10^7 molecule cm^{-3} an hour after the OH introduction based on the decay of the butanonal-d9 (Fig. A.8), and then dropped to 5×10^6 molecule cm^{-3} afterwards. This gives an OH exposure of 12 h ambient daytime equivalent (assuming 2×10^6 molecule cm^{-3} for ambient conditions). The OH concentration in the control chamber was rather low, at 1.8×10^5 molecule cm^{-3}.

A.2.3 Oxygen to Carbon Ratio

The oxygen to carbon ratio of the organic aerosol during Exp. 1 is shown in Fig. A.7. The O:C for the ambient OA was around 0.5, indicating that the ambient OA was moderately oxygenated. Before UV illumination, the O:C of the OA in both the perturbed and the control chambers was also around 0.5, consistent with the fact that the OA in the chambers was the same as the ambient OA. After the OH introduction, the O:C of the OA in the control chamber remained practically the same at 0.5, while that in the perturbed chamber gradually decreased to 0.3 until the end of the experiment. An O:C of 0.3 indicates that the additional SOA formed in the perturbed chamber had much lower O:C than the ambient OA.

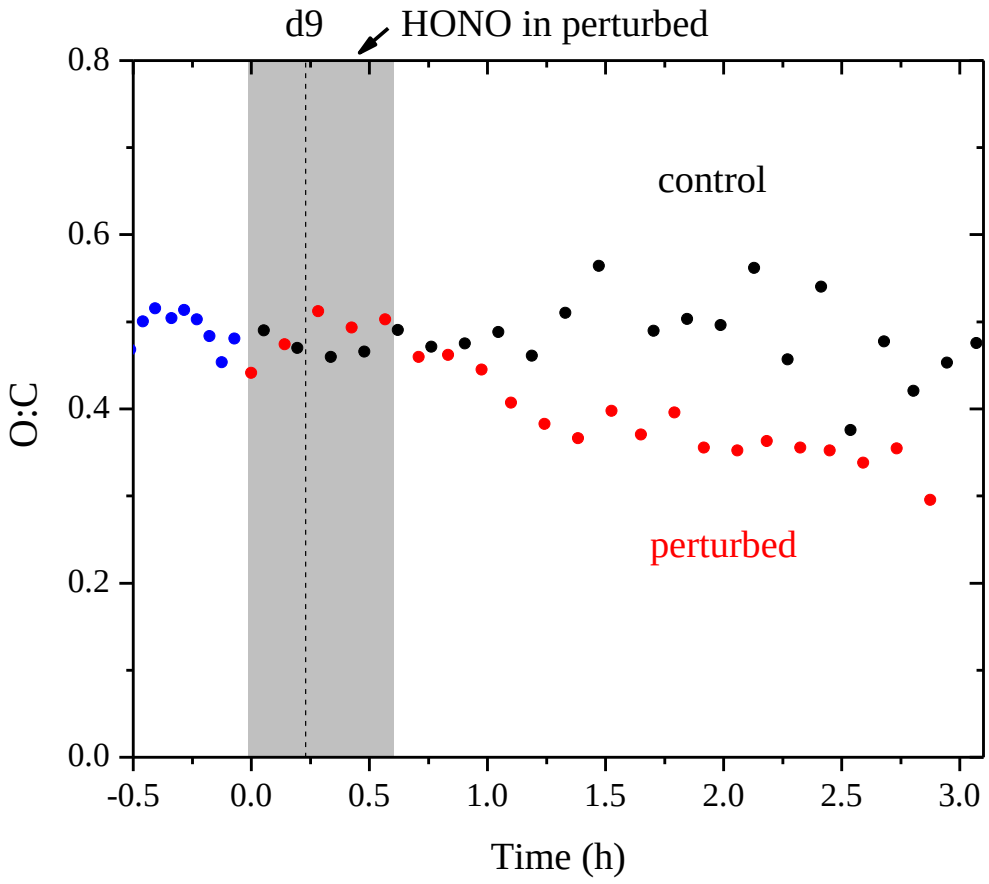

Figure A.7: The atomic oxygen to carbon ratio (O:C) evolution of the AMS-measured organics during Exp. 1. At time zero, the instruments switched from measuring ambient (blue symbols) to the chambers. Butanol-d9 was added to both chambers at *t*=0.25 h. At *t*=0.4 h, HONO was added only to the perturbed chamber to produce OH under UV illumination. The shaded area indicates that the chambers were dark.

The PTR-MS measurements were used to identify potential VOC precursors and products during the aging phase. We set the PTR-MS to measure aromatics including benzene (*m*/*z* 79), toluene (*m*/*z* 93), xylene (*m*/*z* 107), C9 aromatics (*m*/*z* 121), C10 aromatics (*m*/*z* 137) and biogenics including isoprene (*m*/*z* 69) and monoterpene (*m*/*z* 81, *m*/*z* 137). The concentrations of these monitored VOCs remained less than 1 ppb during the course of the experiment. We observed high signal to noise ratio and no evident changes in their concentration. We postulate that these

precursors were probably below the detection limit if they existed in the ambient air. During the OH oxidation, an additional 2.5 ppb *m/z* 59 (acetone) and 5 ppb *m/z* 61 (acetic acid) were formed in the perturbed chamber (Fig. A.8). On the contrary the *m/z* 59 and *m/z* 61 remained constant in the control chamber. This was probably caused by low level of OH (1.8×10^5 molecule cm^{-3}) in the control chamber as compared to that (1.8×10^7 molecule cm^{-3}) in the perturbed chamber.

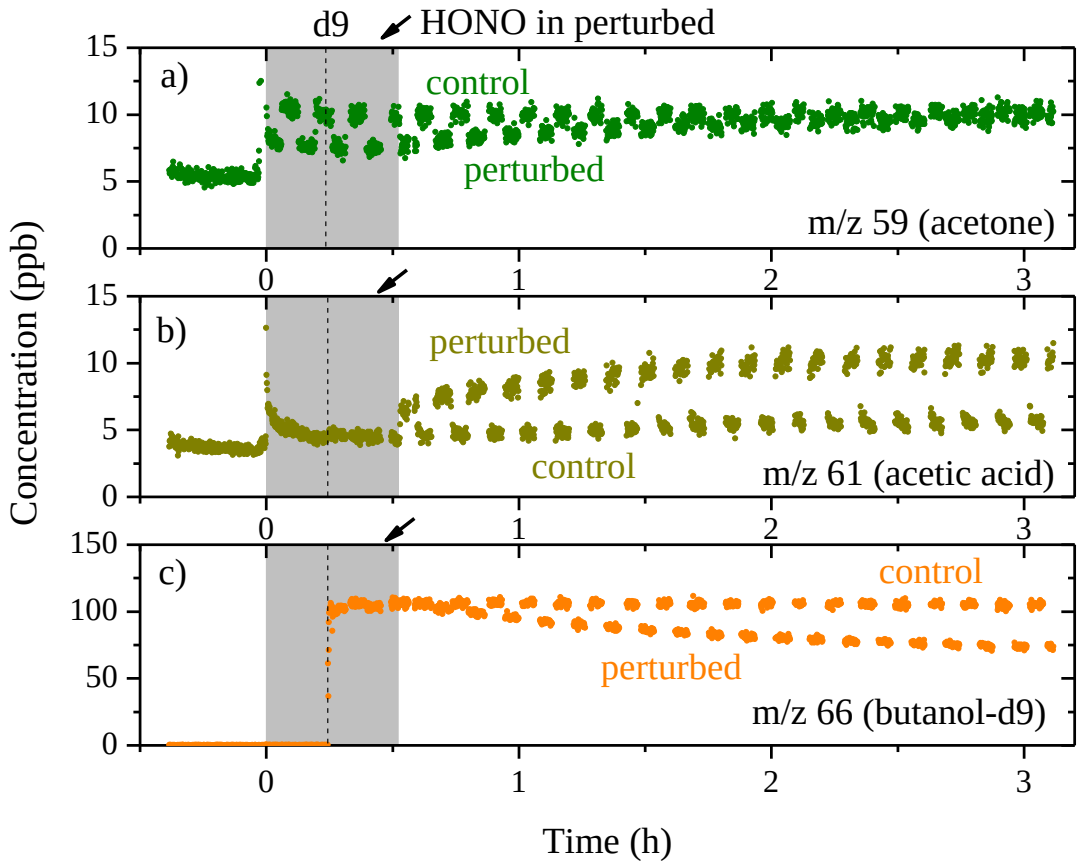

Figure A.8: The PTR-MS measured **a)** m/z 59, **b)** m/z 61, and **c)** m/z 66 concentration time series during Exp. 1. At time zero, the instruments switched from measuring ambient to the chambers. Butanol-d9 was added to both chambers at *t*=0.25 h. At *t*=0.4 h, HONO was added only to the perturbed chamber to produce OH under UV illumination. The shaded area indicates that the chambers were dark.

A.2.4 PMF analysis

PMF analysis of the AMS spectra identified two organic factors in the perturbed chamber: a more-oxygenated (M-OOA) and a less-oxygenated (L-OOA) factor. The M-OOA has an O:C of 0.55 and a pronounced f_{44} of 0.12, indicating moderately aged particles (Fig. A.9). Its time series shows that the M-OOA corresponded to the ambient OA, since it accounted for all of the OA initially in the perturbed chamber (Fig. A.10). During the course of the experiment, the M-OOA

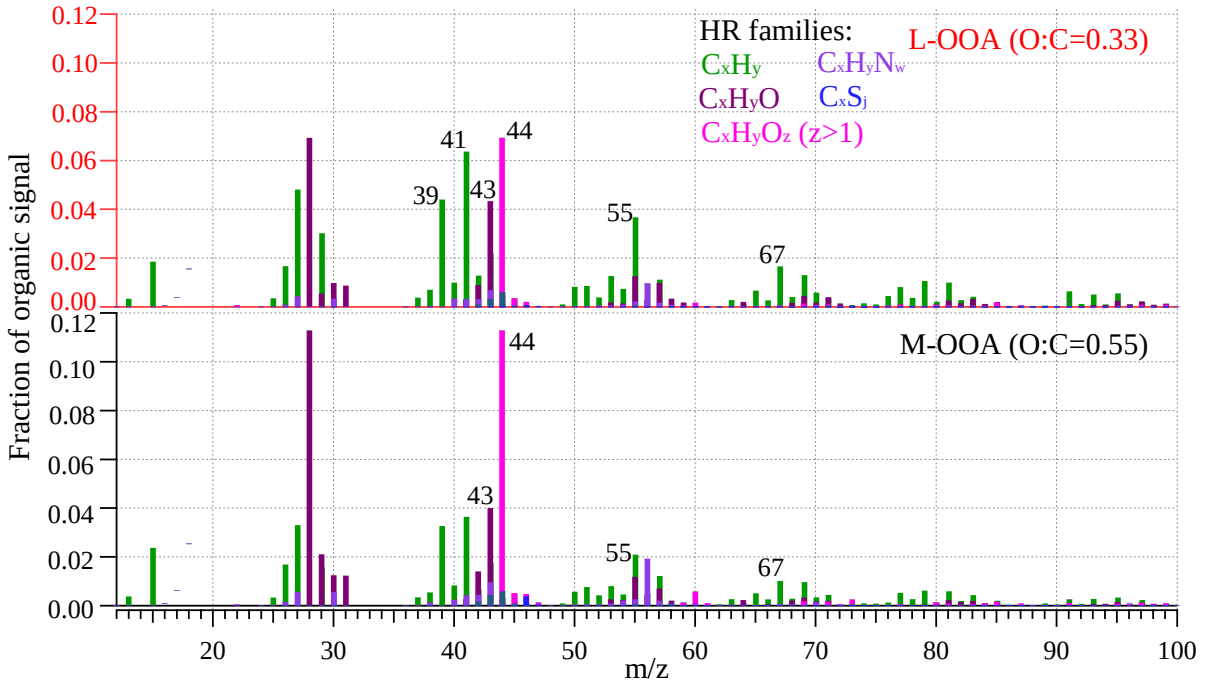

Figure A.9: High-resolution AMS mass spectra for the two PMF factors found in the perturbed chamber during Exp. 1.

gradually decreased over time due to wall loss. The L-OOA has an O:C of 0.33 and an f_{44} of 0.08. Based on its time series, the L-OOA was initially close to zero and was produced upon OH introduction in the perturbed chamber.

As expected, PMF identified only one organic factor in the reference chamber with an O:C of 0.5. The mass spectra of this factor is identical to those of the M-OOA in the perturbed chamber with an angle theta of only 3.6 degrees. This is essentially the same factor as the M-OOA. Its time series in Fig. A.10 shows that this factor in the reference chamber corresponds to the ambient OA, decreasing over time due to wall loss.

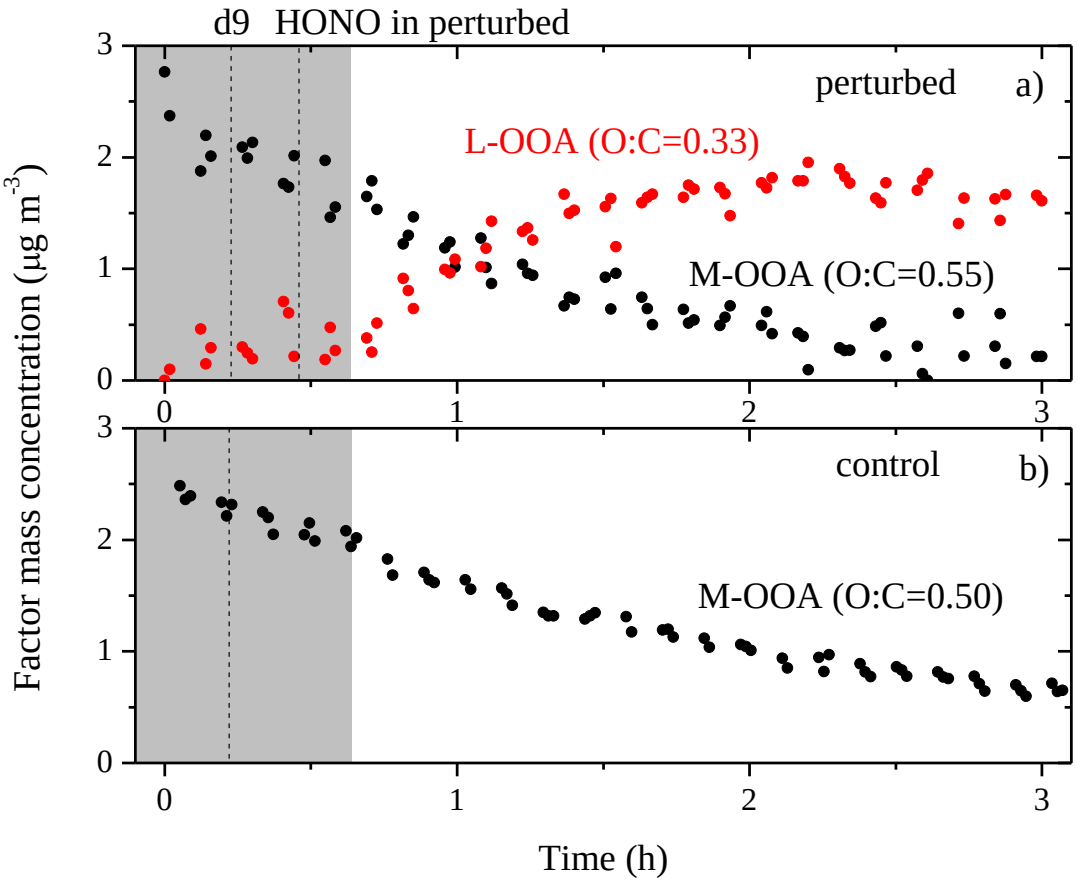

Figure A.10: Time series of **a)** the two factors in the perturbed chamber and **b)** the one factor in the control chamber based on PMF analysis during Exp. 1. At time zero, the instruments switched from measuring ambient to the chambers. Butanol-d9 was added to both chambers at *t*=0.25 h. At *t*=0.4 h, HONO was added only to the perturbed chamber to produce OH under UV illumination. The shaded area indicates that the chambers were dark.

We compared the L-OOA and M-OOA mass spectra to those of OOA factors identified in

previous ambient and laboratory studies (Table A.1). The M-OOA factor corresponding to the

Table A.1: Correlations between PMF factors from this work and PMF OOA factors from selected studies using the angle theta.

SV-OOA/ LV-OOA	**Angle theta** (degree)	
	L-OOA	**M-OOA**
SV-OOA, Pittsburgh[a]	16.5	17.7
SV-OOA, Barcelona[b]	17.0	21.8
SV-OOA, Riverside[c]	17.6	31.2
LV-OOA, Fresno[d]	18.1	16.1
SV-OOA, New York City[e]	19.5	21.6
SV-OOA, Mexico City[f]	19.6	14.8
SV-OOA, Paris[g]	23.9	33.2
SV-OOA, Athens, summer[h]	28.6	13.3
LV-OOA, Paris, summer[g]	29.8	14.3
SV-OOA, Patras, summer[h]	31.5	15.4
LV-OOA, New York City[e]	33.1	16.1
LV-OOA, Pittsburgh[a]	35.4	17.8
LV-OOA Athens, summer[h]	36.4	19.1
LV-OOA, Barcelona[b]	36.7	19.6
LV-OOA, Mexico City[f]	37.0	22.3
OOA, Paris, winter[i]	42.0	25.2
LV-OOA, Patras, summer[h]	42.0	24.3
OOA_II, Pittsburgh[j]	43.3	46.3
OOA_I, Pittsburgh[j]	45.0	44.4
OOA, Pittsburgh[k]	45.2	44.5
LV-OOA, Riverside[c]	49.6	18.0

[a] Gu et al. (2018), [b] Mohr et al. (2012), [c] Docherty et al. (2011), [d] Ge et al. (2012 a, b), [e] Sun et al. (2011), [f] Aiken et al. (2009), [g] Crippa et al. (2013a), [h] Kostenidou et al. (2015), [i] Crippa et al. (2013 b), [j] Ulbrich et al. (2009), [k] Zhang et al. (2005).

ambient OA had moderate similarity (theta of 13.3-19.6 degrees) with 4 SV-OOA factors and 7 LV-OOA factors. This is probably due to the fact that the ambient OA includes organic components with a distribution of oxygen contents that could not be further separated based on the limited set of data (of the order of one hour) collected in this study. On the other hand, the L-OOA identified in this work had also moderate similarity the (theta angle of 16.5-19.6) with five SV-

OOA factors and one LV-OOA factor. This result indicates that the L-OOA factor is more SV-OOA like.

Table A.2: Correlations between PMF factors from this work and PMF COA factors from selected studies using the angle theta.

COA	**Angle theta** (degree)	
	L-OOA	**M-OOA**
Athens, summer[a]	7.3	23.7
Patras, summer[a]	8.7	26.5
New York City[b]	16.5	34
Patras, winter[c]	25	42.2
Paris[d]	32.4	48.3
Pittsburgh[e]	32.9	51.1
Fresno[f]	34.7	52

[a] Kostenidou et al. (2015), [b] Sun et al. (2011), [c] Kaltsonoudis et al. (2017), [d] Crippa et al. (2013a), [e] Gu et al. (2018), [f] Ge et al. (2012 a, b).

The L-OOA AMS spectrum was quite similar (theta angle of 7-9 degrees) with the aged cooking OA spectra identified in Greek cities by Kostenidou et al. (2015) and had some similarity (theta of 16.5 degrees) with processed COA from NYC (Table A.2). Considering the fact that the chambers were filled right after lunch time (3 pm) on the CMU campus, it is likely that some of the COA components were present in the chambers initially and formed part of the additional OA observed after the OH introduction. It is also possible that the other organic intermediate volatility compounds were present that after oxidation produced SOA similar to the aged COA.

A.3 Summary and future work

Preliminary results from the dual-chamber perturbation experiment show that the ambient air components from a university campus (CMU) in Pittsburgh has the potential to form additional SOA upon OH oxidation.

Upon OH oxidation of the ambient air components in the perturbed chamber, nucleation of ~2000 cm^{-3} particles was observed with the nucleation mode of the particle number size distribution centered at ~25 nm by the end of the experiment. We estimated a growth rate of 15 nm h^{-1} based on the SMPS measurements. From the AMS measurements, 1.7 μg m^{-3} additional SOA (including organonitrates) was formed after an OH exposure equivalent to 12 h in the ambient. An additional 0.2 μg m^{-3} sulfate and 0.06 μg m^{-3} ammonium formed, probably in the form of a mixture of ammonium bisulfate and ammonium sulfate. No chemistry was observed in the control chamber due to the low level of OH.

We identified two OOA factors from the perturbed chamber based on the PMF analysis of the AMS-measured high-resolution organic mass spectra. The M-OOA factor originated from the ambient OA and was moderately oxidized. Its mass spectra mimic those of the SV-OOA and LV-OOA. The L-OOA factor formed upon the OH oxidation and had a lower O:C of 0.33. Its mass spectra mimic those of the aged COA.

Due to the limitation of the precursor IVOC measurements, we were not able to determine the source of the additional SOA formation. For future work, measurements of IVOCs should be incorporated. Particle sizers that can measure from 1 nm to 2.5 μm are also needed in order to study nucleation or bigger particles that exist in ambient air. A SO_2 monitor should also be used.

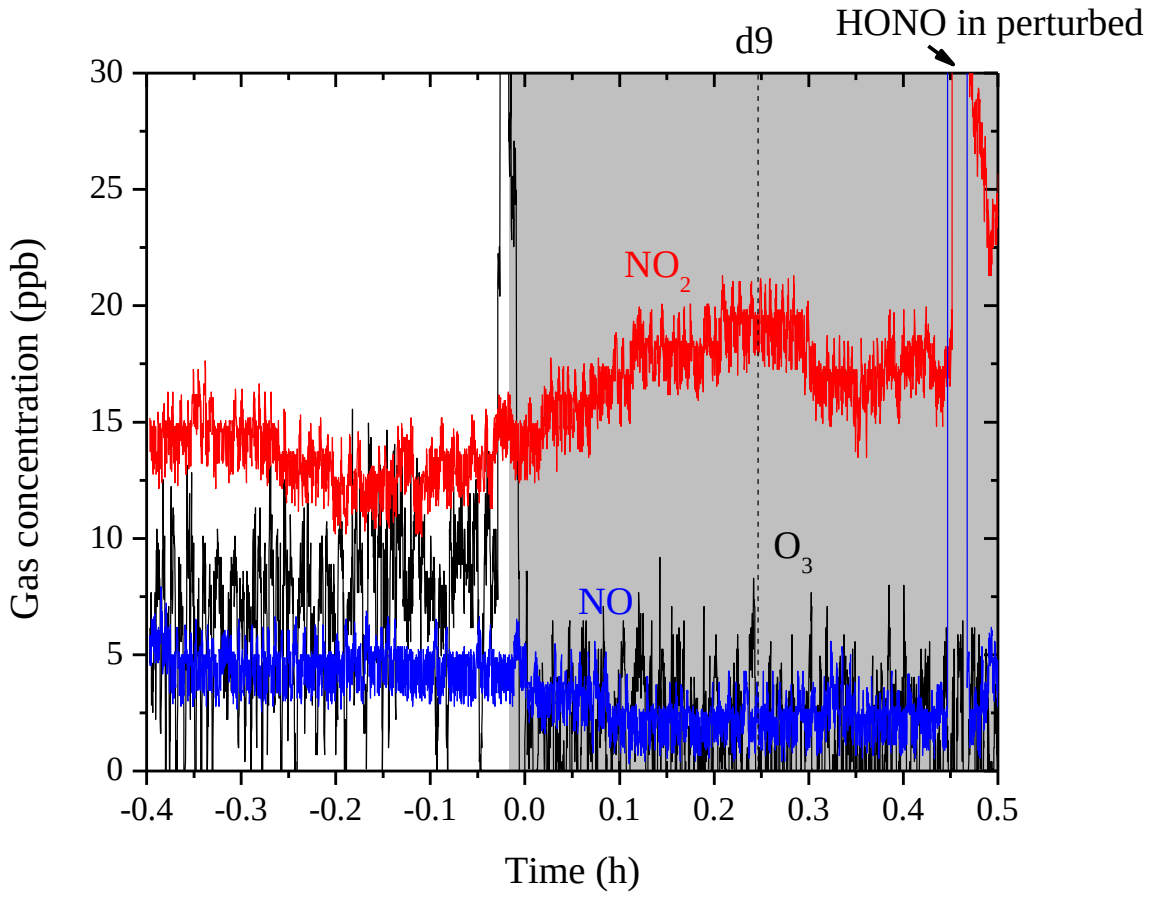

Figure A.11: The gas concentrations of the ambient conditions during the filling process of the chambers (*t*=-0.5-0 h) and initial chamber conditions (*t*=0-0.5 h). At time zero, the instruments switched from measuring ambient to the chambers. Butanol-d9 was added to both chambers at *t*=0.25 h. At *t*=0.4 h, HONO was added only to the perturbed chamber to produce OH under UV illumination. The shaded area indicates that the chambers were dark.

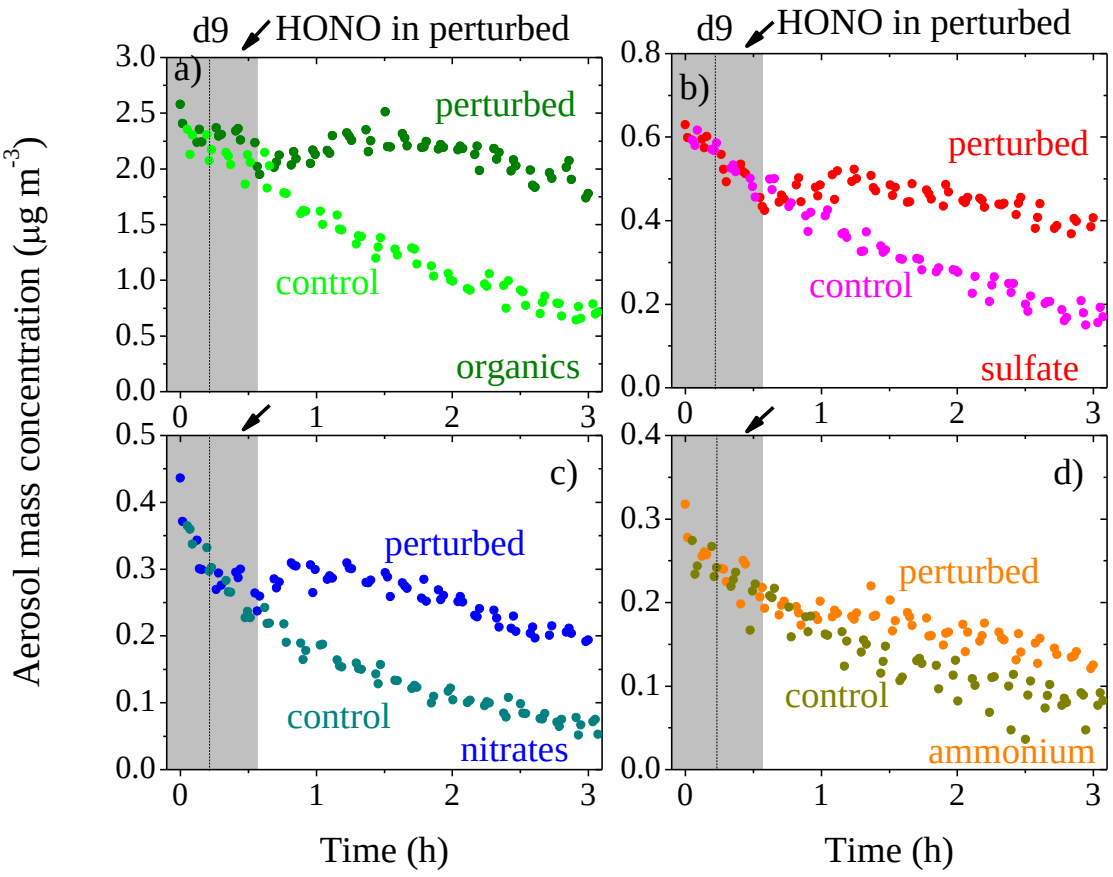

Figure A.12: The AMS-measured (without correction for losses to the walls) aerosol mass concentration for **a)** organics, **b)** sulfate, **c)** nitrates and **d)** ammonium in both the perturbed and the control chamber during Exp. 1. At time zero, the instruments switched from measuring ambient to the chambers. Butanol-d9 was added to both chambers at t=0.25 h. At t=0.4 h, HONO was added only to the perturbed chamber to produce OH under UV illumination. The shaded area indicates that the chambers were dark.

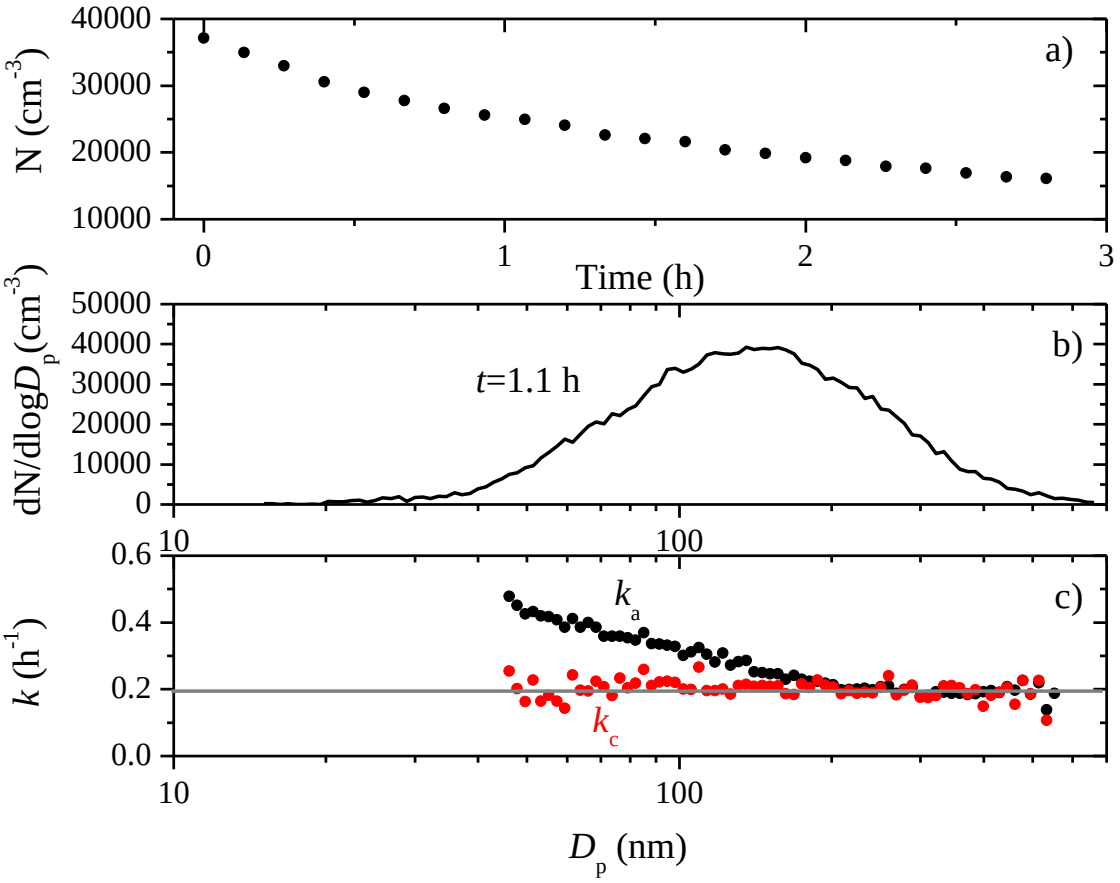

Figure A. 13: The SMPS-measured **a)** aerosol number concentration evolution, **b)** aerosol volume size distribution at t=1.1 h, and **c)** the size-dependent particle wall-loss rate constants with the apparent ones in black the coagulation-corrected ones in red and the fitted ones as the grey line during the seed wall loss period after Exp. 1.

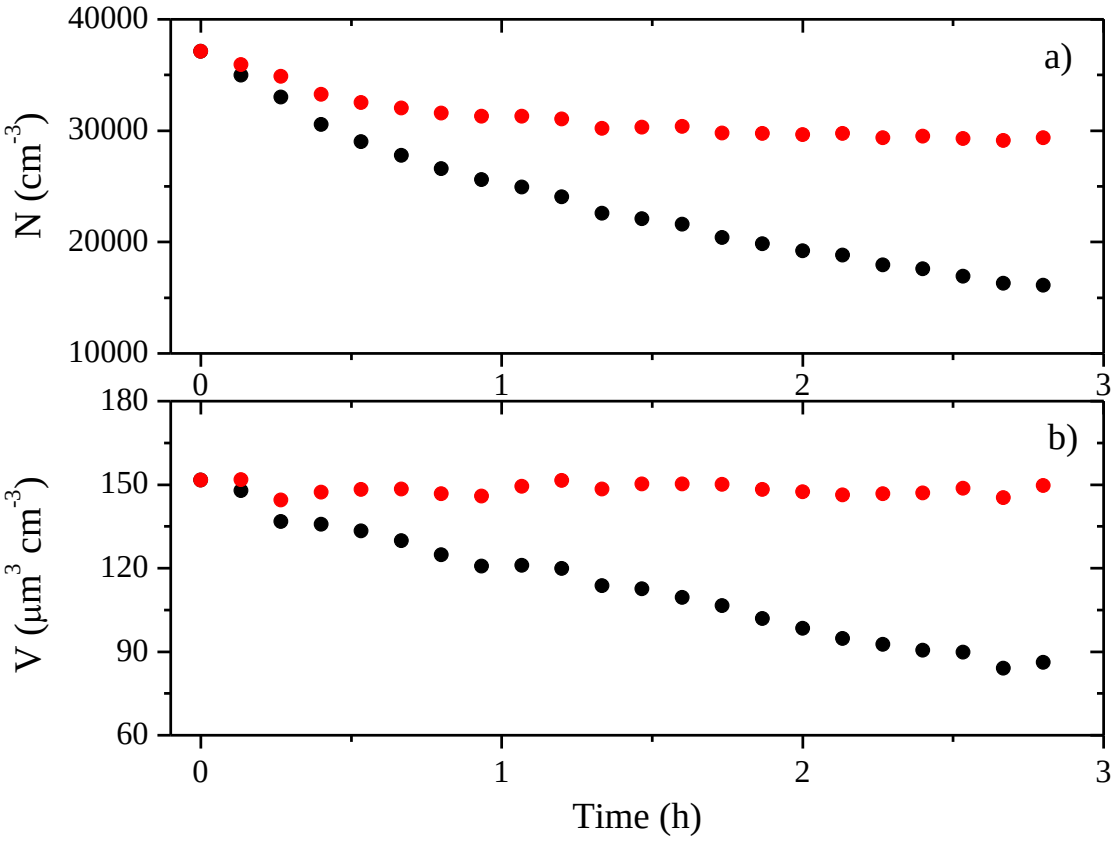

Figure A.14: The SMPS-measured (black symbols) and the particle-loss corrected (red symbols) **a)** number and **b)** volume concentration using a wall-loss rate constant of 0.2 h^{-1} for particles of all sizes during the seed wall loss period after Exp. 1.

A.4 References

Aiken, A. C., Salcedo, D., Cubison, M. J., Huffman, J. A., DeCarlo, P. F., Ulbrich, I. M., Docherty, K. S., Sueper, D., Kimmel, J. R., Worsnop, D. R., Trimborn, A., Northway, M., Stone, E. A., Schauer, J. J., Volkamer, R. M., Fortner, E., de Foy, B., Wang, J., Laskin, A., Shutthanandan, V., Zheng, J., Zhang, R., Gaffney, J., Marley, N. A., Paredes-Miranda, G., Arnott, W. P., Molina, L. T., Sosa, G., and Jimenez, J. L.: Mexico City aerosol analysis during MILAGRO using high resolution aerosol mass spectrometry at the urban supersite (T0) – Part 1: Fine particle composition and organic source apportionment, Atmos. Chem. Phys., 9, 6633–6653, 2009.

Crippa M., El Haddad I., Slowik J., G., DeCarlo P. F., Mohr, C., Heringa, M., F, Chirico, R., Marchand, N., Sciare, J., Urs, B., and Prévôt, A. S. H.: Identification of marine and

continental aerosol sources in Paris using high resolution aerosol mass spectrometry, J. Geophys. Res, 118, 1950-1963, 2013a.

Crippa, M., DeCarlo, P. F., Slowik, J. G., Mohr, C., Heringa, M. F., Chirico, R., Poulain, L., Freutel, F., Sciare, J., Cozic, J., Di Marco, C. F., Elsasser, M., Nicolas, J. B., Marchand, N., Abidi, E., Wiedensohler, A., Drewnick, F., Schneider, J., Borrmann, S., Nemitz, E., Zimmermann, R., Jaffrezo, J.-L., Prévôt, A. S. H., and Baltensperger, U.: Wintertime aerosol chemical composition and source apportionment of the organic fraction in the metropolitan area of Paris, Atmos. Chem. Phys., 13, 961–981, 2013b.

Docherty, K. S., Aiken, A. C., Huffman, J. A., Ulbrich, I. M., DeCarlo, P. F., Sueper, D., Worsnop, D. R., Snyder, D. C., Peltier, R. E., Weber, R. J., Grover, B. D., Eatough, D. J., Williams, B. J., Goldstein, A. H., Ziemann, P. J., and Jimenez, J. L.: The 2005 Study of Organic Aerosols at Riverside (SOAR-1): instrumental intercomparisons and fine particle composition, Atmos. Chem. Phys., 11, 12387–12420, 2011.

Farmer, D. K., Matsunaga, A., Docherty, K. S., Surratt, J. D., Seinfeld, J. H., Ziemann, P. J., and Jimenez, J. L.: Response of an aerosol mass spectrometer to organonitrates and organosulfates, and implications for atmospheric chemistry, P. Natl. Acad. Sci. USA, 107, 6670–6675, 2010.

Ge, X., Setyan, A., Sun, Y., and Zhang, Q.: Primary and secondary organic aerosols in Fresno, California during wintertime: Results from high resolution aerosol mass spectrometry, J. Geophys. Res., 117, D19301, 2012a.

Ge, X., Zhang, Q., Sun, Y., Ruehl, C. R., and Setyan, A.: Effect of aqueous-phase processing on aerosol chemistry and size distribution in Fresno, California, during wintertime, Environ. Chem., 9, 221–235, 2012b.

Gu, P., Li, Z., Ye, Q., Robinson, E., Shi, J., Shah, R., Zimmerman, N., Apte, J., Robinson, A., and Presto, A.: Investigating spatial variation of PM1 concentration and source impact in a metropolitan area, in preparation.

Kaltsonoudis, C., Louvaris, E., Florou, K., Kostenidou, E., Wang, N., Liangou, A., Tsiligiannis, E., Jorga, S., and Pandis S. N.: A new portable dual smog chamber facility with UV lights for field studies, Atmos. Meas. Tech., in preparation.

Kaltsonoudis, C., Kostenidou, E., Louvaris, E., Psichoudaki, M., Tsiligiannis, E., Florou, K., Liangou, A., and Pandis, S. N.: Characterization of fresh and aged organic aerosol emissions from meat charbroiling, Atmos. Chem. Phys., 17, 7143-7155, 2017.

Kostenidou E., Pathak R. K., and Pandis S. N.: An Algorithm for the calculation of secondary organic aerosol density combining AMS and SMPS data, Aerosol Science and Technology, 41, 1002–1010, 2007.

Kostenidou, E., Lee, B. H., Engelhart, G. J., Pierce, J. R., and Pandis, S. N.: Mass spectra deconvolution of low, medium, and high volatility biogenic secondary organic aerosol, Environ. Sci. Technol., 43, 4884–4889, 2009.

Mohr, C., DeCarlo, P. F., Heringa, M. F., Chirico, R., Slowik, J. G., Richter, R., Reche, C., Alastuey, A., Querol, X., Seco, R., Peñuelas, J., Jiménez, J. L., Crippa, M., Zimmermann, R., Baltensperger, U., and Prévôt, A. S. H.: Identification and quantification of organic aerosol from cooking and other sources in Barcelona using aerosol mass spectrometer data, Atmos. Chem. Phys., 12, 1649–1665, 2012.

Sun, Y.-L., Zhang, Q., Schwab, J. J., Demerjian, K. L., Chen, W. N., Bae, M.-S., Hung, H.-M., Hogrefe, O., Frank, B., Rattigan, O. V., and Lin, Y.-C.: Characterization of the sources and processes of organic and inorganic aerosols in New York city with a high-resolution time-of-flight aerosol mass spectrometer, Atmos. Chem. Phys., 11, 1581–1602, 2011.

Ulbrich, I. M., Canagaratna, M. R., Zhang, Q.,Worsnop, D. R., and Jimenez, J. L.: Interpretation of organic components from Positive Matrix Factorization of aerosol mass spectrometric data, Atmos. Chem. Phys., 9, 2891–2918, 2009.

Wang, N., Kostenidou, E., Donahue, N. M., and Pandis, S. N.: Multi-generation chemical aging of α-pinene ozonolysis products by reactions with OH, Atmos. Chem. Phys. Discuss., 10.5194/acp-2017-746, 2017.

Zhang, Q., Alfarra, M. R., Wornsop, D. R., Allan, J. D., Coe, H., Canagaratna, M., and Jimenez, J. L.: Deconvolution and quantification of hydrocarbon-like and oxygenated organic aerosols based on aerosol mass spectrometry, Environ. Sci. Technol., 39, 4938–4952, 2005.

Zhang, Q., Jimenez, J. L., Canagaratna, M. R., Allan, J. D., Coe, H., Ulbrich, I., Alfarra, M. R., Takami, A., Middlebrook, A. M., Sun, Y. L., Dzepina, K., Dunlea, E., Docherty, K., DeCarlo, P. F., Salcedo, D., Onasch, T., Jayne, J. T., Miyoshi, T., Shimono, A., Hatakeyama, S., Takegawa, N., Kondo, Y., Schneider, J., Drewnick, F., Borrmann, S., Weimer, S., Demerjian, K., Williams, P., Bower, K., Bahreini, R., Cottrell, L., Griffin, R. J., Rautiainen, J., Sun, J. Y., Zhang, Y. M., and Worsnop, D. R.: Ubiquity and dominance of oxygenated species in organic aerosols in anthropogenically-influenced Northern Hemisphere midlatitudes, Geophys. Res. Lett., 34, L13801, 2007.

Appendix B
Multi-generation chemical aging of α-pinene ozonolysis products by reactions with OH

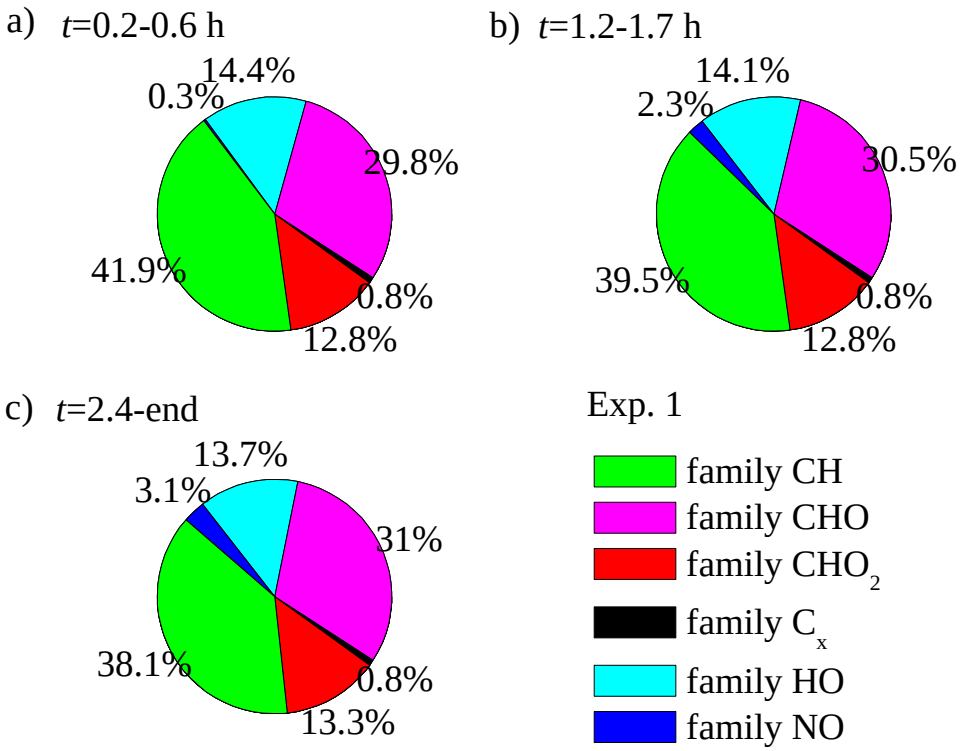

Figure B.1: The SOA composition at the end of the corresponding stages of Exp. 1: **a)** α-pinene ozonolysis; **b)** first OH aging period; **c)** second OH aging period based on the high-resolution family analysis of AMS measurements. The periods of data used are also listed.

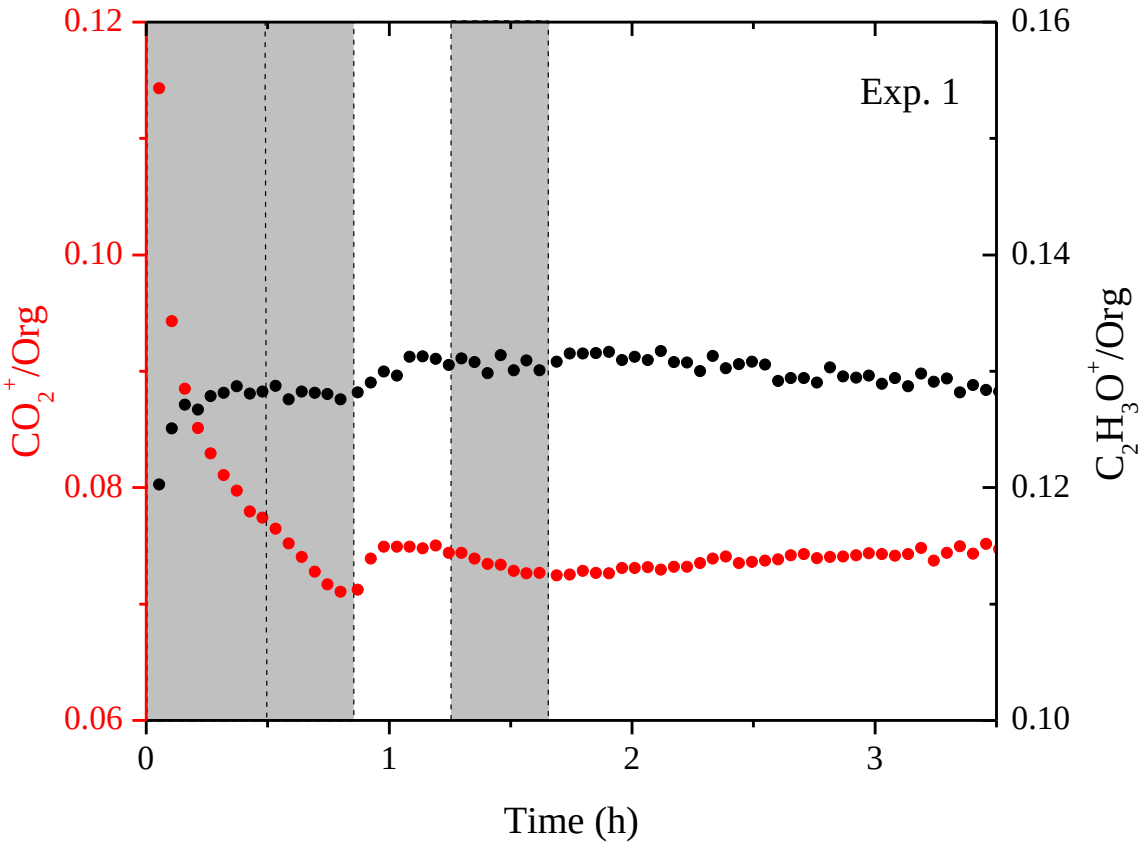

Figure B.2: The **a)** CO_2^+/Org (f_{44}) (red symbols, left axis) and the **b)** $C_2H_3O^+$/Org (f_{43}) (black symbols, right axis) during Exp. 1 based on the high resolution analysis of AMS measurements. The shaded areas indicate that the chamber was dark. The dashed lines mark the beginning and the end of the two HONO injections.

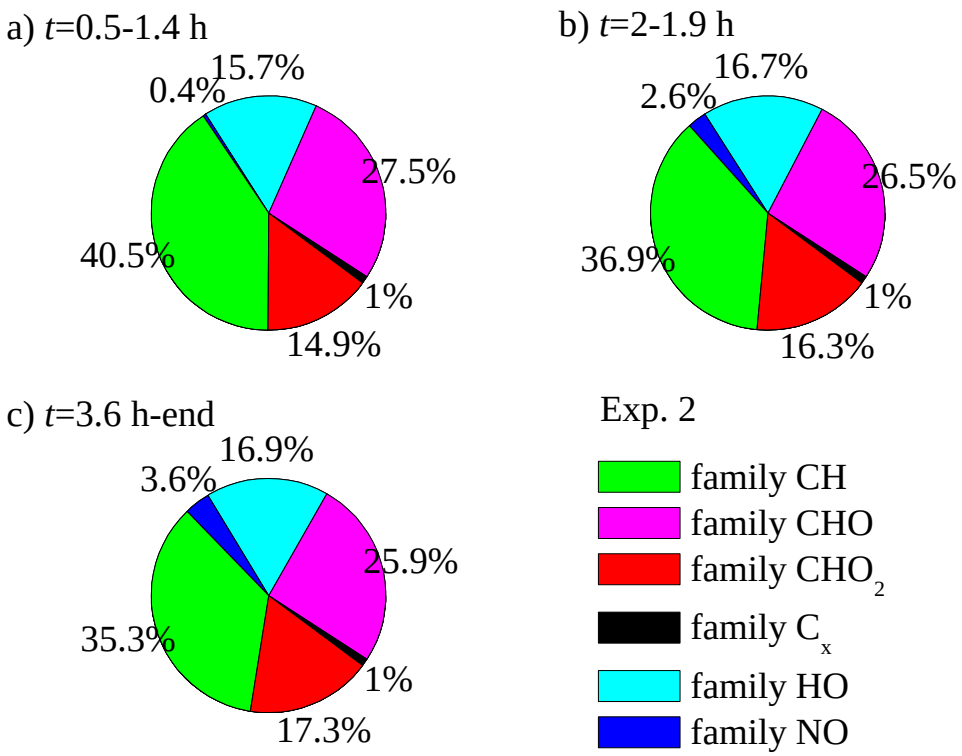

Figure B.3: The SOA composition at the end of the corresponding stages of Exp. 2: **a)** α-pinene ozonolysis; **b)** first OH aging period; **c)** second OH aging period based on the high-resolution family analysis of AMS measurements. The periods of data used are also listed.

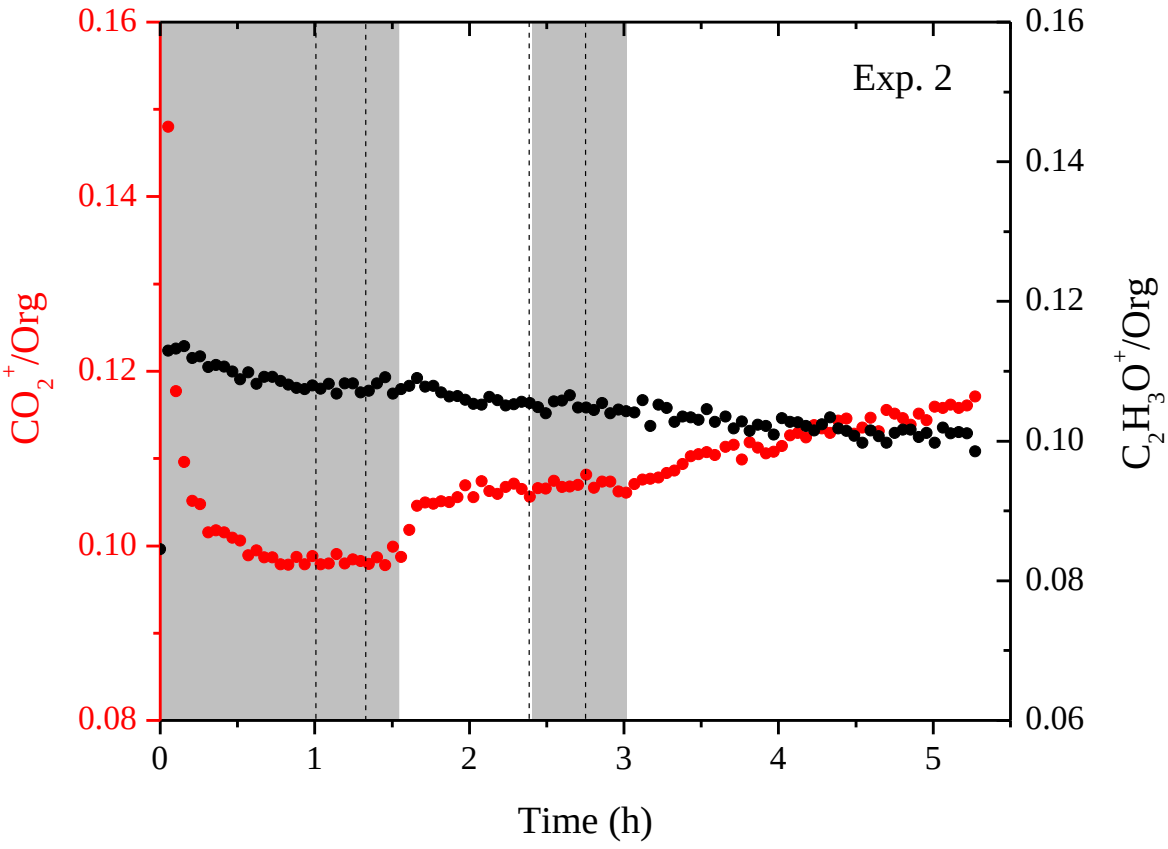

Figure B.4: The **a)** CO_2^+/Org (f_{44}) (red symbols, left axis) and the **b)** $C_2H_3O^+$/Org (f_{43}) (black symbols, right axis) during Exp. 2 based on the high resolution analysis of AMS measurements. The shaded areas indicate that the chamber was dark. The dashed lines mark the beginning and the end of the two HONO injections.

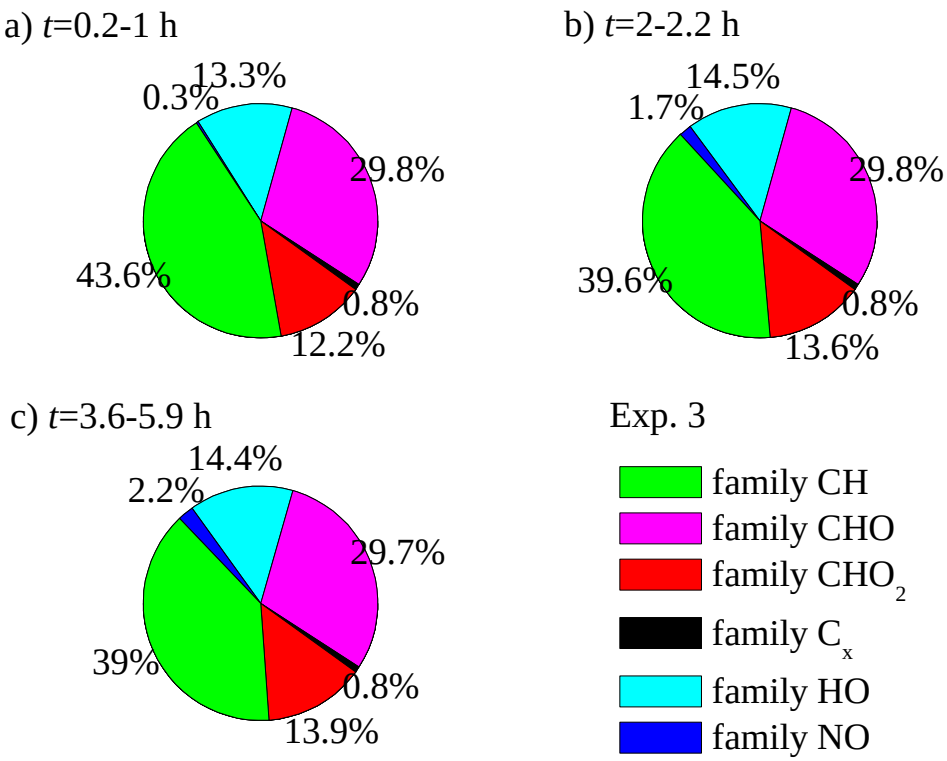

Figure B.5: The SOA composition at the end of the corresponding stages of Exp. 3: **a)** α-pinene ozonolysis; **b)** first OH aging period; **c)** second OH aging period based on the high-resolution family analysis of AMS measurements. The periods of data used are also listed.

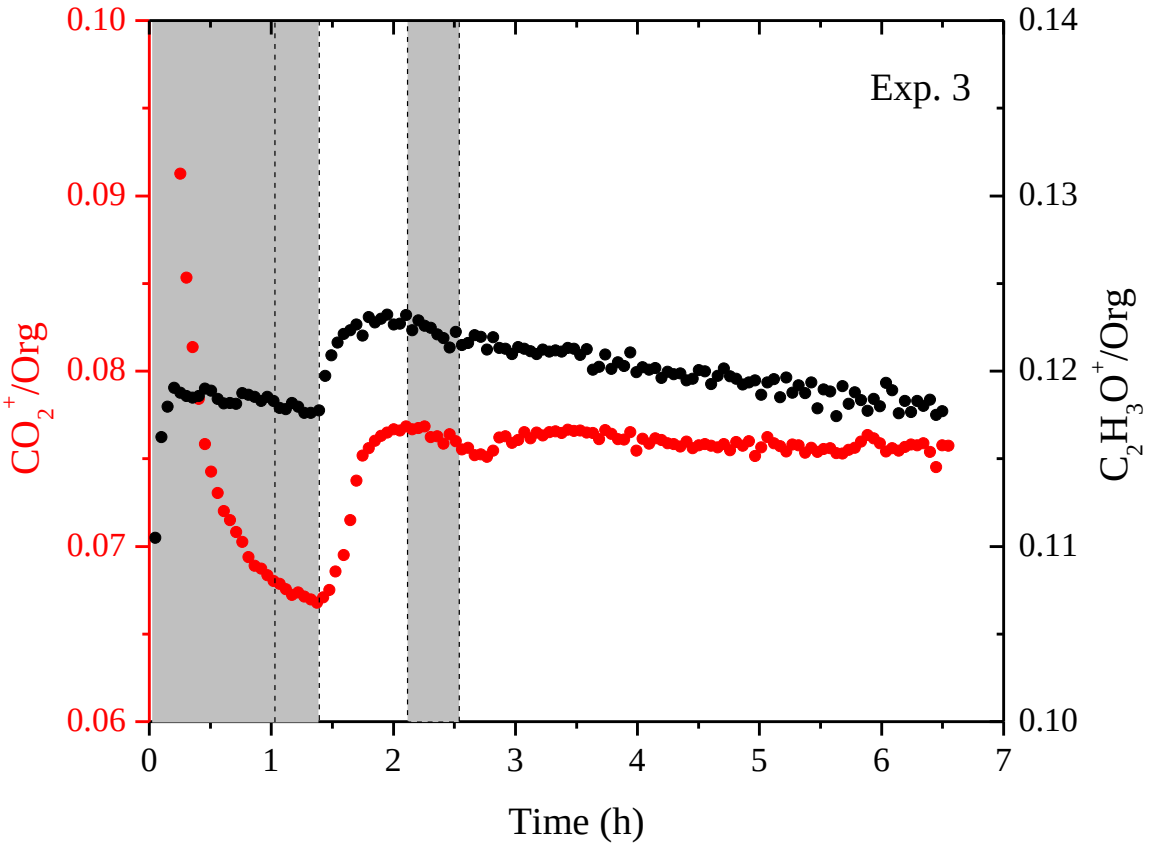

Figure B.6: The **a)** CO_2^+/Org (f_{44}) (red symbols, left axis) and the **b)** $C_2H_3O^+$/Org (f_{43}) (black symbols, right axis) during Exp. 3 based on the high resolution analysis of AMS measurements. The shaded areas indicate that the chamber was dark. The dashed lines mark the beginning and the end of the two HONO injections.

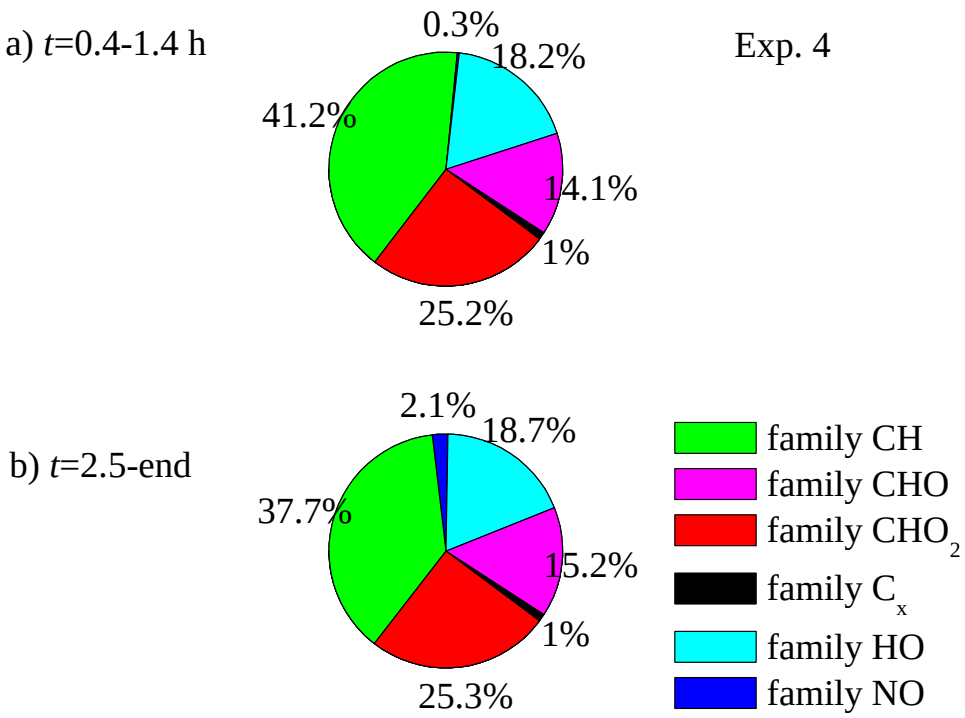

Figure B.7: The SOA composition at the end of the corresponding stages of Exp. 4: **a)** α-pinene ozonolysis; **b)** first OH aging period; **c)** second OH aging period based on the high-resolution family analysis of AMS measurements. The periods of data used are also listed.

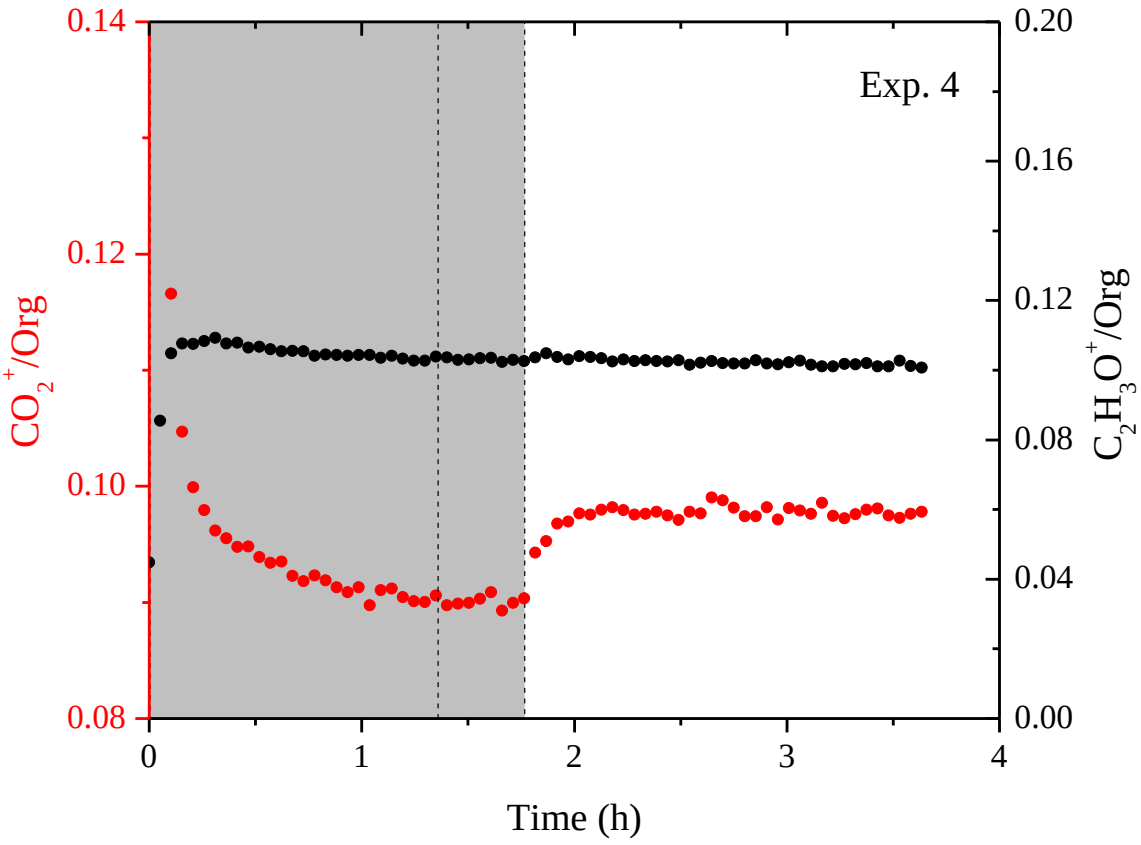

Figure B.8: The **a)** CO_2^+/Org (f_{44}) (red symbols, left axis) and the **b)** $C_2H_3O^+$/Org (f_{43}) (black symbols, right axis) during Exp. 4 based on the high resolution analysis of AMS measurements. The shaded areas indicate that the chamber was dark. The dashed lines mark the beginning and the end of the HONO injection.

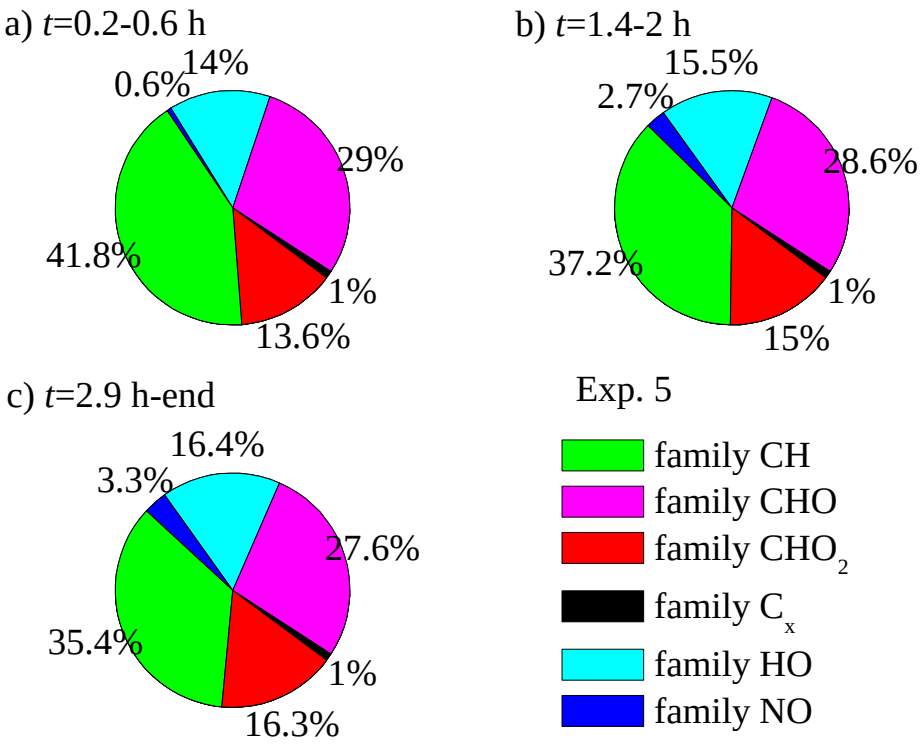

Figure B.9: The SOA composition at the end of the corresponding stages of Exp. 5: **a)** α-pinene ozonolysis; **b)** first OH aging period; **c)** second OH aging period based on the high-resolution family analysis of AMS measurements. The periods of data used are also listed.

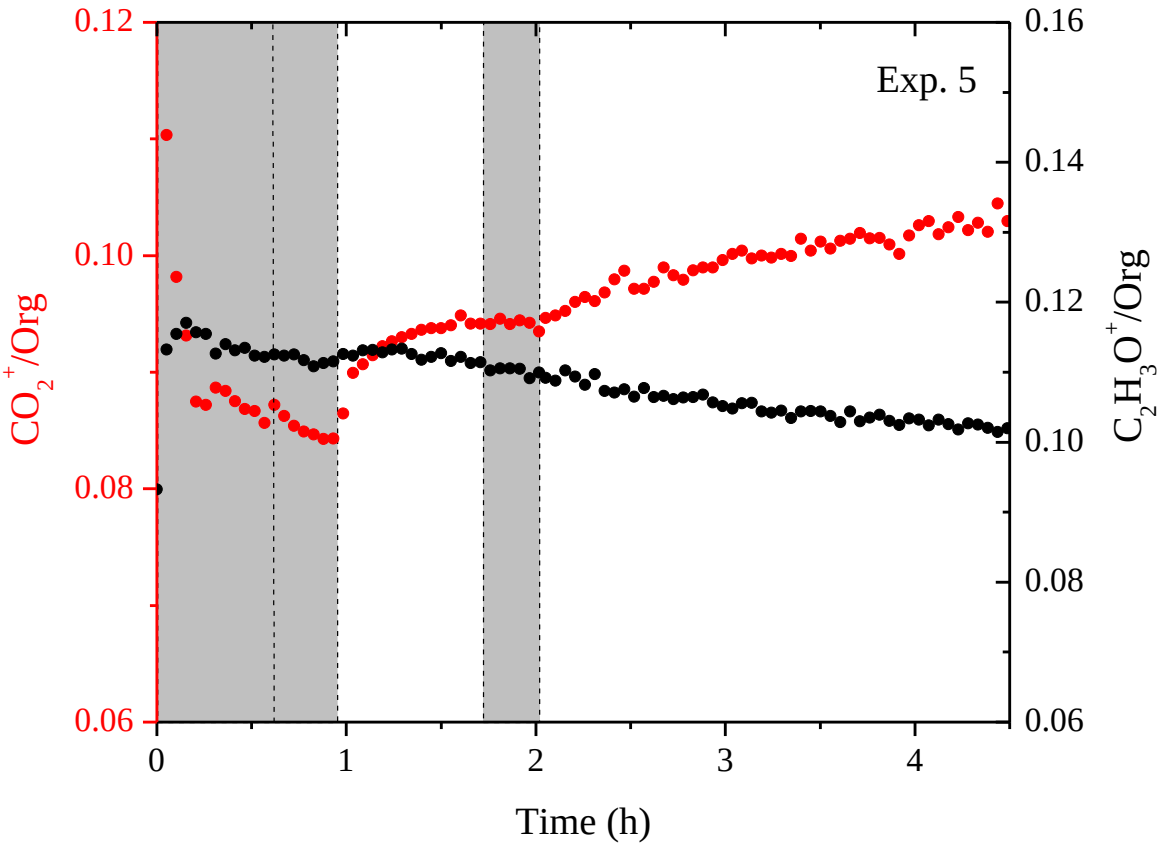

Figure B.10: The **a)** CO_2^+/Org (f_{44}) (red symbols, left axis) and the **b)** $C_2H_3O^+$/Org (f_{43}) (black symbols, right axis) during Exp. 5 based on the high resolution analysis of AMS measurements. The shaded areas indicate that the chamber was dark. The dashed lines mark the beginning and the end of the two HONO injections.

References:

Wang, N., Kostenidou, E., Donahue, N. M., and Pandis, S. N.: Multi-generation chemical aging of α-pinene ozonolysis products by reactions with OH; Atmos. Chem. Phys. Discuss., 10.5194/acp-2017-746, 2017.

Appendix C
Particle wall-loss correction methods in smog chamber experiments

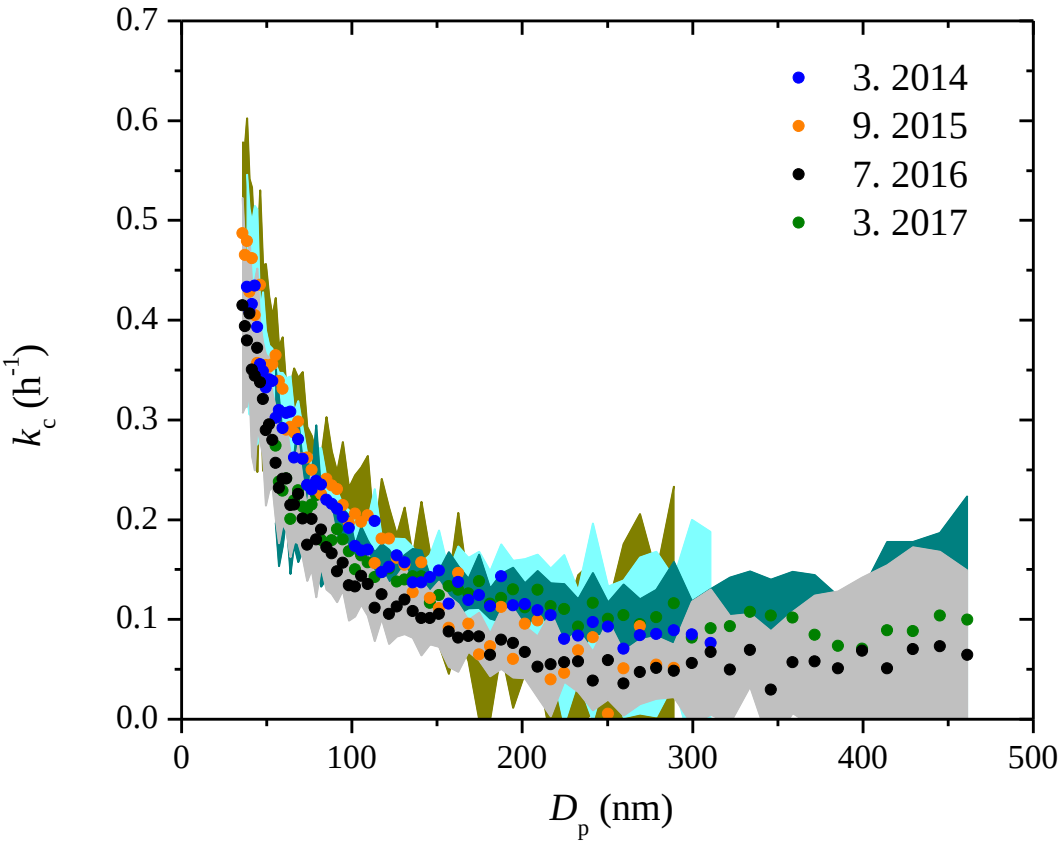

Figure C.1: The $k_c(D_p)$ profiles for the 12 m^3 CMU Teflon chamber over a span of three years. The particle wall-loss rate constants were derived based on SMPS measurements from experiments with only ammonium sulfate particles. The colored area are the uncertainty associated with the corresponding k_c.

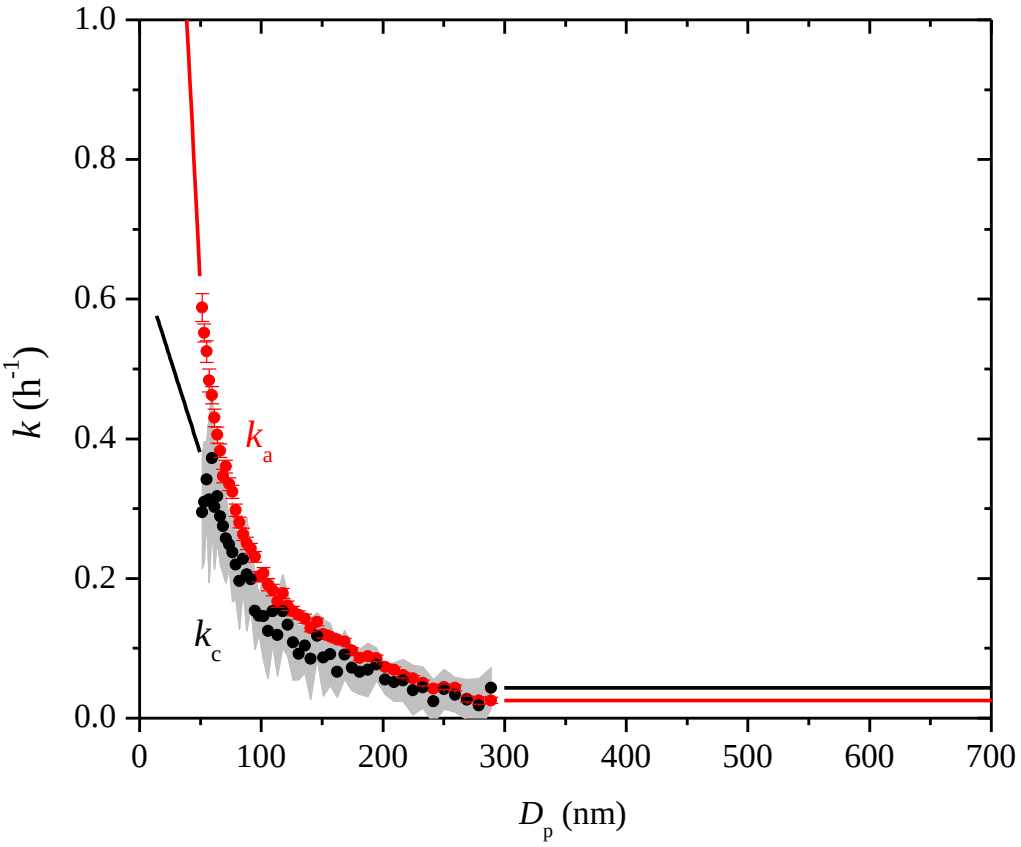

Figure C.2: The apparent (red) and the coagulation-corrected (black) size-dependent particle wall-loss rate constants together with the fits for Exp. 3 across the SMPS-measured particle sizes. The symbols are model results based on the SMPS measurements, and the lines are fits. Only k_a's (red symbols) with an $R^2 > 0.5$ are shown. The error bars are one standard deviation. The grey area is the uncertainty associated with k_c (black symbols).

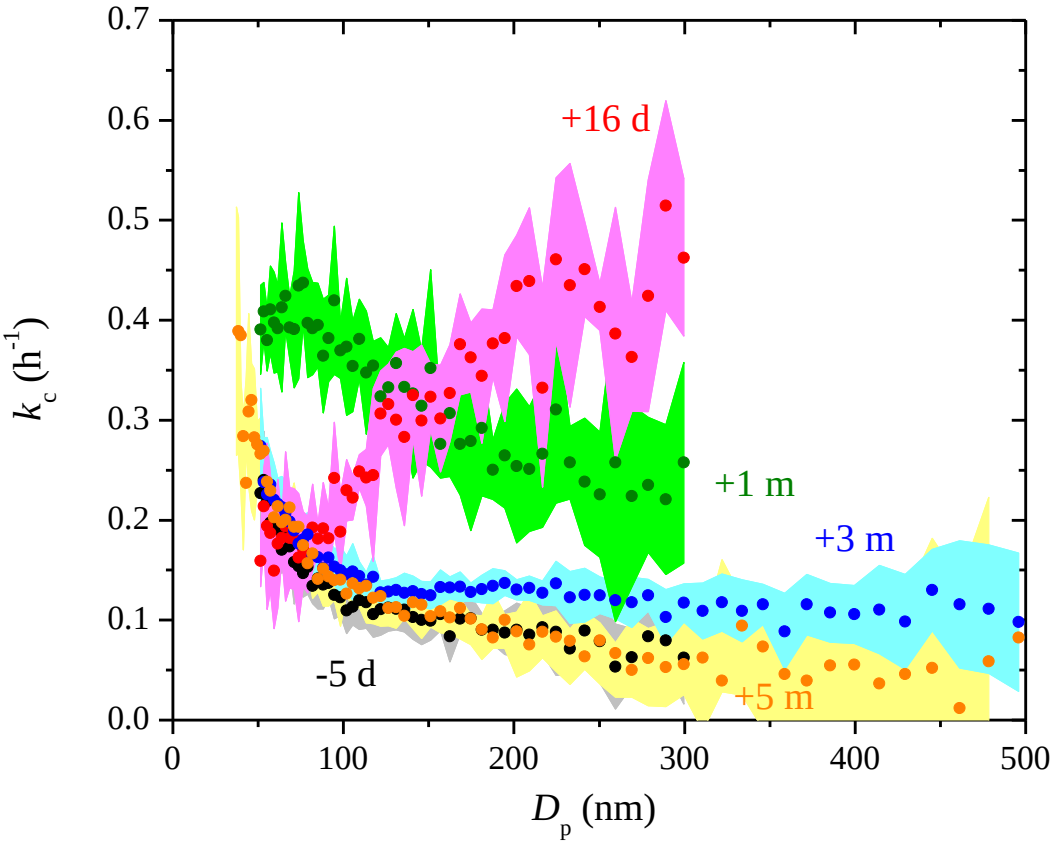

Figure C.3: The coagulation-corrected particle wall-loss rate constant, k_c, at each diameter derived from experiments with only ammonium sulfate particles in the 12 m^3 CMU Teflon chamber before and after some major maintenance in the room where the chamber is suspended. The chamber was partially deflated and its walls subjected to friction repeatedly during the maintenance. The colored area are the uncertainties associated with the corresponding $k_c(D_p)$.

Appendix D
Multi-generation chemical aging of α-pinene ozonolysis products formed under high NO_x conditions

Table D.1: Reactions in the kinetics model and the corresponding reaction rate constants

Reaction	*k* (298 K) (cm^3 $molec^{-1}$ s^{-1} unless otherwise indicated)	Reference
$NO + O_3 \rightarrow NO_2 + O_2$	1.8×10^{-14}	Seinfeld and Pandis (2006)
$NO_2 \xrightarrow{j} NO + O(^3P)$	0.13 min^{-1}	This work
$NO_2 + O_3 \rightarrow NO_3 + O_2$	3.2×10^{-17}	Seinfeld and Pandis (2006)
$NO_2 + NO_3 \rightarrow N_2O_5$	2.2×10^{-30}	Sander et al. (2011)
$NO + NO_3 \rightarrow 2NO_2$	2.6×10^{-11}	DeMore et al. (1994)
$NO_3 \xrightarrow{j} NO_2 + O(^3P)$	0.2 s^{-1}	Seinfeld and Pandis (2006)
$NO_3 \xrightarrow{j} NO + O_2$	0.2 s^{-1}	Seinfeld and Pandis (2006)
$N_2O_5 \rightarrow NO_2 + NO_3$	0.041 s^{-1}	Sander et al. (2011)
$NO_2 + O(^3P) \rightarrow NO + O_2$	1.5×10^{-11}	Seinfeld and Pandis (2006)
α-pinene + $O_3 \rightarrow 0.8OH + RO_2$	8.5×10^{-17}	Atkinson and Arey (2003)
α-pinene + $OH \rightarrow RO_2$	5.4×10^{-11}	Atkinson and Arey (2003)
α-pinene + $NO_3 \rightarrow RO_2$	6.2×10^{-12}	Atkinson and Arey (2003)
$NO + RO_2 \rightarrow NO_2$+RO	9.04×10^{-12}	JPL (2015)
$HO_2 + RO_2 \rightarrow O_2$+ROOH	2.16×10^{-11}	JPL (2015)
$RO_2 + RO_2 \rightarrow RO$	10^{-12}	JPL (2015)
$NO_2 + RO_2 \rightarrow RO_2NO_2$	9.0×10^{-12}	JPL (2015)
$RO_2NO_2 \rightarrow RO_2 + NO_2$	5.78×10^{-5}	Sander et al. (2011)
$NO_3 + RO_2 \rightarrow NO_2$+RO+$O_2$	2.3×10^{-12}	Vaughan et al. (2006)
$O_2 + O(^3P) \rightarrow O_3$	$1.41e^{-14}$	Seinfeld and Pandis (2006)
$HO_2 + O_3 \rightarrow 0.8OH + 2O_2$	$2.05e^{-15}$	JPL (2015)
$HO_2 + NO \rightarrow OH + NO_2$	$8.1e^{-12}$	JPL (2015)
$O_3 + OH \rightarrow HO_2 + O_2$	$6.83e^{-14}$	JPL (2015)
$O_3 \xrightarrow{j} O_2 + O(^3P)$	1×10^{-6} min^{-1}	JPL (2015)
$O_3 \xrightarrow{j} O_2 + O(^1D)$	1×10^{-6} min^{-1}	JPL (2015)
$HO_2 + OH \rightarrow H_2O + O_2$	$1.11e^{-10}$	JPL (2015)
$H_2O + O(^1D) \rightarrow 2OH$	2.2×10^{-10}	(Seinfeld and Pandis, 2006)

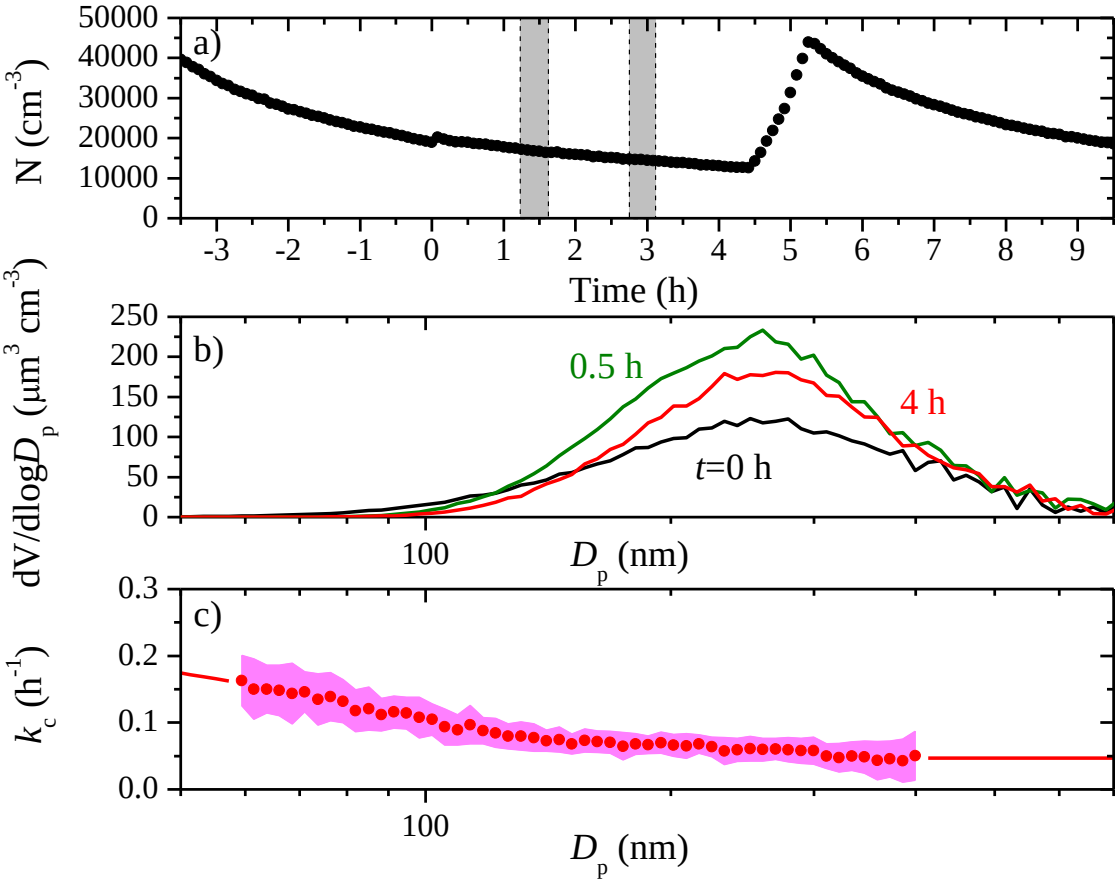

Figure D.1: The SMPS-measured **a)** aerosol number concentration evolution **b)** aerosol volume size distributions at t=0 h, 0.5 h and 4 h during a typical aging experiment with initial NO_x (Exp. 1). Ozone was added into the chamber at time zero to initiate α-pinene ozonolysis under UV illumination. The shaded areas indicate that the chamber was dark. The dashed lines mark the beginning and the end of the two times HONO were added, respectively. The increase in number concentration at t=4.5 h is due to the injection of 5 g L^{-1} ammonium sulfate particles. **c)** The coagulation-corrected, size-dependent particle wall-loss rate constants for Exp. 1, together with the associated uncertainty (magenta area). The red symbols are the rate constants derived from the initial and the final seed periods. The red lines are the fits.

References:

DeMore, W. G., Sander, S. P., Golden, D. M., Hampson, R. F., Kurylo, M. J., Howard, C. J., Ravishankara, A. R., Kolb, C. E., and Molina, M. J.: *Chemical kinetics and photochemical data for use in stratospheric modeling*, evaluation number 11, JPL Publication, 94-26, 1994.

Jet Propulsion Laboratory: *Chemical kinetics and photochemical data for use in atmospheric studies*, evaluation number 18, JPL Publication 15-10, 2015.

Vaughan, S., Canosa-Mas, C. E., Pfrang, C., Shallcross, D. E., Watson, L., and Wayne, R. P.: Kinetic studies of reactions of the nitrate radical (NO_3) with peroxy radicals (RO_2): an indirect source of OH at night?, Phys. Chem. Chem. Phys., 8, 3749-3760, 2006.

Sander, S., Abbatt, J., Barker, J. R., Burkholder, J. B., Friedl, R. R., Golden, D. M., Huie, R. E., Kolb, C. E., Kurylo, M. J., Moortgat, G. K., Orkin, V. L., and Wine, P. H.,: *Chemical kinetics and photochemical data for use in atmospheric studies*, evaluation number 17, JPL Publication, 10, 2011.

Seinfeld, J. H., and Pandis, S. N.: *Atmospheric chemistry and physics: from air pollution to climate change*, Third edition. ed., John Wiley & Sons, Inc., Hoboken, New Jersey, 2016.